Measurement of top quark and W boson polarisation observables with t-channel single-top-quark events in the ATLAS experiment.

Sebastián Pedraza López

Dirigido por:

Susana Cabrera Urbán

Doctorado en Física

Junio, 2017

VNIVERSITAT DE VALÈNCIA

Facultat de Física

Department de Física Atòmica Molecular i Nuclear

Dra. SUSANA CABRERA URBÁN
Científica Titular de Organismos Públicos de Investigación

CERTIFICA:

Que la presente memoria, ***"Measurement of top quark and W boson polarisation observables with t-channel single-top-quark events in the ATLAS experiment"***, ha sido realizada bajo mi dirección en el *Departament de Física Atòmica, Molecular i Nuclear* de la *Universitat de València* por Sebastián Pedraza López y constituye su tesis para optar al grado de doctor en Física.

Y para que así conste, en cumplimiento de la legislación vigente, firmo el presente Certificado.

Firmado
Dra. Susana Cabrera Urbán

Declaration

This dissertation is the result of my own work, except where explicit reference is made to the work of others, and has not been submitted for another qualification to this or any other university.

Sebastián Pedraza López

Yo considero al progreso como la llama de una antorcha que no es para quemar cosa alguna, sino para alumbrarlo todo. La antorcha sólo quema al que se la guarda debajo de su capa y no la pasa, por egoísmo avaro. La antorcha es luz y calor, es amor y generosidad y cada uno debe incrementar su llama con la propia sustancia de su alma y de su cuerpo. Nuestro cuerpo es el cabo de la antorcha y su llama nuestra alma. Al pasarla a otros damos nuestra alma y nuestro cuerpo, nuestro cuerpo, es decir, lo que sirvió para renovarnos, para sucedernos, para revivirnos.

Juan Ramón Jiménez

No se pasa de lo posible a lo real, sino de lo imposible a lo verdadero.

María Zambrano

Este trabajo se lo dedico a todas aquellas personas que me han ayudado a llegar tan lejos. A mi familia y amigos. A ti Ali y a ti Darío, gracias por creer en mi, por vuestro amor y por el apoyo incondicional que siempre me habéis ofrecido, os quiero mucho. Y a ti Marta. Gracias por tu amor, tu comprensión, tu paciencia y el sacrificio que también has tenido que hacer estos años para que yo pueda realizar mi sueño.
Y a ti Papá, lo conseguí.

Preface

This dissertation presents the work done for the alignment of the ATLAS Inner Detector during the last campaign of data taking in Run I, and an analysis to probe the Wtb vertex structure in t-channel single top quark production and decay, using 20.3 fb^{-1} of proton-proton collisions data recorded by the ATLAS detector with a centre of mass energy of $\sqrt{s} = 8$ TeV.

Since its development in the 1960's and 1970's, the Standard Model of elementary particle physics has been experimentally tested up to the TeV scale and has successfully explained a host of experimental results. It has predicted a wide variety of phenomena which subsequently have been discovered, such as the existence of the $W^{\pm}$ and Z bosons, the top quark and the recently discovered Higgs boson. Despite its great success, the Standard Model is not considered to be the final fundamental theory of particle physics. There are open questions on which the Standard Model can not provide satisfactory answers, such as the existence of dark matter and dark energy, neutrino masses or the matter-antimatter asymmetry of the universe. A brief description of the Standard Model and the theoretical framework needed to develop the analysis presented in this dissertation is shown in Chapter 1.

The Large Hadron Collider (LHC), built by the European Organization for Nuclear Research (CERN), has been designed to study the Standard Model and beyond providing proton-proton collisions with an unprecedented centre of mass energy and luminosity to its particle detectors. The ATLAS experiment, whose data are used in this thesis, is one of the four largest detectors at the LHC. The description of the LHC and the ATLAS experiment can be found in Chapter 2. A well calibrated and aligned tracker is needed in order to

provide good quality tracks which are used widely in different reconstruction algorithms in ATLAS. The basics of the Inner Detector alignment as well as the work developed to provide the best alignment corrections are described in Chapter 3.

Events with t-channel single top events with one charged lepton, two jets, one of them being a b-jet and missing transverse momentum are used to probe the structure of the Wtb vertex through the measurement of observables related to the polarisation of the top quark and W boson. The dataset and the Monte Carlo samples used as well as the method followed to estimate the backgrounds are described in Chapter 4. The methodology followed in order to perform the measurements and the estimation of the uncertainties are explained in Chapter 5. Finally, the conclusion for this dissertation is contained in Chapter 6.

Contents

CHAPTER 1

Theoretical framework

The top quark is the heaviest known elementary particle and one of the least well measured. Its mass is very close to the electroweak symmetry breaking scale, and therefore the study of its properties can provide information about new physics phenomena beyond the Standard Model. In particular, we are interested in its couplings in the Wtb vertex which can yield information about the existence of CP violation and the matter-antimatter asymmetry of the Universe. To that end, we will measure in Chapter 5 a set of observables related to the top quark and W boson polarisation by using single top quark events produced in the t-channel. In order to develop these ideas in greater detail it will be necessary to describe first our current knowledge of elementary particles and their interactions.

1.1 The Standard Model of particle physics

The Standard Model (SM) of elementary particle physics is a quantum gauge field theory which provides a fundamental description of all elementary particles, their dynamics and interactions. According to the SM, all matter is composed of fermions and the interactions are mediated by the exchange of bosons.

Fermions are particles with half integer spin that obey the Fermi-Dirac statistics and the Pauli exclusion principle[1]. In the SM, the fermions are clas-

[1]The Pauli exclusion principle implies that two identical fermions cannot share the same

	Matter particles			Spin	Electric charge
Family	1^{st}	2^{nd}	3^{rd}		
Quarks	u	c	t	1/2	+2/3
	d	s	b	1/2	−1/3
Leptons	ν_e	ν_μ	ν_τ	1/2	0
	e^-	μ^-	τ^-	1/2	−1

Table 1.1: The fermions of the Standard Model listed with their spin and electric charge.

	Field particles	Force	Spin	Electric charge
Gauge bosons	g	strong	1	0
	$W^\pm$ and Z	weak	1	±1 and 0
	γ	electromagnetic	1	0
Scalar bosons	H		0	0

Table 1.2: The bosons of the Standard Model listed with their spin and electric charge.

sified in quarks and leptons (see Table 1.1), which are point-like fundamental particles with spin $s = 1/2$. Each fermion has a corresponding anti-particle which has the same mass but carrying opposite quantum numbers. Quarks and leptons are arranged in three generations, the second and third generations being a copy of the first one but having larger masses. Each generation is composed of an up-type quark (up (u), charm (c), top (t)); a down-type quark (down (d), strange (s), bottom (b)); a charged lepton (electron (e), muon (μ), tau (τ)) and its neutral partner called neutrino (ν_e, ν_μ, ν_τ). Charged leptons carry an electric charge of $-q_e$, where q_e is the absolute value of the electron charge. They are sensitive to electromagnetic and weak interactions, whereas neutrinos only interact via weak force. Quarks carry a fractional electric charge, $+\frac{2}{3}q_e$ for the up-type quarks and $-\frac{1}{3}q_e$ for down-type quarks. In addition quarks carry colour charge, thereby they are sensitive to the electromagnetic, weak and also to the strong interactions. Quarks are not found in nature as free particles since they are confined through strong interaction into colorless composite particles called hadrons.

Bosons are particles with integer spin that obey the Bose-Einstein statistics. The SM bosons, listed in Table 1.2, are the mediators of three of the four fundamental forces in nature known up to now: electromagnetic, weak and strong. They are particles with spin $s = 1$, and each fundamental force has its associated boson:

- The electromagnetic force acts between particles with electrical charge. Its associated boson is the photon, γ, which is a massless particle without

quantum state.

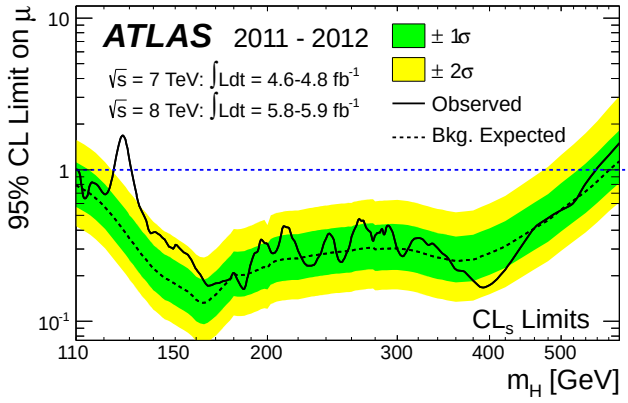

Figure 1.1: ATLAS combined search results: the observed (solid) 95% CL upper limit on the signal strength as a function of m(H) and the expectation (dashed) under the background-only hypothesis. The dark and light shaded bands show the $\pm\sigma$ and $\pm 2\sigma$ uncertainties on the background-only expectation [1].

electrical charge.

- The strong interaction binds quarks into hadrons and it holds protons and neutrons together in the atom nuclei. The associated boson of this force is the gluon, g, which is massless, electrically neutral and carry colour charge. Unlike photons, gluons not only interact with quarks, but also they interact among themselves.

- The weak interaction is responsible for nuclear decays such as the β decay. In contrast to the massless photon and gluon, the mediators of this force are massive gauge bosons, the electrically charged $W^{\pm}$ bosons and the neutral Z boson.

- Gravity is the weakest of all the fundamental forces on subnuclear scales. Therefore, it can be neglected and is not included in the SM.

The SM is a quantum gauge field theory built from the principle that physics should be invariant under local gauge transformations. It is described by a lagrangian whose symmetry group is $SU(3)_C \otimes SU(2)_L \otimes U(1)_Y$. The strong interaction, also known as Quantum Chromodynamics (QCD), is associated with the local $SU(3)_C$ symmetry. On the other hand, the local $SU(2)_L \otimes U(1)_Y$ symmetry corresponds to the electroweak interaction, which was proposed by Glashow, Salam and Weinberg [2–4] in the 1960s and unifies the electromagnetic and weak interactions.

In principle, the particles that compose the SM are massless, unlike what is observed in nature. Therefore, a mechanism must be introduced in the theory

in order to generate mass. The $W^{\pm}$ and Z^0 bosons acquire mass through the electroweak symmetry breaking mechanism (EWSB). In the SM, the Higgs scalar field produces a spontaneous breaking of the electroweak symmetry when it acquires a non-vanishing vacuum expectation value. This mechanism is known as the Brout-Englert-Higgs mechanism [5–7] and postulates the existence of one scalar particle, the Higgs boson. The Higgs field also provides mass to the SM fermions via Yukawa interactions. On July 2012, the ATLAS and the CMS collaborations announced they had each observed a new particle consistent with the Higgs boson at the LHC [8,9], with a mass of 125 GeV (Figure 1.1). This is one of the biggest achievement of the LHC physics program up to now. After this experimental fact, Francois Englert and Peter Higgs were awarded with the Nobel prize in physics *"for the theoretical discovery of a mechanism that contributes to our understanding of the origin of mass of subatomic particles, and which recently was confirmed through the discovery of the predicted fundamental particle, by the ATLAS and CMS experiments at CERN's Large Hadron Collider"* [10].

The SM theory was exhaustively tested with high precision up to an energy scale of $\sqrt{s} \sim 200$ GeV using the LEP collider. Then, using the Tevatron collider, the SM was carefully tested up to an energy scale of $\sqrt{s} = 1.8 - 1.9$ TeV, which led to the discovery of the top quark predicted by the SM, and currently, the SM is being tested to an energy of $\sqrt{s} = 13$ TeV with the LHC. The measurements and searches performed up to now seem to be consistent with the theory, and no hints of new physics are observed. Figure 1.2 shows a summary of several SM cross section measurements and their comparison with their theoretical predictions, which are calculated at Next-to-Leading-Order (NLO) or higher.

Despite the great success of the SM, the discovery of the Higgs boson being its latest achievement, there are some open questions that the SM cannot answer, such as the oscillation of neutrinos [12], the origin of dark matter and dark energy [13], the matter-antimatter asymmetry [14], etc. These are reasons to search for new physics beyond the SM, predicted by theories such as supersymmetry [15] or extradimensions [16]. The research performed in this thesis is motivated by the matter-antimatter asymmetry observed in nature, looking for violation of CP symmetry by measuring W boson and top quark polarisation observables using single-top quark events.

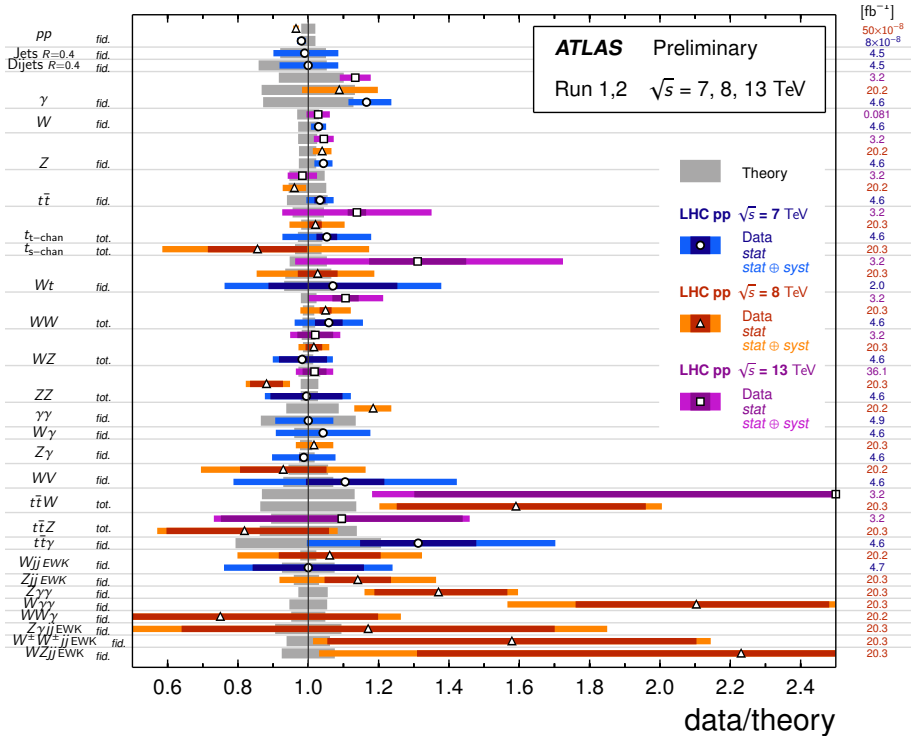

Figure 1.2: Summary of several SM total and fiducial production cross section measurements, corrected for leptonic branching fractions, compared to the corresponding theoretical expectations. All theoretical expectations were calculated at NLO or higher. The W and Z vector-boson inclusive cross sections were measured with 35 pb-1 of integrated luminosity from the 2010 dataset. All other measurements were performed using the 2011, 2012, or 2015 datasets. The dark-color error bar represents the statistical uncertainly. The lighter-color error bar represents the full uncertainty, including systematics and luminosity uncertainties [11].

$\sqrt{s}$(TeV)	$\sigma_{t\bar{t}}$ (pb)	σ_{t-chan} (pb)	$\sigma_{Wt-chan}$ (pb)	σ_{s-chan} (pb)
7	$177.3\ ^{+10.1}_{-10.8}$ [20]	$64.57^{+2.63}_{-1.74}$ [21]	$15.74^{+1.17}_{-1.21}$ [22]	$4.63^{+0.20}_{-0.18}$ [23]
8	$252.9\ ^{+13.3}_{-14.5}$ [20]	$87.76^{+3.44}_{-1.91}$ [21]	22.37 ± 1.52 [22]	5.61 ± 0.22 [23]
13	$831.8\ ^{+40.3}_{-45.6}$ [20]	$216.99^{+9.04}_{-7.71}$ [24, 25]	71.7 ± 3.8 [22]	$10.32^{+0.40}_{-0.36}$ [24, 25]

Table 1.3: Theoretical prediction of the cross sections for the different production processes of top quarks at LHC at different energies. The values of the cross section for the different single top processes correspond to the combined production of top and anti-top quarks.

Experiment ($\mathcal{L}$ (fb^{-1}))	$\sqrt{s}$(TeV)	$\sigma_{t\bar{t}} \pm$ (stat) $\pm$ (sys) $\pm$ (lumi) (pb)	$\delta\sigma_{t\bar{t}}$(%)	Ref.
ATLAS dilepton eμ (5)	7	$182.9 \pm 3.1 \pm 4.2 \pm 3.6$	3.5	[26]
ATLAS dilepton eμ (20)	8	$242.4 \pm 1.7 \pm 5.5 \pm 7.5$	3.9	[26]
ATLAS dilepton eμ (3.2)	13	$818 \pm 8 \pm 27 \pm 19$	4.2	[27]
CMS dilepton eμ (5)	7	$174.5 \pm 2.1\ ^{+4.5}_{-4.0} \pm 3.8$	3.6	[28]
CMS dilepton eμ (20)	8	$245.6 \pm 1.3\ ^{+6.6}_{-5.5} \pm 6.5$	3.8	[28]
CMS lepton + jets (2.3)	13	$834.6 \pm 2.5 \pm 22.8 \pm 22.5$	3.9	[29]

Table 1.4: Top pair production cross section most precise measurements at LHC.

1.2 Top quark physics at LHC

The top quark is the heaviest of the quarks predicted by the Standard Model. Its existence was theoretically proposed in 1973 by Makoto Kobayashi and Toshihide Maskawa to explain the observed CP violation in kaon decay [17] and it was experimentally discovered in 1995 by the CDF and DØ collaborations at Tevatron [18, 19]. Due to its large mass close to the electroweak scale and therefore, its strong coupling to the Higgs boson in the SM, the properties of the top quark have been studied extensively at the LHC. In this section the latests results of top quark properties measured by ATLAS will be summarized.

There are two main mechanisms for producing top quarks at hadron colliders, top quark pair production and single top production. Top quark pairs production has the highest cross section of the two mechanisms, as it is shown in Table 1.3, and it is performed via the strong interaction. In Figure 1.3 it is shown the different processes that contribute to top quark pairs production at leading order. As the LHC is a proton-proton collider, the production of top quarks pairs through quark-antiquark annihilation is disfavoured with respect to the gluon fusion, the latter being responsible of roughly 80% of the top quark pairs produced. In Table 1.4 are shown the most precise measurements of the top quark pair production at LHC at different centre of mass energy.

The second mechanism, single top quark production, consists on the production of top quarks via the electroweak interaction. There are three process

Experiment ($\mathcal{L}$ (fb^{-1}))	$\sqrt{s}$(TeV)	σ_{t-chan} (pb)	$\delta\sigma_{t-chan}$(%)	Ref.
ATLAS (4.59)	7	68.0 ± 4.5	6.6	[30]
ATLAS (20.2)	8	89.6 ± 8.0	8.9	[31]
ATLAS (3.2)	13	247.0 ± 46.0	19.0	[32]
CMS (1.17 μ ch. 1.57 e ch.)	7	67.2 ± 6.1	9.0	[33]
CMS (19.7)	8	83.6 ± 7.7	9.3	[34]
CMS (2.3)	13	232.0 ± 31.0	13.0	[35]

Table 1.5: Single top quark t-channel production cross section most precise measurements at LHC.

responsible for the production of single top quarks, whose leading order Feynman diagrams are shown in Figure 1.4(a):

- **t-channel** is the electroweak scattering of a light quark and a b quark where a virtual space-like W boson is exchanged between the two quarks. This is the dominant production mode of single top quarks because it has the largest cross-section among the three production modes. A summary of the latest measurements performed by ATLAS and CMS on the production of single top quarks via t-channel is shown in Table 1.5.

- **s-channel** is the production of a top and a bottom quark by quark-antiquark annihilation. A virtual time-like W boson is formed from the two initial state quarks. Due to the nature of the proton, this production mode is strongly suppressed at the LHC compared to the Tevatron because at the LHC the antiquarks come from the proton sea quarks whereas at the Tevatron the antiquarks are valence quarks. The first evidence of s-channel single top production at LHC was observed by ATLAS in 2015 using the 20.3 fb^{-1} of the 8 TeV sample recorded in 2012 [36]. In Figure 1.4(b) it is shown the Feynman diagram describing the process at leading order.

- **Wt-channel** is the production mode where a top quark is produced together with an on-shell W boson. Because of the massive particles in the final state, this production mechanism had an extremely low rate at the Tevatron and could not be observed by neither CDF nor D$\emptyset$ collaborations. First evidence of this production mechanism was reported by ATLAS and CMS at the LHC [37, 38]. The leading order Feynman diagram describing this mode is shown in Figure 1.4(c).

The mass of the top quark has to be determined from experimental measurements because it is a free parameter of the SM. The most precise measurement of the reconstructed top mass performed by ATLAS yields a mass of

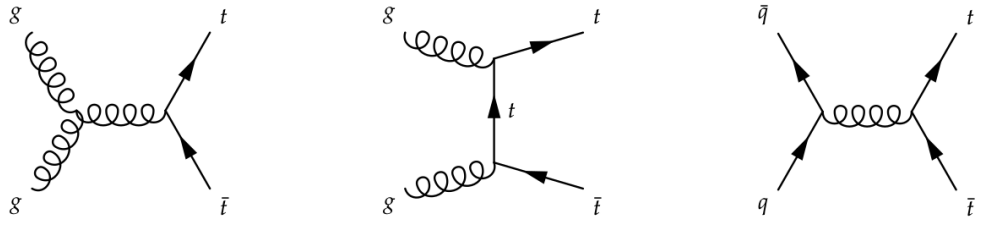

Figure 1.3: Feynman diagrams of $t\bar{t}$ production at leading order. On the left, the first two diagrams represent the production through gluon fusion. On the right, the production is due to quark-antiquark annihilation.

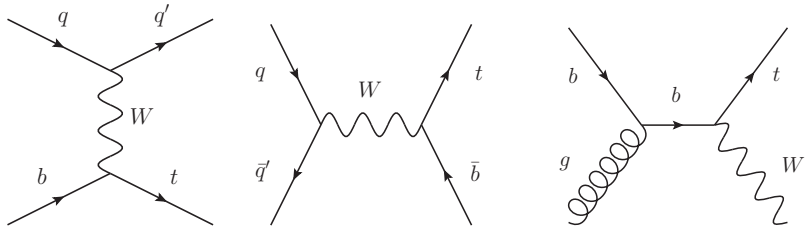

(a) t-channel **(b)** s-channel **(c)** Wt-channel

Figure 1.4: Feynman diagramas of the single-top production at leading order.

172.84 ± 0.70 GeV [39], which is 40 times larger than the b quark mass, being the heaviest fundamental particle experimentally observed.

An interesting electroweak process where tests on the SM predictions can give some hint of new physics is the top decay through flavour changing neutral current (FCNC). These processes, suppressed by GIM mechanism in the SM [40], have branching ratios of the order of 10^{-15} while some beyond standard models (BSM) can predict higher production ratios [41–43] . The latest results on this searches performed by ATLAS and CMS show that there is no excess in the observed number of events relative to the SM prediction [44–47].

1.3 Anomalous couplings in Wtb vertex

The large mass of the top quark leads to a lifetime of $\tau_t \sim 10^{-25}$ s, which is shorter than the typical timescale of the strong interaction, which is of the order of $\sim 10^{-23}$ s. This makes the top quark unique among the other quarks because it decays before hadronization takes place, thus, we can study a quasi-free quark. Top quark decays weakly through the Wtb vertex with almost 100% of branching fraction into a W boson and a b quark, while the production of the top quark can be performed via strong interaction in $t\bar{t}$ pairs, or via the weak interaction in single tops. The advantage of study top quarks using single top events with respect to using $t\bar{t}$ pairs is that the same physical process is

involved in both the production and the decay of the top quark, thus we can study the weak interaction and in particular the Wtb vertex by minimizing the contamination from QCD processes. In addition, as the top quark does not hadronize before decay, it transfers all the spin information to the decay products. In the case of $t\bar{t}$ events, the spin information of the $t\bar{t}$ system is also transferred to the decay products, therefore the spin of the top and anti-top quark can not be disentangled [48]. However, the spin information of the top (anti-top) quark can be accessed when it is produced singly. Furthermore, top quarks produced in the t-channel are polarized along the direction of the light quark [49], which is a measurable axis that could be used to study the Wtb vertex.

The extended lagrangian that describes the Wtb vertex in a model independent way can be written as [50] :

$$\mathcal{L}_{Wtb} = -\frac{g}{\sqrt{2}}\bar{b}\gamma^{\mu}(V_L P_L + V_R P_R)tW_{\mu}^{-} - \frac{g}{\sqrt{2}}\bar{b}\frac{i\sigma^{\mu\nu}}{M_W}(g_L P_L + g_R P_R)tW_{\mu}^{-} + \text{h.c.}\ . \tag{1.1}$$

This lagrangian arises from effective operators of dimension six, where the coupling strengths V_L and V_R are the left and right-handed vector couplings respectively, and g_L and g_R are the left and right-handed tensor couplings respectively. These are the so-called anomalous couplings, since in the SM $V_L = V_{tb}$ while $V_R = g_R = g_L = 0$. In order to measure the different couplings, a set of observables sensitive to them are defined with special focus on g_R, due to the fact that a non zero imaginary part of g_R may imply CP violation. These observables will be described in the following sections but the complete understanding on the anomalous couplings can be found in References [51,52].

1.3.1 W boson helicity fractions

The W boson produced in the decay of the top quark is polarised in three different states: left, zero or right helicity. The probability of finding the W boson in such states can be related to the total decay width of the top quark as :

$$\Gamma(t \to Wb) = \Gamma_L + \Gamma_0 + \Gamma_R, \tag{1.2}$$

$$1 = \frac{\Gamma_L}{\Gamma} + \frac{\Gamma_0}{\Gamma} + \frac{\Gamma_R}{\Gamma} = F_L + F_0 + F_R\ , \tag{1.3}$$

where $F_i = \Gamma_i/\Gamma$ are the so-called helicity fractions.

The angular distribution of the lepton produced by the decay of the W

boson can be written as:

$$\frac{1}{\Gamma}\frac{d\Gamma}{d\cos\theta^*} = \frac{3}{8}(1-\cos\theta^*)^2 F_L + \frac{3}{4}\sin^2\theta^* F_0 + \frac{3}{8}(1+\cos\theta^*)^2 F_R, \tag{1.4}$$

where θ^* is the angle between the momentum of the charged lepton in the W rest frame and the W momentum in the top quark rest frame, as it is shown in Figure 1.5.

From the angular distribution $\cos\theta^*$ we can define different asymmetries which provide the same information as the helicity fractions, but they are easier to measure from the experimental point of view as we will see in the following chapter. We can define an asymmetry as:

$$A_z = \frac{N(\cos\theta^* > z) - N(\cos\theta^* < z)}{N(\cos\theta^* > z) + N(\cos\theta^* < z)}, \tag{1.5}$$

where $N(\cos\theta^* > z)$ ($N(\cos\theta^* < z)$) is the number of events where $\cos\theta^*$ is below (above) z^2. With this definition, we can build three different asymmetries which can be related to the helicity fractions:

$$z = 0 \rightarrow A_{FB} = \frac{3}{4}(F_R - F_L), \tag{1.6}$$

$$z = -(2^{2/3}-1) \rightarrow A_+ = 3\beta[F_0 + (1+\beta)F_R] \ , \tag{1.7}$$

$$z = (2^{2/3}-1) \rightarrow A_- = -3\beta[F_0 + (1+\beta)F_L] \ , \tag{1.8}$$

where $\beta = 2^{1/3} - 1$. In the particular case where $z = 0$, the asymmetry is called *forward-backward* asymmetry. As said before, asymmetries are easier to measure experimentally, however, in order to compare with other published results it is useful to provide the measured values of the helicity fractions. Therefore, we can write the helicity fractions as a function of the asymmetries as follows:

$$F_L = \frac{1}{1-\beta} - \frac{A_+ - \beta A_-}{3\beta(1-\beta^2)} \ , \tag{1.9}$$

$$F_0 = \frac{1+\beta}{1-\beta} + \frac{A_+ - A_-}{3\beta(1-\beta)} \ , \tag{1.10}$$

$$F_R = \frac{1}{1-\beta} + \frac{A_- - \beta A_+}{3\beta(1-\beta^2)} \ . \tag{1.11}$$

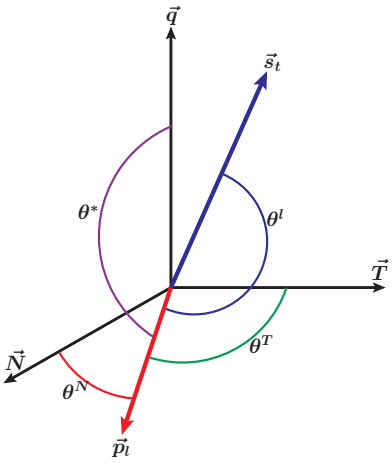

Figure 1.5: The polarisation frame is a right-handed cartesian frame defined by the momentum of the W boson in the top rest frame ($\vec{q}$) and the normal and transverse axis, where $\vec{N} = \vec{s}_t \times \vec{q}$ and $\vec{T} = \vec{q} \times \vec{N}$. The angular distributions we can measure are: θ^*, which is the angle between the momentum of the charged lepton ($\vec{p}_l$) in the W boson rest frame and the momentum of the W boson in the top rest frame; θ^N which is the angle between the momentum of the charged lepton in the W boson rest frame and the normal direction and θ^T, which is the angle between the momentum of the charged lepton in the W boson rest frame and the transverse direction. The angle θ^l related with the polarisation of the top quark is measured between the momentum of the charged lepton and the momentum of the light quark ($\vec{s}_t$) both in the top quark rest frame [51].

1.3.2 W boson polarisation fractions

These observables exploit the feature of polarized top quarks in t-channel single top events by measuring angular distributions in the so-called polarisation frame [51]. The spin of the top quark is partially polarized along the momentum direction of the light quark, which is one of the axis of this new frame. The other two axis are defined as $\vec{N} = \vec{s}_t \times \vec{q}$ and $\vec{T} = \vec{q} \times \vec{N}$, where $\vec{s}_t$ is the light quark momentum, $\vec{q}$ is the momentum of the W boson in the top rest frame, $\vec{N}$ is the normal axis and $\vec{T}$ is the transverse axis, as it can be seen Figure 1.5.

The W boson has three possible polarisation states : positive, zero or negative polarisation. These polarisation states are defined for the normal and the transverse axis and the angular distribution can be written as:

$$\frac{1}{\Gamma}\frac{d\Gamma}{d\cos\theta^N} = \frac{3}{8}(1+\cos\theta^N)^2 F_+^N + \frac{3}{4}\sin^2\theta^N F_0^N + \frac{3}{8}(1-\cos\theta^N)^2 F_-^N \ , \quad (1.12)$$

$$\frac{1}{\Gamma}\frac{d\Gamma}{d\cos\theta^T} = \frac{3}{8}(1+\cos\theta^T)^2 F_+^T + \frac{3}{4}\sin^2\theta^T F_0^T + \frac{3}{8}(1-\cos\theta^T)^2 F_-^T \ , \quad (1.13)$$

where Γ is the decay width of the top quark; $\theta^{N(T)}$ is the angle between the mo-

[2]The threshold z is a fixed value in the interval $[-1, 1]$. In the case of $z = 0$ we get a forward-backward asymmetry.

mentum of the lepton in the W boson rest frame and the normal (transverse) axis, and $F_i^{N(T)}$ are the so-called normal (transverse) polarisation fractions, which satisfy $F_+^{N(T)} + F_0^{N(T)} + F_-^{N(T)} = 1$.

For these angular distributions we can define the same set of asymmetries as in the previous case:

$$z = 0 \rightarrow A_{FB}^{N,T} = \frac{3}{4}(F_+^{N,T} - F_-^{N,T}) \ , \tag{1.14}$$

$$z = -(2^{2/3} - 1) \rightarrow A_+^{N,T} = 3\beta[F_0^{N,T} + (1+\beta)F_+^{N,T}] \ , \tag{1.15}$$

$$z = (2^{2/3} - 1) \rightarrow A_-^{N,T} = -3\beta[F_0^{N,T} + (1+\beta)F_-^{N,T}] \ . \tag{1.16}$$

Among these six observables sensitive to anomalous couplings in the Wtb vertex, the most important one is the forward-backward asymmetry in the normal direction, A_{FB}^N. This observable is very sensitive to the imaginary part of the right-handed tensor coupling g_R. For small values of g_R and under the assumptions of $V_R = g_L = 0$ and $V_L = V_{tb}$, we obtain:

$$A_{FB}^N = 0.64\mathcal{P}\mathrm{Im}(g_R) \ , \tag{1.17}$$

where $\mathcal{P}$ is the degree of polarisation of the top quark (see Section 1.3.3). Thus, a non zero A_{FB}^N may imply CP violation[3].

1.3.3 Top quark polarisation

The degree of polarisation of the top quark can be measured via the angular distribution of the top quark decay products:

$$\frac{1}{\Gamma}\frac{d\Gamma}{d\cos\theta^i} = \frac{1}{2}(1 + \alpha_i\mathcal{P}\cos\theta^i) \ , \tag{1.18}$$

where Γ is the decay width of the top quark; θ^i is the angle between the momentum of the ith decay product in the top quark rest frame and the top spin direction which is parallel to the light quark momentum (see Figure 1.5); α_i is the so-called spin analysing power of the ith decay product and $\mathcal{P}$ is the degree of polarisation of the top quark [51]. The charged lepton is the decay product of the top quark with the largest spin analysing power at leading order, as can be seen in Table 1.6, therefore, it will be used in order to perform the measurement of the top quark polarisation in Chapter 5.

[3] Although the A_{FB}^N asymmetry is sensitive to CP violating phasis in the Wtb vertex, it is not genuinely CP violating and could be faked by unitarity phases. The sum of asymmetries for top and antitop quark decays, $A_{FB}^{CP} = A_{FB}^N(t) + A_{FB}^N(\bar{t})$ is unambiguously CP violating.

Particle type	α_i
Charged lepton	1.000
b quark	-0.403
W boson	0.403
neutrino	-0.324

Table 1.6: Predicted tree level values of the spin analysing power for the top quark decay products. For top antiquarks the quantities have the same values with opposite sign.

As it was done for the helicity and polarisation fractions, we can build an asymmetry related to the angular distribution $\cos\theta^i$, but in this case it only has sense the forward-backward asymmetry:

$$A_{FB} = \frac{1}{2}\alpha_i \mathcal{P} \ . \tag{1.19}$$

Scope of the analysis

The large number of single top quark events produced by the LHC at $\sqrt{s} =$ 8 TeV in 2012 allows the study of the structure of the Wtb vertex through the measurement of all the observables sensitive to anomalous couplings defined in this chapter. The asymmetries presented here are measured using t-channel single top events. In the case of the W boson helicity, the measured helicity fractions are provided in addition to the asymmetries with the purpose of comparing with other published results.

CHAPTER 2

The LHC and ATLAS

2.1 The LHC

The Large Hadron Collider (LHC) [53] is the largest circular synchrotron accelerator built nowadays. It is based at the European Organisation for Nuclear Research, CERN, housed in the same tunnel that was used by the Large Electron-Positron collider (LEP) [54]. The LHC ring has a circunference of about 26.7 km and it is divided in eight arcs and eight insertion regions (IR). Four of the insertion regions are reserved to accommodate the physics experiments. The other four insertion regions are used to install the systems to control the beams: one contains the radio frequency cavities (RF) that accelerate the protons and compensate the energy losses; other IR contains the beam dump system and the other two contain the collimator system, which is used to clean the beam from particles which deviate from the nominal trajectory and momentum. Each of the eight arcs contains 49 quadrupole magnets, that keep the beam focussed, and 154 superconducting Niobium-Titanium dipole magnets, that bend the beams in a circular path. Due to the maximum beam energy of 7 TeV, the dipole magnets have to generate and keep during operation a magnetic field of up to 8.33 T[1]. To achieve this high and reliable magnetic field, the dipole magnets are cooled down to 1.9 K with

[1]The energy stored in a beam in a circular accelator is $E \approx c \cdot e\rho B$, where c is the speed of light, e the electric charge of the accelerated particle, ρ the bending radius, and B the magnetic field strength [55]

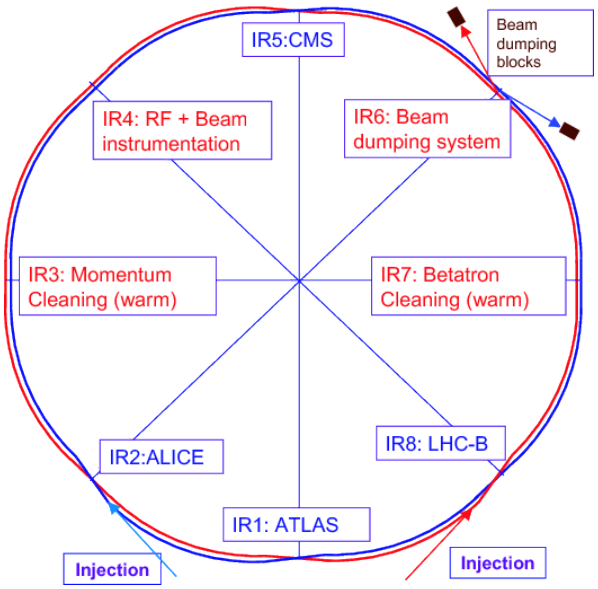

Figure 2.1: Schematic layout of the LHC complex [56].

super-fluid liquid Helium. The layout of the LHC is shown in Figure 2.1.

One important parameter of a collider is the number of events produced per second:

$$\frac{\mathrm{d}N}{\mathrm{d}t} = \sigma \mathcal{L}_{ins} \ , \tag{2.1}$$

where $\mathrm{d}N/\mathrm{d}t$ is the event production rate, σ is the cross-section of the process under study and $\mathcal{L}_{ins}$ is the collider instantaneous luminosity, which depends only on accelerator parameters:

$$\mathcal{L}_{ins} = \frac{f N_p^2 n_b \gamma_r}{4\pi \epsilon_n \beta^*} F(\theta, \sigma_z) \ , \tag{2.2}$$

where f is the bunch crossing frequency, N_p is the number of protons per bunch, n_b is the number of bunches, γ is the relativistic gamma factor, ϵ_n is the normalized emittance[2], β^* is the optical beta function at the collision point[3] and lastly $F(\theta, \sigma_z)$ is the geometrical luminosity reduction factor, related to the crossing angle and the density distribution of protons in a bunch. In Table 2.1 it is shown the design parameters values of the LHC together with the best values obtained for each parameter per year along the Run I. The evolution on the instantaneous luminosity in Run I, that almost reached its nominal design

[2]The emittance is a measure for the average spread of particle coordinates in position and momentum phase spaces.

[3]The optical beta function at the collision point is referred as the distance from the focus point in which the beam width is twice as wide as at the focus point.

Parameter	Nominal	2010	2011	2012
Beam energy [TeV]	7	3.5	3.5	4
Bunch spacing [ns]	25	150	50	50
Number of bunches	2808	368	1380	1380
Protons per bunch (10^{11})	1.15	1.2	1.45	1.65
β^*[m]	0.55	3.5	1.5/1	0.6
ϵ_n [μm]	3.75	2.4	2.4	2.5
Relativistic γ	7461	3730	3730	4263
Luminosity [$\text{cm}^{-2}\text{s}^{-1}$]	10^{34}	$2.1 \cdot 10^{32}$	$3.7 \cdot 10^{33}$	$7.7 \cdot 10^{33}$
Luminosity delivered [fb^{-1}]		0.048	5.46	22.8

Table 2.1: LHC running conditions for the nominal design and during the Run I data taking [53,57]. Each parameter value corresponds to the best performance achieved during the year.

value in 2012, is a sign of the good performance of the LHC.

Prior to being injected into the LHC ring, particles are accelerated in different sequential stages by using the CERN accelerator complex, that is shown in Figure 2.2. First, protons are stripped from Hydrogen atoms and are accelerated up to an energy of 50 MeV by a linear accelerator (Linac2). Then they are sent to the Proton Synchroton Booster (PSB), where protons reach an energy of 1.4 GeV. Later, the protons are injected to the Proton Synchroton (PS), where they are arranged in bunches in order to reach an energy of 25 GeV. After that, they are transferred to the Super Proton Synchroton (SPS), where the protons are accelerated up to 450 GeV, which is the injection energy of the LHC. Finally, the protons are accelerated up to 7 TeV in the LHC ring.

The idea of exploring the nature to the TeV scale arose more than thirty years ago. The concept of the LHC started in 1984 [58] even before the construction of the LEP. However, it was not possible to reach the TeV scale with the technology available in the 80's. The building of the LHC was approved in 1994 and its construction began in 1998, two years before LEP was decomissioned [59]. Even if the construction of the LHC and the experiments was completed in 2008, the collisions did not start until the end of 2009 due to an incident that happened during the initial attemp. During that initial run, an electrical failure led to an explosion affecting the cooling system and causing mechanical damage to several magnets [60]. After one year of repair, proton beams were successfully circulated at the injection energy (450 GeV) and the first *pp* collisions were produced on November 2009. In 2010 the beam energy was set to 3.5 TeV and the LHC delivered an integrated luminosity of 45 pb^{-1}at $\sqrt{s} = 7$ TeV. In 2011 the centre of mass energy was kept to $\sqrt{s} = 7$ TeV. The

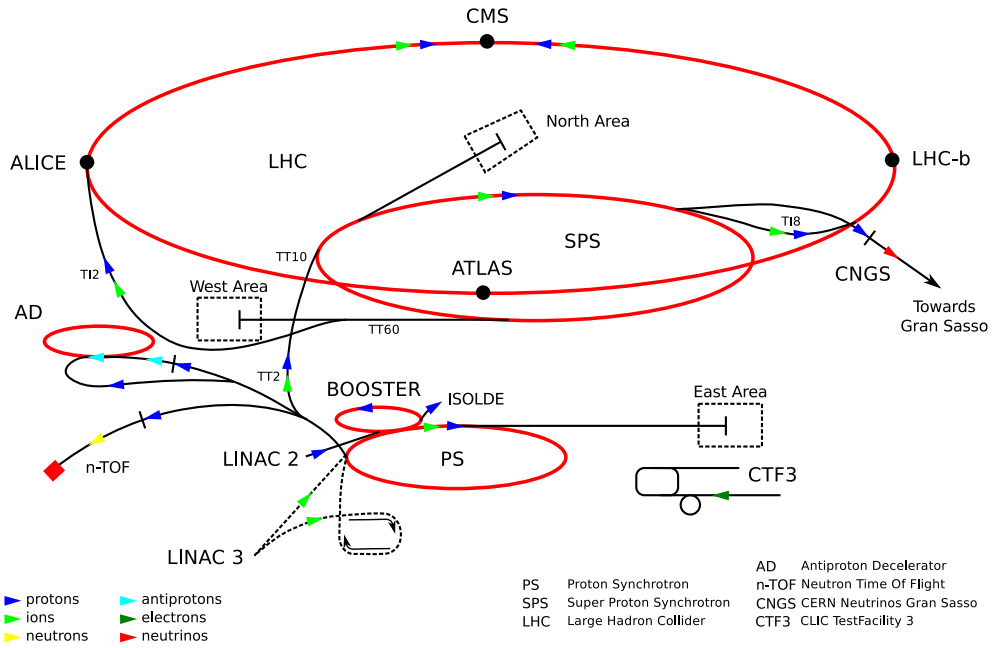

Figure 2.2: CERN accelerator complex and associated experiments.

instantaneous luminosity reached a value of $\mathcal{L}_{inst} = 3.65 \cdot 10^{33}\text{cm}^{-2}\text{s}^{-1}$ and the LHC delivered a total integrated luminosity of $\mathcal{L} = 5.46$ fb^{-1}. The campaign of 2012 beat all previous records: the centre of mass energy was raised from energies of 7 TeV to 8 TeV; the instantaneous luminosity almost reached the design value ($\mathcal{L}_{inst} = 7.7 \cdot 10^{33}\text{cm}^{-2}\text{s}^{-1}$); and the LHC delivered a total integrated luminosity of $\mathcal{L} = 22.8$ fb^{-1}, four times more data than the previous year and more than the luminosity accumulated by the Tevatron proton-antiproton collider of the Fermilab laboratory during its whole operation.

The data produced by the LHC is collected by different experiments located along the collider ring. There are four big experiments, which have their respective detector installed at one of the interaction points, as it is shown in Figure 2.1. The ATLAS (A Toroidal LHC ApparatuS) detector [61] located at Point 1 and the CMS (Compact Muon Solenoid) detector [62] at Point 5 are large, general purpose detectors designed to cover a wide range of physics. Their primary task is to explore the physics beyond the Standard Model especially from proton-proton collisions. The LHCb (LHC beauty) detector [63], located at Point 8, is designed to investigate topics related to the heavy quark flavours c and b with especial focus on the asymmetry of matter and antimatter observed in the universe. The ALICE (A Large Ion Collider Experiment) detector [64] placed at Point 2 is designed to study lead-ion collisions (PbPb)

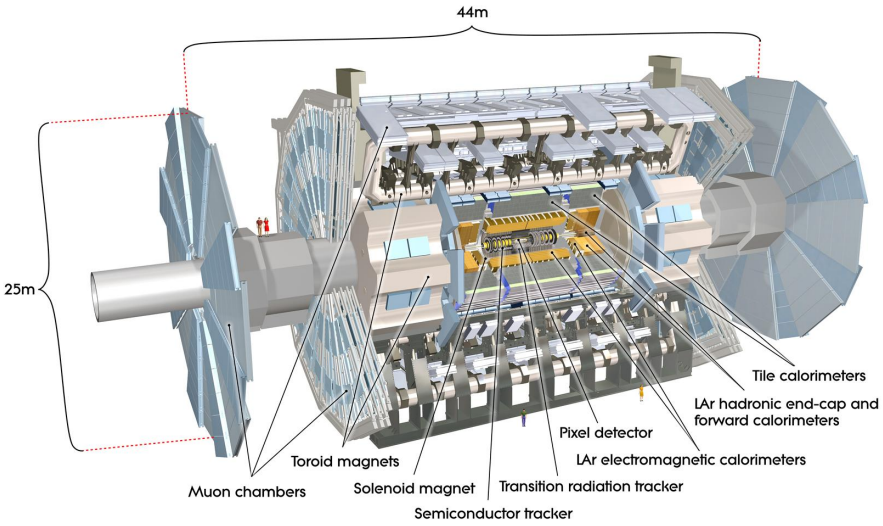

Figure 2.3: Schematic layout of the ATLAS detector.

to investigate the conditions of the early universe by creating extremely high matter densities. In addition to these big experiments, there are three smaller ones installed at the same interaction points, that are designed to study specific phenomena not covered by the physics programs of the main experiments already presented. The LHCf (LHC forward) [65] and TOTEM (TOTal Elastic and diffractive Meaurement) [66] experiments study particles produced in the very forward regions of the ATLAS and CMS respectively, which are too close to the beampipe to be recorded by the larger detectors. The MoEDAL (Monopole and Exotics Detector At the LHC) [67] experiment is installed in the same point as the LHCb, and searches for magnetic monopoles or particles with similar properties.

2.2 ATLAS detector

The ATLAS detector [61] is a general purpose experiment built to fully exploit the physics produced by the LHC. Its design, assembly and calibration as well as its overall preparation and operation have been a collaborative effort among the 37 nations and 2500 scientists who contribute to the ATLAS project. The detector is located $\sim$ 100 m underground. It is 44 m long and 25 m tall and weights 33 tones. It is composed by three sub-detectors installed around the beam pipe, following the layout shown in Figure 2.3. Each sub-detector is divided in a barrel and two end-caps. The barrel has

the form of a cylinder with the beam pipe in its axis and the end-caps are closing off the cylinder of the barrel in the forward regions. Each sub-detector has been designed to measure a specific property of the outgoing particles emerging from the collisions. The innermost sub-detector is the Inner Detector (ID), which is sensitive to charged particles. It is responsible of the pattern recognition, momentum measurement of charged particles and reconstruction of primary and secondary vertices. Surrounding the ID it is placed the solenoid magnet [68] with a 2 T magnetic field to bend the trajectories of the charged particles within the ID. Next sub-detectors are the calorimeters which are responsible of measuring the energy of the particles. The electromagnetic calorimeter is designed to measure the energy deposited by photons, electrons and positrons while the hadronic calorimeter is intended to measure the energy deposited by hadrons. The outermost sub-detector is the Muon Spectrometer (MS) which measures the momentum of muons, the only charged particle that can propagate through the calorimeters. The muon system also includes chambers for triggering on these particles. A toroidal magnet system is located together with the MS in order to bend the muons within the MS.

2.2.1 Muon Spectrometer

This spectrometer is the outermost part of the ATLAS detector and it is immersed in a large superconducting air-core toroid magnet, as it is shown in Figure 2.4. The large barrel toroid, composed by 8 superconducting coils, provides the magnetic bending over the range[4] $|\eta| < 1.4$. On the other hand, two end-cap toroids, also composed by 8 superconducting coils, bend the muons in the range $1.6 < |\eta| < 2.7$. This magnet configuration provides a field which is mostly orthogonal to the muon trajectory with a bending power up to 8 T m in the central region. The complex system of muon chambers is built out of separate trigger and high-precision tracking chambers. In the barrel region, muon tracks are measured in chambers arranged in three cylindrical layers around the beam axis while in the transition and end-cap regions the chambers are installed in planes perpendicular to the beam, also in three layers. Four different types of drift chambers are used in the muon system that are optimised for different purposes. Two of them provide precision muon tracking while the other are used for triggering muon candidates.

- **Monitored Drift Tubes (MDT):** they provide coverage in the region

[4]The pseudorapidity, η, is defined as $\eta = -\log(\tan(\theta/2))$ where θ is the polar angle measured with respect to the Z axis, which is parallel to the beam pipe.

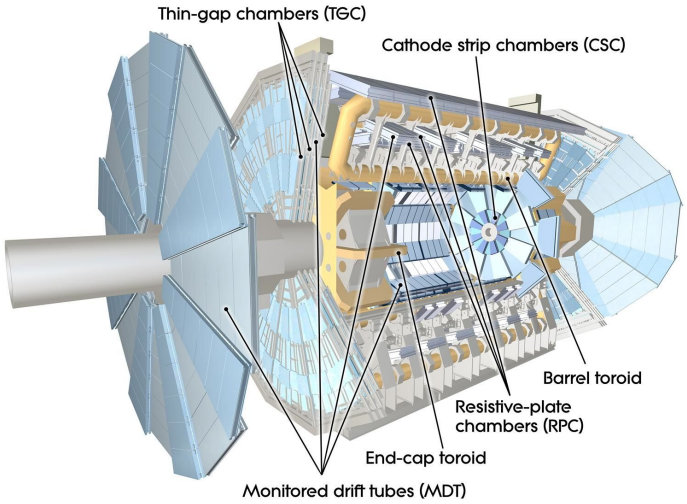

Figure 2.4: View of the Muon Spectrometer.

$|\eta| < 2.7$. They consist on drift tubes that measure the distance of a muon track to the wire located in the centre of the tube, providing high precision measurements of the tracks in the principal bending direction of the magnetic field.

- **Cathode Strip Chambers (CSC):** they are located in the inner-layer of the muon system covering the forward region, $2.0 < |\eta| < 2.7$. They are composed by multi-wire proportional chambers which provide a position resolution better than 60 μm. They are optimised to also withstand high event rates that are present in the forward regions.

- **Resistive Plate Chambers (RPC):** they are gaseous detectors that operate in avalanche mode. They are arranged in layers with the MDT or CSC sandwiched in between, covering the region $|\eta| < 1.5$. They provide trigger signals.

- **Thin Gap Chambers (TGC):** they are multi-wire proportional chambers that work in a similar manner as the RPC's and with the same purpose, but they are located in the forward region of the detector in $1.05 < |\eta| < 2.7$.

The muon system is designed to achieve a momentum resolution below 4% for muons which transverse momentum, p_T, is lower than 200 GeV, increasing to 10% for muons with $p_T = 1$ TeV.

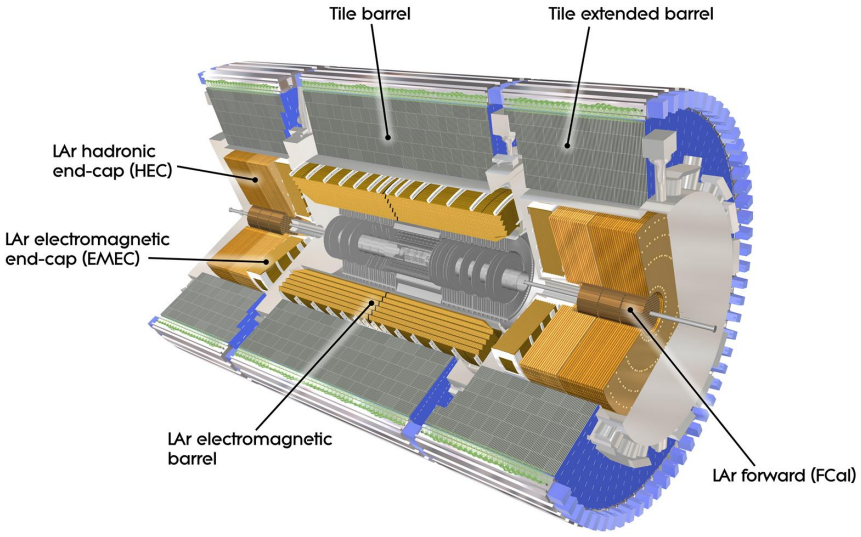

Figure 2.5: View of the ATLAS calorimeter system.

2.2.2 Calorimeters

The calorimeters in ATLAS measure the energy of charged and neutral particles as well as jets. They also detect the missing transverse energy by summing all of the measured energy deposits.

The layout of the calorimeters in ATLAS is shown in Figure 2.5. The calorimeter system covers the range $|\eta| < 4.9$ with full ϕ-symmetry. In the η region matched to the Inner Detector, the fine granularity of the electromagnetic (EM) calorimeter is ideally suited for precision measurements of electrons, positrons and photons. The coarser granularity of the rest of the calorimeter is sufficient to satisfy the physics requirements for jet reconstruction and missing transverse energy measurement.

The depth is an important design criterion for calorimeters since they should completely contain particle showers and limit the punch-through into the muon system. The total thickness of the EM calorimeter is greater than 22 radiation lengths[5] (X_0) in the barrel and greater than 24 radiation lengths in the end-caps. The radial depth of the Hadronic calorimeter is 7.4 interaction lengths[6] (λ) in the barrel and more than 10 interaction lengths in the end-caps.

[5] X_0 is the mean distance over which a high-energy electron loses all but $1/e$ of its energy by bremsstrahlung.

[6] λ is defined as the mean path length necessary to reduce the number of relativistic charged particles by a factor $1/e$ when passing through a certain material.

- **Electromagnetic calorimeter :** it provides energy measurement for particles that interact primarily via the electromagnetic interaction, such as electrons and photons. It is divided into a barrel part ($|\eta| < 1.475$) and two end-cap components ($1.375 < |\eta| < 3.2$), each housed in its own cryostat. The barrel calorimeter consists of two identical half barrels, separated by a small gap of 4 mm at $z = 0$. Each end-cap calorimeter (EMEC) is mechanically divided into two coaxial wheels, an outer wheel covering the region $1.375 < |\eta| < 2.5$ and an inner wheel covering the region $2.5 < |\eta| < 3.2$. It uses liquid argon (LAr) as active detector medium, which was chosen for its intrinsic linear behaviour, its stability of response over time and its intrinsic radiation-hardness. On the other hand, the passive absorber medium is made of lead plates. The lead plates are arranged in layers with the LAr sandwiched in between with accordion geometry, providing a complete ϕ symmetry without azimuthal cracks. The expected energy resolution in the EM calorimeter is $\frac{\sigma_E}{E} = \frac{10\%}{\sqrt{E}} \oplus 0.7\%$.

- **Hadronic calorimeter :** it uses two different technologies: scintillator-tile in the barrel region ($|\eta| < 1.7$) and liquid argon in the end-caps ($|\eta| > 1.5$). Since hadronic showers are much longer and wider than electromagnetic showers, the hadronic calorimeter needs to be much thicker than the EM calorimeter. The barrel part, called the Tile Calorimeter (TileCal), is placed directly outside the EM calorimeter envelope and is separated into a large central barrel ($|\eta| < 1.0$) and two smaller extended barrel cylinders ($0.8 < |\eta| < 1.7$) on each side (Tile extended barrel). The TileCal uses steel plates as the absorber and scintillating tiles as the active material. The end-cap part, called the Hadronic End-cap Calorimeter (HEC), is located directly behind the end-cap electromagnetic calorimeter and consists of two independent wheels per end-cap. The HEC extends from $1.5 < |\eta| < 3.2$, thereby overlapping with the Forward Calorimeter and the TileCal. The HEC uses liquid argon as the active medium and copper plates as the absorber material, arranged in a parallel-plate geometry. The expected energy resolution of the barrel and end-cap calorimeters is $\frac{\sigma_E}{E} = \frac{50\%}{\sqrt{E}} \oplus 3\%$ for single pions.

- **Forward calorimeter :** (FCal) it covers the region $3.1 < |\eta| < 4.9$ and is about 10λ deep. It is split longitudinally into three modules, the first one uses copper as absorber material and provides a good optimization

of the EM measurements while the other two modules use tungsten as absorber material to measure the energy of hadronic interaction. All of them use LAr as active material. The FCal is integrated into the end-cap cryostats, which provides a more uniform coverage and reduces the radiation background levels in the Muon Spectrometer. The expected energy resolution is $\frac{\sigma_E}{E} = \frac{100\%}{\sqrt{E}} \oplus 10\%$ for single pions.

2.2.3 Inner Detector

The Inner Detector (ID) is the innermost ATLAS detector and it is designed to measure the trajectory, also often referred to as track, of charged particles. The ID is composed by three sub-detectors: Pixel detector, Semi-Conductor Tracker detector (SCT) and Transition Radiation Tracker detector (TRT), and its layout is shown in Figure 2.6. The ID has a length of 7 m and a diameter of 2.3 m, surrounding the LHC beam pipe with the interaction point in its centre and covering a range of $|\eta| < 2.5$. It is immersed in a magnetic field of 2 T along the z axis provided by a superconducting solenoid, which allows the measurement of the transverse momentum, p_T, by measuring the curvature of charged particles. The solenoid has a diameter of 2.5 m and its length is 5.3 m, thus shorter than the ID. Because of this, the magnetic field is non-uniform towards the end-caps. Nevertheless these inhomogeneities are mapped and included in the track reconstruction algorithms, thus with no major impact on further physics analysis.

- **Pixel detector :** it is composed by 1744 identical silicon pixel modules. Each module consists of a silicon sensor of area 63.4×24.4 mm^2 with a pixel size of 50×400 μm^2. In the barrel region, the detector elements are arranged on concentric cylindrical layers around the beam axis, while in the forward regions they are mounted on disks perpendicular to the beam axis. There are three layers in the barrel and three disks in each end-cap, so that on average each track produces three hits in the Pixel detector. The intrinsic resolution of the pixel detector is 10 μm in the shortest pixel direction, and 115 μm in the long pixel direction, which corresponds to the beam pipe direction for the barrel modules and with the radial direction for the end-cap ones.

- **SCT detector :** it surrounds the pixel detector and it is composed by 4088 modules. Each module is composed by two silicon micro-strips sensors of 80 μm pitch that are glued back-to-back with a stereo angle

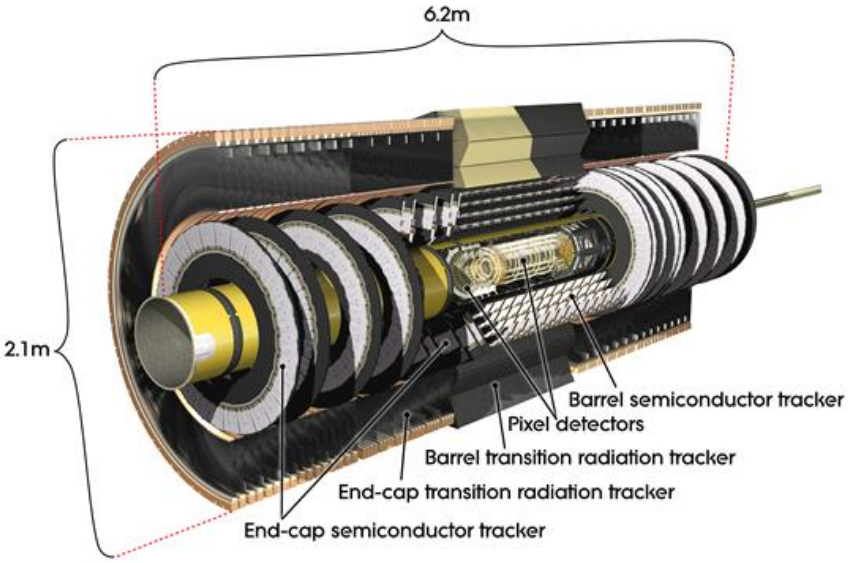

Figure 2.6: View of the ATLAS Inner Detector.

of 40 mrad. The SCT modules are arranged on four cylindrical layers in the barrel region and on nine discs in each end-cap. In both the barrel and the end-cap, the modules are mounted such that each track will encounter eight strip layers on average. The intrinsic accuracies per module are 17 μm across the strips, and 580 μm along the strips.

- **TRT detector :** it is the outermost sub-detector in the Inner Detector. It is composed by $\sim$ 300.000 straw tubes. Each straw is 4 mm diameter with a gold-plated tungsten wire in the middle filled with a mixture of gases. The TRT produces on average 30 hits per track with an intrinsic resolution of 130 μm in the perpendicular direction to the straw.

The combination of precision silicon trackers at small radius with the straw tracker in the outermost part of the ID provides high-precision and a robust pattern recognition in both $r\phi$ and z coordinates. The silicon detectors allow precise measurements of the impact parameter as well as high accuracy for both primary and secondary vertex reconstruction. This is very important for instance in the context of the heavy flavour where jets originating from b-hadrons can be identified. The straw tracker, i.e. the TRT, provides continuous tracking to enhance the pattern recognition and significantly improves the momentum resolution due to the large number of hits measured and the longer track length. The straw tracker also provides electron identification,

complementary to that of the calorimeter, by detecting transition-radiation photons in the gas mixture of the straw tubes.

2.2.4 The trigger system

The ATLAS trigger system is designed to reduce the event rate produced by the LHC, that can be up to 40 MHz, down to an event rate that can be handled by the data acquisition system by rejecting events with no interesting physics signatures. It is divided in three levels called level-1 trigger (L1) [69], level-2 trigger (L2) and the event filter [70]. The L1 uses custom made electronics and is directly integrated in the hardware of the detectors. It makes use of the electromagnetic and hadronic calorimeters as well as the muon triggers from the muon system. It selects or rejects an event in 2.5 μs, providing an output rate to the next step of 75 kHz. The next filter is a two-step software-based trigger called High Level Trigger (HLT) that processes the events in a processor farm. The first step of the HLT is the L2 trigger, that uses regions of interest defined by the L1 trigger. The events are analysed using the full granularity from all sub-detectors within the region of interest. The L2 processes an event in 10 ms and reduces the output rate to 1 kHz. Finally, the event filter uses the fully reconstructed event and selects an event within a few seconds, reducing the output to $\sim$ 200 Hz. An important property of the trigger is the so-called prescale. The cross-section of some processes is several orders of magnitude larger than the cross-section of other processes of interest, thus, the former events would make use of a large fraction of the trigger bandwidth, reducing the capacity to select the latter ones. In order to prevent the loss of rare processes a prescale is applied to a trigger criterion. For instance, a prescale value of 1000 applied to a trigger criterion would cause the trigger to only fire each thousandth time although its requirements are fulfilled

2.2.5 The computing system

The huge amount of data produced by the LHC, around 15 petabytes per year, should be stored in a efficient way and also accessible by thousands of scientist world-wide, ensuring enough computing power to carry out the large amount of analyses that are performed everyday. To fulfil these requirements on storage and computing power capabilities, the LHC developed a Grid technology [71] which is managed by the Worldwide LHC Computing Grid (WLCG) [72, 73], the LHC experiments and the computing centres from the institutions participating in the LHC physics program.

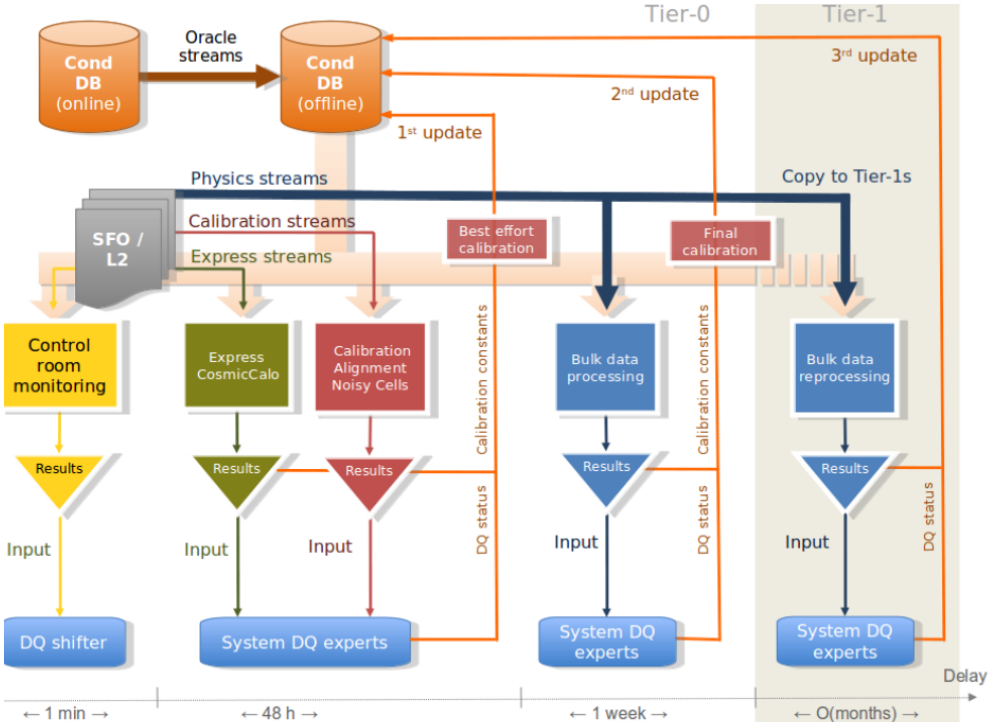

Figure 2.7: The ATLAS data quality operation scheme in 2012.

The ATLAS data distribution model [74] presents a hierarchy structure of sites called Tiers, where each level in the hierarchy has a definite role within the grid. A permanent copy of the ATLAS raw data is stored at the only Tier-0 hosted at CERN. After the first pre-processing, data are transferred to 10 Tier-1 around the world. These Tiers centres perform the full event reconstruction and also accept analysis jobs submitted from different institutes. The Tier-2 sites have a copy of a portion of data with certain interest and they are responsible to generate the Monte Carlo simulations. There are around 80 Tier-2 and they also accept analysis jobs from other institutions. Finally, the last level of the hierarchy are the Tier-3 sites, which are the analysis computing resources under the control of individual institutes and finally dedicated to physics analysis tasks.

2.2.6 ATLAS performance in Run I

The data delivered by the LHC is recorded within streams such as the physics stream, the calibration stream and the express stream. These streams are defined with a dedicated trigger setup. The physics stream is used for data analysis, and is defined from sets of triggers focusing on specific final state

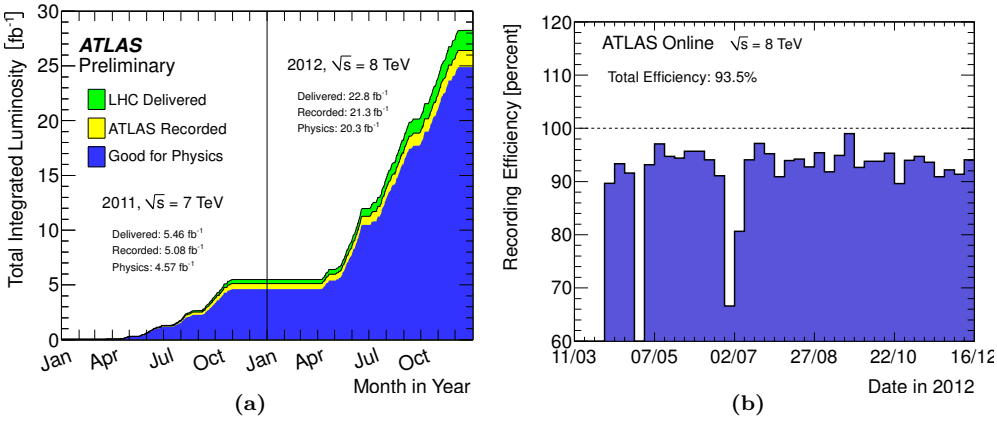

Figure 2.8: On the left (a), it is shown the cumulative luminosity versus time delivered by the LHC (green) and recorded by ATLAS (yellow). The cumulative luminosity certified to be good quality data during stable beams and for pp collisions at 7 and 8 TeV centre-of-mass energy in 2011 and 2012 is represented in blue colour. On the right (b), it is shown the data taking efficiency in 2012 per week [75].

objects like electromagnetic clusters, jets, missing transverse energy, etc. The calibration stream contains specific events for several detectors and are used to compute the alignment and calibration constants for the detectors. Finally, the express stream contains a reduced fraction of the data ($\sim 4\%$) and it is used for data quality purposes. Figure 2.8(a) shows the integrated luminosity during 2011 and 2012 that corresponds to the physics stream. The luminosity delivered by the LHC is shown in green while the luminosity registered by ATLAS is shown in yellow, and as can be seen, a small fraction of data could not be recorded. The registered data declared good for physics analyses is shown in blue. The role of the calibration and express streams is to guarantee, through their evaluation, the highest quality assessment and reconstruction of the physics data [76]. Therefore, it is mandatory to process these streams before the physics stream would be delivered to the ATLAS collaboration. The calibration and express streams are processed at Tier-0 at CERN, where the monitoring tools are deployed, and at this stage shifters and experts update the conditions databases used to store the complete picture of the detector status, the calibration and the alignment constants. An example of these tools is the web application developed for the monitoring of the ID alignment constants run by run, that will be explained in next chapter. All these tasks must be completed within 48 hours, before the start of the bulk data processing. This process, known as the *calibration loop* [77, 78], is the first part of the quality operation scheme of ATLAS (see Figure 2.7) and thanks to this effort, the efficiency of the data taking during the 2012 was 93.5% (see Figure 2.8(b))

and over 90% for the Run I. The data used in this thesis was recorded during 2011, for alignment studies, and in 2012, for alignment and top quark physics studies, which benefits of all these processes already described ensuring the highest data quality available at the moment.

CHAPTER 3

Inner Detector Alignment

The knowledge of the exact position of the detector elements in the Inner Detector determines the resolution with which a particle trajectory can be reconstructed. Usually, the position of every detector element changes over time due to different causes such as the assembly of detector components, changes in the magnet system, etc. In order to correct for this and provide the best description of the Inner Detector, an alignment algorithm based on tracks is used. This chapter describes briefly the basics of the ID alignment and the strategy followed during the 2012 data taking period.

3.1 Alignment requirements

Almost all physics analyses performed using the data recorded by the ATLAS detector rely on particle reconstruction and identification algorithms that utilize tracks in their functioning. For instance, b-tagging algorithms, primary and secondary vertex finders and lepton reconstruction are some of the algorithms for which an excellent track reconstruction is mandatory to carry out, for example, precision measurements of particle properties or to measure production rates of certain processes. However, only using devices with both high granularity and resolution in the ID will not guarantee the expected excellent performance. In addition, a good detector calibration and alignment is needed to fully exploit the capabilities of the ID. Uncertainties in the exact position of every single detector element have been introduced during the assembly

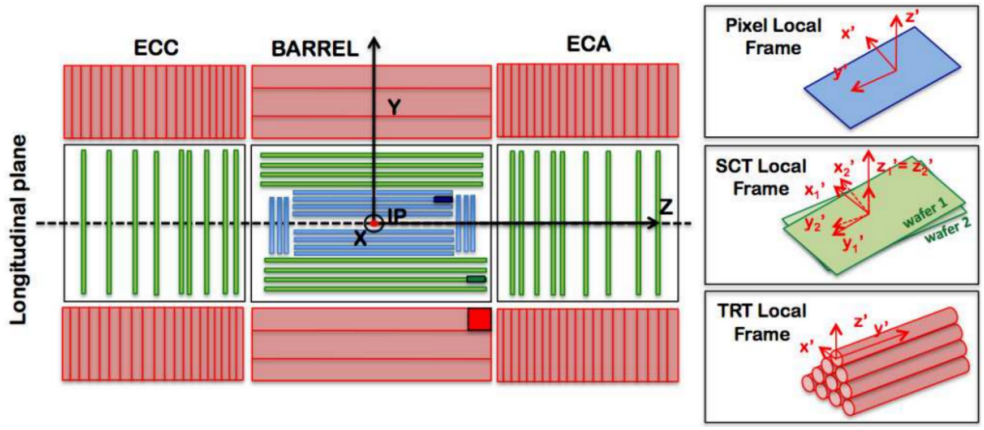

Figure 3.1: Left: Schematic representation of the longitudinal plane of the inner detector showing the Pixel (blue), the SCT (green) and the TRT (red). The global coordinate system is shown with the origin at the centre of the detector. Right: Local coordinate frame of the different devices.

and installation of the detector and also during the operation, as a result of changes in temperature of the cooling system, the ramping of the magnetic field, etc.

In order to achieve the ATLAS physics goals, the degradation of the track parameters due to the ID alignment must be lower than 20% with respect to their intrinsic resolution. This means that the required resolution of the alignment for Pixels and the SCT must be 7 μm and 12 μm respectively in the bending plane, and a resolution of 170 μm per straw for the TRT [79]. Consequently, due to its impact on the further physics analyses, the ID alignment is one of the crucial tasks to be accomplished before data can be delivered to analysers.

3.1.1 The ATLAS coordinate systems

From the different coordinate systems used in ATLAS, the ones that are relevant for the alignment of the ID are: the Global coordinate frame, where we define the module's position in space, and the Local coordinate frame, where we reconstruct the hits of the tracks.

Global coordinate frame

The global coordinate frame (X, Y, Z) shown in Figure 3.1, is a right-handed Cartesian coordinate system with the origin defined at the nominal interaction point of the proton-proton collisions. The Z axis is parallel to the beam, coinciding the positive Z direction with the solenoid magnetic field. The

positive X direction points to the centre of the LHC ring while the positive Y direction points towards the Earth's surface. Within this coordinate system we define the variables ϕ, η, and θ. The azimuthal angle $\phi \in (-\pi, \pi]$ is measured in the X-Y plane where the positive X axis corresponds to $\phi = 0$ and the positive Y axis to $\phi = \pi/2$. The polar angle $\theta \in [0, \pi]$ is measured with respect to the Z axis, with $\theta = 0$ in the positive Z direction. Finally, the pseudorapidity η is defined as $\eta = -\log(\tan(\theta/2))$. Although these variables are not used to describe the geometry of the detector, they are useful to describe the kinematics of the event.

Local coordinate frame

The local coordinate frame (x, y, z), also illustrated in Figure 3.1, is a local right-handed Cartesian reference system that is defined for each module. The origin is located at the geometrical centre of the device and the position of the different axes depends on the type of the module:

- In the Pixel modules, the x and y axes are defined within the detector plane. The x axis is parallel to the most precise measurement direction, which coincides with the direction along the short side of the module, while the y axis is parallel to the long side of the module, being the less precise measurement direction. The x axis is orientated along the ϕ axis in the global coordinate frame.

- As it was mentioned in section 2.2, the sensitive part of the SCT modules is composed by two micro-strips wafers assembled back to back. Hence, in SCT modules there are two x and y axes, each of them defined within the surface of each wafer, but sharing the same z axis. As in the case of the Pixel modules, the x axis is parallel to the short side of the wafer, being the most precise measurement direction, while the y is parallel to the long side of the wafer, being the less sensitive one. The x axis orientated along the ϕ axis in the global coordinate frame.

- In the TRT straws, the y axis points along the wire, which is the less precise measurement direction, while the x axis is perpendicular to both the y axis and the radial direction from the origin of the global coordinate frame to the straw centre.

The hits are reconstructed in the local coordinate frame of the different modules. While for the Pixel modules the reconstruction it is straight forward,

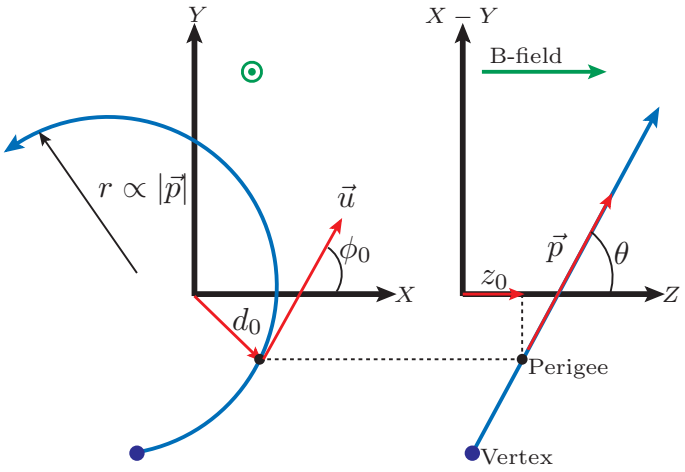

Figure 3.2: Track parameters

in the case of the SCT the information from the two local frames associated to the hit are used to reconstruct it. Finally, the x coordinate of the hit reconstructed by the TRT is associated to the radial distance to the straw.

3.1.2 Track parameters

Figure 3.2 shows the track parameters used for the ID alignment. The track representation uses five parameters $\boldsymbol{\pi} = (d_0, z_0, \phi_0, \theta, q/p)$[1], where the first two parameters represent the position of the track while the other three parameters represent the momentum of the charged particle with respect to a reference point. From the alignment and the physics perspectives, the most interesting representation is the one in which the track is parametrized with respect to the perigee, which is the point of closest approach of the track to the global Z axis. In this representation, d_0 is the transverse impact parameter, defined to be positive when the direction of the track is clockwise with respect to the origin. z_0 is the longitudinal impact parameter and it has the same sign as the one of the Z axis. ϕ_0 and θ are the azimuthal and polar angle respectively. And finally, the parameter q/p where q is the charge of the particle and p its momentum, provides information about the curvature of the track [80].

[1]From now on, bold variables will represent vectors.

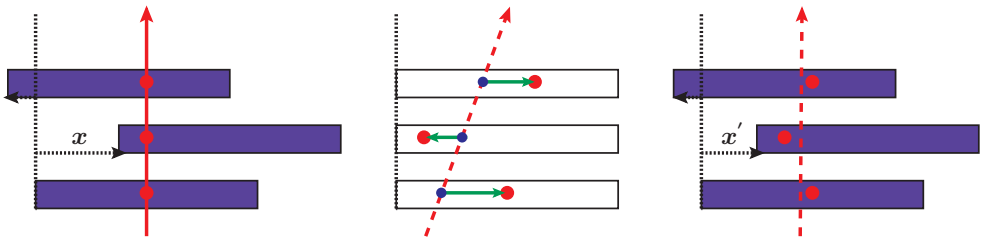

Figure 3.3: Schematic picture of the alignment process. The figure on the left represents the real geometry of the detector with the real track in solid red and one hit in each module in red. The figure on the middle represents the apparent detector position. The reconstructed track is represented in dashed red. The intersection point between the reconstructed track and each module is represented with blue points while the residuals are represented by green lines. The figure on the right represent the detector after apply the alignment corrections.

3.1.3 Residuals

The last key ingredients for the alignment are the residuals of the track. Within the context of tracking and alignment, a residual is the distance between a hit[2] and the intersection point of the reconstructed track in the sensor. Thus, we can define the residual as $r = (\mathbf{m} - \mathbf{e}(\boldsymbol{\pi}, \mathbf{a})) \cdot \mathbf{u}$, where $\mathbf{m}$ is the position of the measured hit, $\mathbf{e}$ is the intersection point of the reconstructed track in the sensor and $\mathbf{u}$ is an unitary vector pointing along the sensing direction[3]. As it is expected, the intersection point $\mathbf{e}$ depends on the track parameters ($\boldsymbol{\pi}$) and on the alignment ones ($\mathbf{a}$)[4]. The position of the hit ($\mathbf{m}$) is measured in the local frame and then it does not depend on the position of the module, meaning that it does not depend on the alignment parameters. The better the quality of a track, the lower the residuals are. To that end, not only good reconstruction algorithms are needed but also the precise knowledge of the location of the modules plays an important role.

3.2 Track based alignment

As said before, the primary goal of the ID alignment is to determine the position and orientation of each sensing device. During the assembly of the ID, measurements on the position of the different alignable structures were done, providing an initial geometry of the detector [81]. After its assembly and installation in the ATLAS cavern, the ID detector has not been accessible

[2] A hit is a signal in the detector produced by the impact of a particle. This signal is a cluster of pixels/strips in the Pixel and SCT, and a drift circle in the TRT.

[3] The sensing direction depends on the type of the module where the residuals are going to be measured. In the case of a pixel module, there are two sensing directions which coincide with the x and y coordinates in the local coordinate frame.

[4] The alignment parameters will be defined in section 3.2.1

with the purpose of updating its geometry and particularly when ATLAS has been in operational mode during data taking. Then, to tackle this problem, we perform an indirect measurement of the position of each alignable structure using track-based alignment algorithms. In picture 3.3, it is shown the basics of the ID alignment. On the left sketch in Figure 3.3, the real positions of the modules with their relative displacements are shown in blue, while the real trajectory of the charge particle and its hits on the modules are shown in solid red. In the middle of the picture, the white modules represent their apparent position according to our knowledge on the geometry of the detector. The track is reconstructed according to the hits and the apparent position of the modules, shown in dashed red. The green arrows represent the residuals associated to each hit. Then, taking this information into account, we try to update the geometry of the detector by using algorithms that minimize the residuals of the track with respect to the module's position. Finally, on the right of the picture, we have a corrected geometry, that is not yet perfect, but ensures a high quality on the reconstructed track.

Within the ATLAS software framework, there are several track-based algorithms implemented. All of them were tested and used during commissioning and detector operation, as for example the *Robust* algorithm [82]. However, the methods used during operation in the Run I to align the ID were the *Local* χ^2 [83] and *Global* χ^2 [84] algorithms. Both methods are based on the minimization of the χ^2 function of the residuals, but with a different approach, as described in detail in the following section.

3.2.1 χ^2 minimization and alignment parameters

The alignment constants, that are the corrections to the position and orientation of each alignable structure[5], are those obtained as a result of the minimization of the χ^2 function built from track-hit residuals:

$$\chi^2 = \sum_t \sum_h \left(\frac{r_{th}(\boldsymbol{\pi}, \mathbf{a})}{\sigma_h} \right)^2 , \tag{3.1}$$

where t is the set of reconstructed tracks and h the set of hits associated to each track t. r_{th} is the residual of each hit associated to the track t and σ_h its associated hit error. We can write the previous equation in a more convenient

[5]The vector of alignment constants $\mathbf{a}$ contains all degrees of freedom being aligned. In general it will be a repetition of the basic vector $\widetilde{\mathbf{a}} = (T_x, T_y, T_z, R_x, R_y, R_z)$ for every structure aligned, where T_i and R_i represent the translation along the i axis and the rotation around the i axis respectively.

way using vector notation:

$$\chi^2 = \sum_t \mathbf{r}_t(\boldsymbol{\pi}, \mathbf{a})^T V^{-1} \mathbf{r}_t(\boldsymbol{\pi}, \mathbf{a}) \ . \tag{3.2}$$

In this representation, the hit error can be decoupled from the residual, with the matrix V being the covariance matrix of the hit errors. If we perform the total differential of the χ^2 function we obtain:

$$d\chi^2 = \underbrace{\frac{\partial \chi^2}{\partial \boldsymbol{\pi}} d\boldsymbol{\pi}}_{a} + \underbrace{\frac{\partial \chi^2}{\partial \mathbf{a}} d\mathbf{a}}_{b} \rightarrow \frac{d\chi^2}{d\mathbf{a}} = \frac{\partial \chi^2}{\partial \boldsymbol{\pi}} \frac{d\boldsymbol{\pi}}{d\mathbf{a}} + \frac{\partial \chi^2}{\partial \mathbf{a}} \ . \tag{3.3}$$

As we can see, the differential function has two terms, the term a related with the track parameters and the term b related with the alignment parameters. Then, when performing the total derivative with respect to the alignment parameters, we are introducing an important relationship between the track and alignment parameters through the term $d\boldsymbol{\pi}/d\mathbf{a}$, that is going to make the difference between the *Local* χ^2 and the *Global* χ^2 algorithms.

The *Local* χ^2 algorithm assumes that the track parameters do not depend on the alignment ones ($d\boldsymbol{\pi}/d\mathbf{a} = 0$). Then, the total derivative in Equation 3.3 is reduced to the partial derivative with respect to the alignment parameters, the track parameters being constants. On the other hand, the *Global* χ^2 algorithm is based on the assumption that the track parameters depend on the alignment ones ($d\boldsymbol{\pi}/d\mathbf{a} \neq 0$). Hence the χ^2 function is minimised by fitting simultaneously all tracks and alignment parameters. This can be easily understood since the corrections on the position of each module will relocate the hits, producing a new reconstructed track.

Applying the minimisation condition to the χ^2 function with respect to $\mathbf{a}$, and using Equation 3.2 we obtain:

$$\frac{d\chi^2}{d\mathbf{a}} = 0 \rightarrow \sum_t \left(\frac{d\mathbf{r}_t(\boldsymbol{\pi}, \mathbf{a})}{d\mathbf{a}} \right)^T V^{-1} \mathbf{r}_t(\boldsymbol{\pi}, \mathbf{a}) = 0 \ . \tag{3.4}$$

Entering the alignment and track corrections into Equation 3.4 via the Taylor's expansion of the residuals up to first order, one obtains:

$$\boldsymbol{r} = \mathbf{r_0} + \frac{\partial \mathbf{r}}{\partial \boldsymbol{\pi}} \delta\boldsymbol{\pi} + \frac{\partial \mathbf{r}}{\partial \mathbf{a}} \delta\mathbf{a} = \mathbf{r_0} + \left(\frac{\partial \mathbf{r}}{\partial \boldsymbol{\pi}} \frac{d\boldsymbol{\pi}}{d\mathbf{a}} + \frac{\partial \mathbf{r}}{\partial \mathbf{a}} \right) \delta\mathbf{a} = \boldsymbol{r_0} + \frac{d\mathbf{r}}{d\mathbf{a}} \delta\mathbf{a} \ ; \tag{3.5}$$

in which the term $d\boldsymbol{\pi}/d\mathbf{a}$ appears again. We will keep from now on the full term to generalise ($d\boldsymbol{\pi}/d\mathbf{a} \neq 0$), as the *Local* χ^2 is a particular case of the

Global χ^2 approach. Inserting Equation 3.5 into 3.4 we obtain the following expression:

$$\left[\sum_t \left(\frac{d\mathbf{r}}{d\mathbf{a}}\right)^T V^{-1} \left(\frac{d\mathbf{r}}{d\mathbf{a}}\right)\right] \delta\mathbf{a} + \sum_t \left(\frac{d\mathbf{r}}{d\mathbf{a}}\right)^T V^{-1}\mathbf{r}_0 = 0 \ . \tag{3.6}$$

We can now define the alignment matrix and vector:

$$\mathcal{M}_a = \sum_t \left(\frac{d\mathbf{r}}{d\mathbf{a}}\right)^T V^{-1} \left(\frac{d\mathbf{r}}{d\mathbf{a}}\right); \qquad \mathfrak{v}_a = \sum_t \left(\frac{d\mathbf{r}}{d\mathbf{a}}\right)^T V^{-1}\mathbf{r}_0 \ . \tag{3.7}$$

Therefore, Equation 3.6 can be re-written as:

$$\mathcal{M}_a\delta\mathbf{a} + \mathfrak{v}_a = 0 \rightarrow \delta\mathbf{a} = -\mathcal{M}_a^{-1}\mathfrak{v}_a \ . \tag{3.8}$$

Then, after the inversion of the alignment matrix we obtain the correction $\delta\boldsymbol{a}$ to the initial parameters with the final solution being $\boldsymbol{a} = \boldsymbol{a}_0 + \delta\boldsymbol{a}$. If the initial estimate of the alignment parameters is far from the real position, then several iterations of the alignment algorithm will be needed in order to recover the full correction.

The way to tackle the solving step depends on the setup used to perform the alignment. Depending on the number of the alignable structures used, each one contributing with up to 6 degrees of freedom (DoF), the size of the alignment matrix may vary from few tens of DoF to many thousands when aligning the ID at module level. As pointed out before, the *Global* χ^2 algorithm correlates all the alignable structures crossed by the same track, making the alignment matrix dense and therefore increasing the difficulty to solve the linear system derived from Equation 3.8. This is not a problem when we are aligning large structures or the size of the alignment matrix is not too big. However, when we attempt to align the ID at the module level, solving the linear system becomes challenging from the computational point of view. A practical way of making the alignment matrix sparse is by using the *Local* χ^2 algorithm. In this case, the track parameters are frozen ($d\boldsymbol{\pi}/d\mathbf{a} = 0$) and the correlation between different alignable structures is discarded. The alignment matrix becomes block diagonal, and therefore the matrix inversion is much less CPU time consuming than the *Global* χ^2 one. On the other hand, we will need to perform more iterations to reach the final alignment corrections than using the *Global* χ^2 method instead.

3.2.2 Weak modes

Whilst the alignment algorithms described previously can produce a description of the detector geometry which provides an efficient and good quality track fit, they cannot fully guarantee that the track parameter reconstruction is free from systematic biases. It is possible to find distortions in the detector geometry which preserve the track model but lead to biased physics measurements, such as the measurement of the invariant mass of the Z boson. These are called *weak modes*, as they correspond to near singular modes of the solution of Equation 3.8. The weak modes are collective detector deformations, real or introduced as artefacts of the alignment procedure itself, that transform one helical trajectory into another helix. The χ^2 of the reconstructed tracks and the track-hit residuals remain invariant under the presence of these weak modes.

The biases introduced by the weak modes into the track parameters have a significant impact on physics measurements, taking into account that the most affected track parameters are the momentum and the impact parameters. This makes the study of the quality of the track-hit residuals insufficient to ensure a good quality alignment of the ID. To tackle this problem, we introduce additional constraints to the alignment algorithms that can be applied to either the reconstructed parameters of the tracks used as input to the alignment algorithm or to the alignment parameter themselves. An example of the former type of constraint are the kinematic constraints of the decay $Z \rightarrow \mu^+\mu^-$, which is used to measure biases on momentum as well as biases in the impact parameters. An example of the latter type of constraint is the modularity of the algorithms used, that allows the alignment of each alignable structure independently from the others, at different levels of granularity and choosing the degrees of freedom that are allowed to move. The work done for this thesis in the so-called $Z \rightarrow \mu\mu$ method in order to remove the weak modes will be discussed in Sections 3.3.3 and 3.3.5.

3.2.3 Alignment levels and degrees of freedom

The alignment levels follow the assembly hierarchy, starting by aligning the largest structures to finally align every sensing device. First we align the largest structures, such as the Pixel detector and SCT barrel and end-caps. These structures have the largest misalignments but require less statistics and to perform less iterations of the alignment algorithms to accurately determine

Setup	Description	Structures	DoF	Constraints
1	Pixel fixed			
Global χ^2	SCT barrel	1	All	
	SCT end-caps	2	All	
	TRT barrel	1	All except T_z	
	TRT end-caps	2	All except T_z	
	Total	6	33	
2	Pixel barrel layers	3	All	
Global χ^2	Pixel end-caps discs	6	T_x, T_y, R_z	
	SCT barrel layers	4	All	Beam spot,
	SCT end-caps discs	18	T_x, T_y, R_z	Momentum bias and
	TRT barrel	1	All except T_z	Impact parameter bias
	TRT end-caps	2	All except T_z	
	Total	34	129	
Si 3	Pixel barrel modules	1456	All	
Global χ^2	Pixel end-caps modules	288	T_x, T_y, R_z	
	SCT barrel modules	2112	All	Beam spot,
	SCT end-caps modules	1976	T_x, T_y, R_z	Momentum bias and
	TRT barrel modules	96	T_x, R_z	Impact parameter bias
	TRT end-caps wheels	80	T_x, T_y, R_z	
	Total	6008	28632	
TRT 3	Pixel and SCT are fixed			
Local χ^2	TRT straw level	351k	T_x, R_z	
	Total	351k	702k	

Table 3.1: Summary of the alignment configurations used throughout 2012. The beam spot constraint forces the tracks to be originated at the beam spot.

their alignment constants. The next level of alignment follows after having aligned the large structures, if that would be needed. When the alignable structures decrease in size, for example the SCT barrel is split into barrel layers, their alignment corrections will become smaller with respect to the ones obtained in the previous level. By contrast, they require more statistics and more iterations of the alignment algorithms in order to obtain a good set of alignment constants. This is easily understood since we are aligning smaller structures, the alignment matrix becomes bigger and dense, thus making the solving step of Equation 3.8 more challenging. On top of that, each alignable structure needs at least one track crossing it in order to be aligned. The "canonical" alignment levels can be classified as follows:

- **Level 1 :** the Pixel detector is treated as a unique element while the SCT and TRT are both split in three structures, the barrel and two end-caps.

- **Level 2 :** the Pixel and SCT barrel are split in layers and the end-caps in discs. The TRT barrel is separated in modules and the end-caps in wheels.

- **Level 3 :** this level aligns at the finest granularity. The Pixel and SCT

are aligned at module level while the TRT is aligned at straw level.

Thanks to the modularity of the alignment software, we can prepare different setups for the alignment procedure. We can require different granularity levels to different sub-detectors independently from each others as well as to select the DoF to be used for the different structures. The DoF that are considered depend on both the expected misalignment and on the sensitivity of the alignable structure to corrections on each DoF. In Table 3.1 the different setups used for the alignment of the ID in 2012 are shown.

3.3 Alignment results in 2012

In this section, the alignment procedure performed in 2012 is explained with special focus on the contributions of this thesis to this effort [85].

Data selection

Two types of samples collected with the ATLAS detector from proton-proton collisions produced by the LHC at $\sqrt{s} = 8$ TeV are used for the 2012 campaign. The first sample is based on sets of good quality tracks which are used as an input to the alignment algorithms. The tracks used are required to have transverse momentum of at least 10 GeV, pass through at least 9 silicon modules, have at least 7 silicon hits and are required to be isolated from other tracks within a cone of $\Delta R = 0.3$[6]. The size of the samples can vary from a complete run when we are aligning in the run-by-run basis, up to entire periods of data taking.

The second one is a sample enriched in $Z \rightarrow \mu\mu$ events used as input to compute biases in the momentum and in the impact parameters. Muon candidates are required to be *combined muons*[7]. In addition all muon tracks are required to have:

- Impact parameters with respect to the primary vertex with values $d_0 <$ 0.2 mm and $z_0 < 1.0$ mm.
- At least one hit in the first layer of the Pixel detector, if one is expected.
- At least one Pixel hit and five SCT hits.

[6]The isolation cone, ΔR is defined as $\Delta R = \sqrt{\Delta\phi^2 + \Delta\eta^2}$.

[7]Track reconstruction is performed independently in the ID and MS, if both tracks can be combined then the muon candidate is of type *combined muon*.

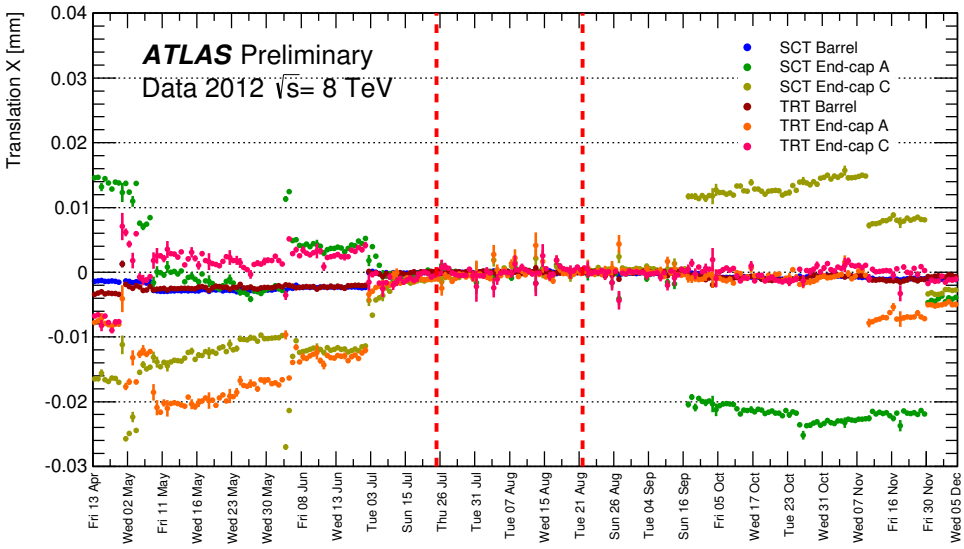

Figure 3.4: The corrections to the global X position (T_X) of all ID sub-detectors with respect to the Pixel detector during 2012. The vertical dashed lines indicate the data taking periods in which the baseline constants were determined. Errors shown are statistical uncertainties on determined alignment parameter and crucially depend on the statistics of data recorded in a given run.

- At most two Pixel or SCT holes[8].
- If $0.1 < |\eta| < 1.9$: at least six TRT hits, including TRT outliers[9], with the fraction of outlier hits being less than 0.9.
- if $|\eta| \leq 0.1$ or $|\eta| \geq 1.9$: if the track has at least six TRT hits, including TRT outliers, the fraction of TRT outliers has to be less than 0.9.

3.3.1 Baseline Alignment Constants

The set of alignment constants used as the basis for all subsequent alignment refinements was obtained using a large amount of data (over 4 fb^{-1}) collected during a period of time where the detector conditions were stable, specifically 30 runs recorded from July 22nd to August 24th 2012. This stability allowed for an accurate determination of alignment constants and a minimization of track parameter biases such as the momentum and the impact parameters. The biases caused by the weak modes described in section 3.2.2 were measured in (η, ϕ) maps, one map per parameter to be corrected. Latter, these maps were used as input for the alignment algorithm in order

[8] A hole is defined as a missing hit in a detector sensor where a signal is expected.

[9] An outlier is defined as a hit discrepant from the trajectory hypothesis by more than a certain number of standard deviations.

to constraint the biases, as it is explained in section 3.3.3. With the new set of alignment constants, the biases were measured again and they were fed back into the alignment algorithm for the next iteration. This procedure was repeated at all levels of granularity until the biases were almost removed, as it is shown in figures 3.5-3.8. All levels of alignment shown in Table 3.1 were performed within this stable period. Two iterations at Level 1 and three iterations at Level 2 were typically required for the *Global* χ^2 method to reach convergence in the entire ID. At Level 3, the *Global* χ^2 was still applied to the Pixel and SCT, requiring in this case 5 iterations to reach convergence, while for the Level 3 aligment of the TRT, the *Local* χ^2 method was used due to the large number of DoF involved. In this case more than 30 iterations were required to take into account correlations among straws.

3.3.2 Run-by-run alignment

The run-by-run alignment allows the identification of detector misalignments prior to the bulk data reconstruction. The ID alignment process was fully integrated in the 48 hours calibration loop at Tier-0 in early 2011. After each run finished, two iterations of Level 1 alignment were performed. Later, the results of this initial alignment were analysed. If movements were observed then the detector geometry needed to be updated before 48 hours.

The monitoring of the evolution over time of the alignment constants was done manually. Therefore this important task could not be translated to an operational mode and be assigned to the ID offline shifter. For that purpose, a web application[10] was developed using the web framework *CherryPy* [86] and PyROOT. This tool was checking automatically for new runs aligned in order to provide plots on demand to the person on an alignment shift. The shifter could produce plots with residuals distributions or figures with the evolution of the alignment constants like in Figure 3.4, where the user was able to easily determine if there is any misalignment. The web application was fully deployed using the ATLAS Web Redirector Service [87] at the end of 2011, being a useful tool to keep the misalignments under control in the 2012 campaign. This web tool is currently operative in the Run 2 data taking.

The results of the Level 1 corrections in the global X translations during 2012 are displayed in Figure 3.4. Due to the Level 1 setup described in section 3.2.3, the alignment corrections are defined relatively to the Pixel detector[11].

[10]The web application is currently hosted at https://atlasalignment.cern.ch/

[11]The Pixel detector was fixed for this setup, therefore any misalignment at Level 1 on

The reference alignment period used to determine the baseline constants is marked by the two vertical lines. Changes to the environmental conditions of the detector such as temperature, magnetic field strength, etc., taking place during technical stops in data taking, often led to significant movements of the detector, as can be seen in Figure 3.4 around 16th of September. In addition to these relatively large movements, slow gradual drifts of the sub-detectors are observed, for instance in the period between 11th of May to 30th of May. These gradual movements are attributed to mechanical relaxations after a sudden change on the operation conditions and it could take many weeks to stabilize.

3.3.3 Sagitta biases

Orthogonal displacements of the reconstructed hits in the detector result in a charge-antisymmetric alteration of the track curvature, which is translated into a shift in the transverse momentum (p_T) according to:

$$\frac{q}{p_T} \rightarrow \frac{q}{p_T} + \delta_{sagitta} \quad \text{or} \quad p_T \rightarrow p_T(1 + q p_T \delta_{sagitta})^{-1} \ , \tag{3.9}$$

where $\delta_{sagitta}$ is an universal bias parameter for all measured momenta and uniquely defines the deformation, while q is the value of the charge associated to the track. As the reconstructed polar angle does not change, the longitudinal component of the momentum scales in an identical manner to the transverse component, leading to:

$$p \rightarrow p(1 + q p_T \delta_{sagitta})^{-1} \ . \tag{3.10}$$

Two methods can be used for the determination of the sagitta biases. The first one, called the E/p method, uses the electromagnetic calorimeter as a reference and utilises the ratio of the measured energy deposited in the calorimeter (E) and of the momentum measured by the ID (p) of the electrons. Under the assumption that the calorimeter response is independent of the charge of the incoming particle, charge-dependent momentum biases introduced by the alignment procedure in the ID are expected to be seen as differences in the E/p ratio for electrons and positrons [88]. The E/p method was used as a cross check during 2012 campaign. The second method, called the $Z \rightarrow \mu\mu$ method, was the main method used to remove the sagitta bias. It extracts

the Pixel detector is absorbed by the Level 1 corrections of the SCT and TRT.

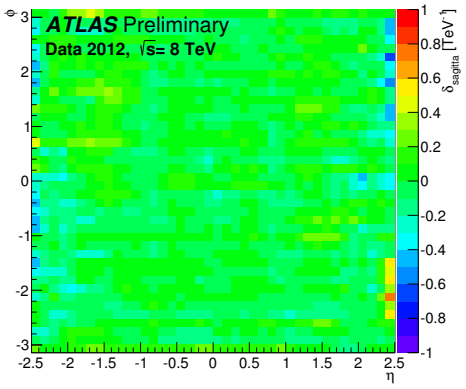

(a) Momentum bias map using $Z \to \mu\mu$ method

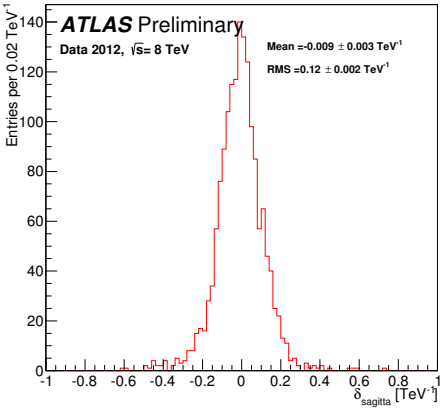

(b) 1D projection from 3.5(a)

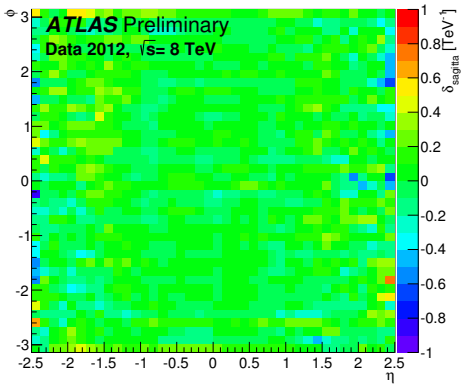

(c) Momentum bias map using E/p method

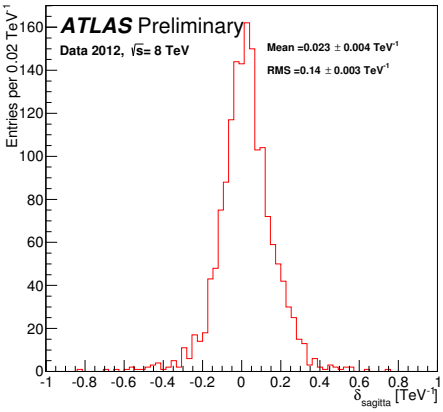

(d) 1D projection from 3.5(c)

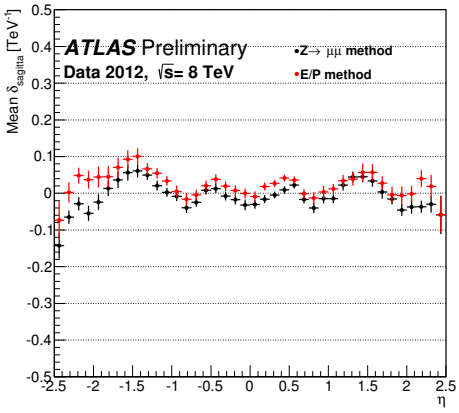

(e) Mean Bias vs. η

Figure 3.5: The 2D plots show the measured momentum bias (δ_{sagitta}) in 2012 data using a 40×40 grid of ϕ and η. The $Z \to \mu\mu$ method is used in Figure 3.5(a) while the E/p method is used in Figure 3.5(c). The histograms on the right show the results of the 1600 measurements of their respective 2D map. The bottom plot shows a comparison of the measured momentum bias (δ_{sagitta}) using the $Z \to \mu\mu$ and E/p method. The data used in these plots were recorded from July 22nd to August 24th 2012.

the bias from shifts on the invariant mass of the Z boson using $Z \to \mu^+\mu^-$ candidates.

The invariant mass of two low mass and highly relativistic particles[12] is given by :

$$m^2 = 2|\boldsymbol{p}_1||\boldsymbol{p}_2|(1 - \cos\theta) \ , \tag{3.11}$$

where $\boldsymbol{p}_1$ and $\boldsymbol{p}_2$ are the momenta of the particles and θ is the angle between the momentum vectors. Then, using Equation 3.10 and ignoring the uncertainties on the angular variables, which are negligible compared to the size of the momentum uncertainties at the Z mass scale, we obtain:

$$m^2 \to m^2_{reco} \approx m^2(1 + q_1 p_{T1}\delta_{sagitta1} + q_2 p_{T2}\delta_{sagitta2}) \ , \tag{3.12}$$

where we keep corrections up to first order in $\delta_{sagitta}$. Later, the shift in the Z invariant mass can be written as:

$$\Delta(m^2) = \frac{m^2_{reco} - m^2_Z}{m^2_Z} \approx q_1 p_{T1}\delta_{sagitta1} + q_2 p_{T2}\delta_{sagitta2} \ , \tag{3.13}$$

where we can see that second order corrections to the invariant mass are leading order in $\delta_{sagitta}$. There is no a priori reason to assign the momentum bias to one of the muons, therefore the sagitta bias measured by each muon is:

$$\delta_{sagitta} = \frac{1}{2}\frac{\Delta(m^2)}{q p_T} \ . \tag{3.14}$$

Since we are using the invariant mass of the Z boson, which is a neutral resonance, it is satisfied that $q_1 = -q_2$ and $p_{T1} \approx p_{T2}$. Then the terms in Equation 3.12 cancel and the invariant mass is not biased on average. Therefore, this method is not as sensitive to global momentum bias as it is the E/p method. However, the $Z \to \mu\mu$ method is good to determine the biases locally ($\delta_{sagitta} \to \delta_{sagitta}(\eta, \phi)$). In this case, the terms in Equation 3.12 do not cancel because each particle is pointing to different regions of the detector, which have different values of $\delta_{sagitta}$.

The sagitta biases are measured in a (η, ϕ) map covering completely the ID, and they are minimized during the determination of the alignment constants by adding constraints to the input track momentum. This is achieved by adding a term to the χ^2 function in Equation 3.2 which constraints the track

[12]The squared four-momentum of a particle is $P^\mu P_\mu = m^2 = E^2 - \boldsymbol{p}^2$. In the case of a highly relativistic and low mass particle ($m \ll E$) we obtain the approximation $E \simeq |\boldsymbol{p}|$.

momentum to its corrected momentum:

$$\frac{q}{p_{corrected}} = \frac{q}{p_{reco}}(1 - qp_T\delta_{sagitta}(\eta, \phi)) \ . \tag{3.15}$$

After each iteration of the alignment algorithm, a new map with the remaining biases is computed and then used as input for the next iteration of the alignment algorithm in order to obtain a set of alignment constants free of biases.

Figure 3.5(a) shows the remaining sagitta biases in 40×40 bins in ϕ vs η after correcting the ID from momentum biases using the $Z \to \mu\mu$ method. In both end-caps there are small localized momentum biases. In the positive end-cap there is a deformation which amounts to approximately -0.6 TeV^{-1} or 3% at $p_T = 50$ GeV. Similar features are observed in the negative end-cap. Figure 3.5(b) shows the distribution of observed sagitta biases. The mean sagitta bias is -0.009 TeV^{-1}, which translates into a mean bias of 0.05%.

As in the previous case, Figure 3.5(c) shows the remaining sagitta biases measured using the E/p method after correcting the ID from momentum biases using the $Z \to \mu\mu$ method. Qualitatively the results look similar to those of the $Z \to \mu\mu$ method. Overall, the mean sagitta bias is 0.023 TeV^{-1}, which translates into a mean bias of 0.12% at $p_T = 50$ GeV. The mean bias observed is significantly different from that of the $Z \to \mu\mu$ method. This can be attributed to the reduced sensitivity of the $Z \to \mu\mu$ method to global sagitta biases, as argued previously. A comparison of both methods used to determine the sagitta bias as a function of η is shown in Figure 3.5(e). The mean sagitta shows clear indications of an η-dependent structure and in both cases the results are compatible.

3.3.4 Impact of Run-by-Run alignment on sagitta biases

Thanks to the monitoring described in Section 3.3.2, significant detector movements were automatically corrected for in the alignment and used for the initial data processing. As a result of this improved procedure the observed time-dependent sagitta biases for 2012 were significantly reduced. The main improvement originates from the correction of the movements of the end-caps with respect to the barrel detector. Figure 3.6 shows the impact of the alignment correction for two representative periods of ATLAS data-taking, referred to as periods A (April 4^{th}–16^{th} 2012) and H (October 13^{th}–26^{th} 2012).

Despite the minimal change in the average sagitta bias both inclusively and

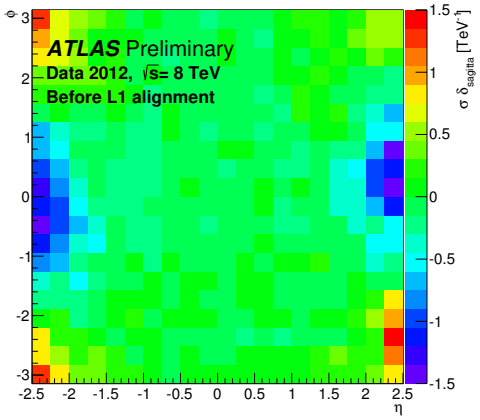

(a) Period A before end-cap alignment

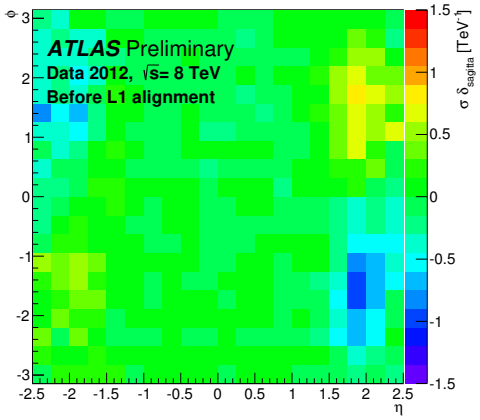

(b) Period H before end-cap alignment

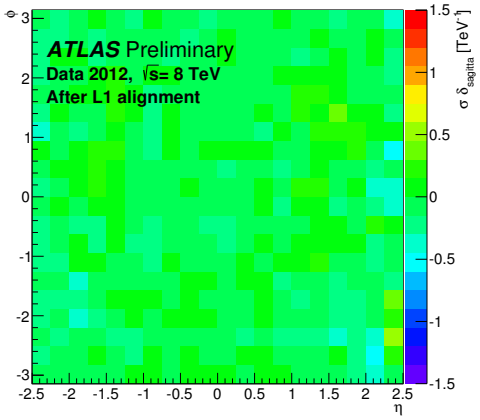

(c) Period A after end-cap alignment

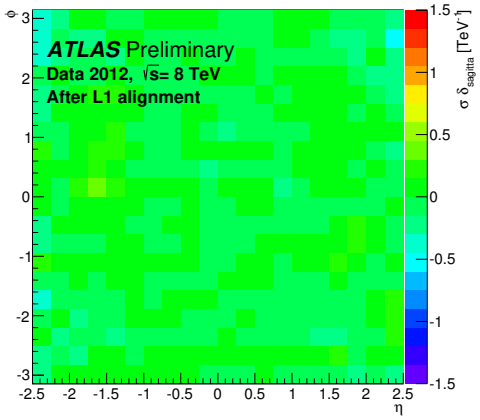

(d) Period H after end-cap alignment

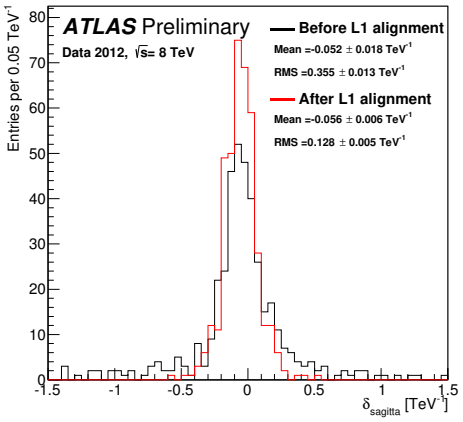

(e) Projection of the measured bias in period A

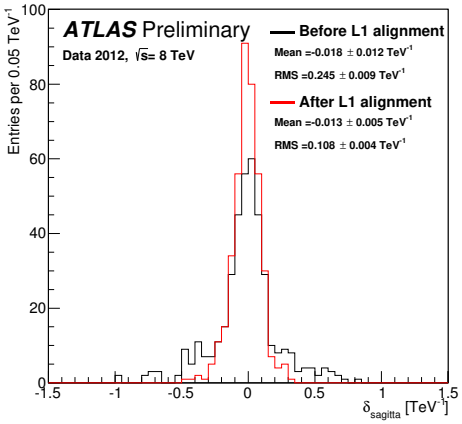

(f) Projection of the measured bias in period H

Figure 3.6: The measured momentum bias (δ_{sagitta}) using the $Z \to \mu\mu$ method in 2012 data for various periods of time. The measurement was performed in 20×20 regions of η and ϕ. It should be noted that a non-negligible statistical fluctuations may be present in these measurements (up to 0.1 TeV^{-1} for the high η regions)

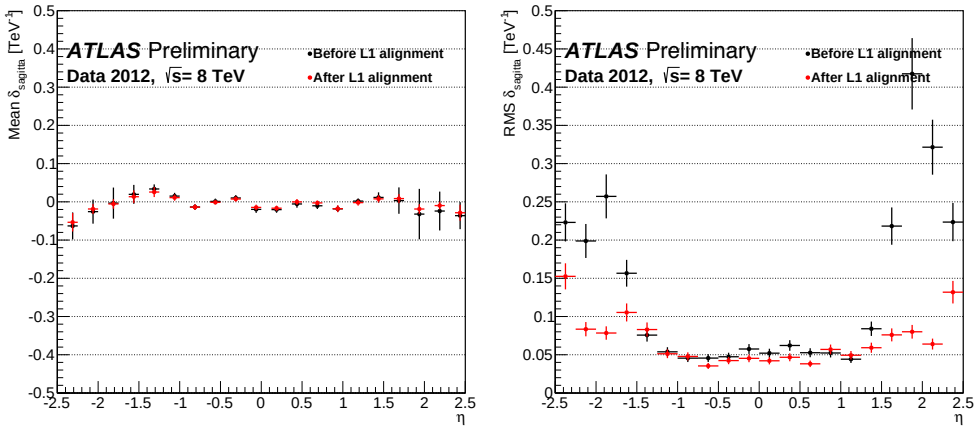

(a) Mean Bias vs. η **(b)** RMS Bias vs. η

Figure 3.7: A comparison of the measured momentum bias (δ_{sagitta}) using the $Z \to \mu\mu$ Period H before and after Level 1 alignment corrections.

as a function of η (see Figure 3.7) before or after corrections, a measurable improvement in the momentum resolution is observed due to the reduction of the ϕ-dependent structure, (see y-axes in Figures 3.6(a) and 3.6(b)). In both periods A and H the spread of the sagitta biases has reduced by over 50% as a result of the alignment corrections.

These results validate the adopted strategy, where a detailed alignment at all levels of granularity with explicit removal of sagitta distortions is performed only in the chosen reference data-taking period (see section 3.3.1). This alignment is then propagated to other periods via Level 1 corrections only, which account for the bulk of physical detector movements due to environmental changes. It has also been verified that higher level alignment corrections can give only marginal improvement on top of the adopted procedure.

3.3.5 Impact parameter biases

In order to remove biases in the longitudinal and transversal impact parameters (IP), a new method was implemented for the first time into the alignment procedure in 2012. In an analogous way to the one used for the determination of the sagitta biases, the IP biases are both measured in (η, ϕ) maps covering completely the ID. An additional term to the χ^2 function in Equation 3.2 is

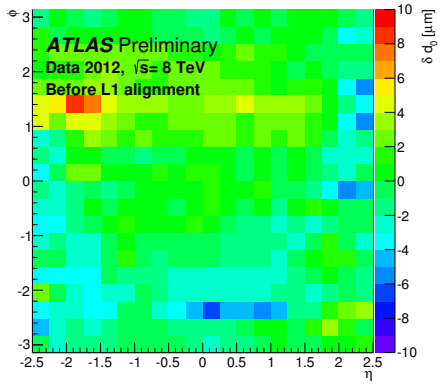

(a) δd_0 bias before alignment

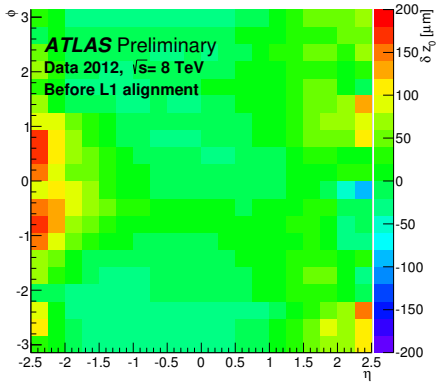

(b) δz_0 bias before alignment

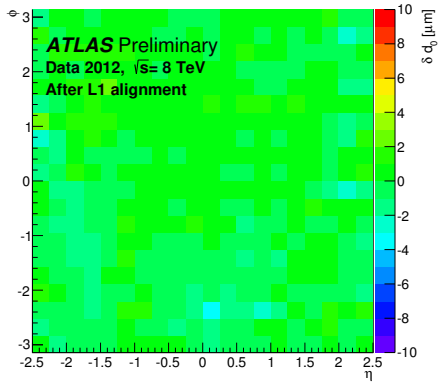

(c) δd_0 bias after alignment

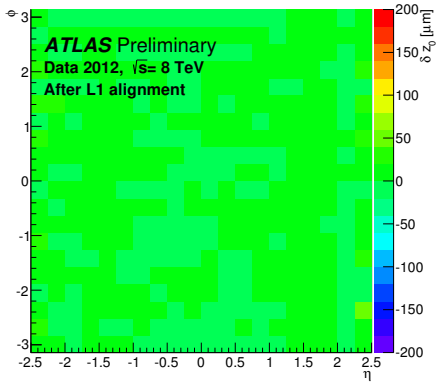

(d) δz_0 bias after alignment

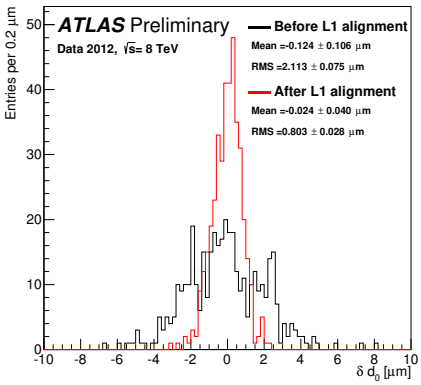

(e) Transversal impact parameter

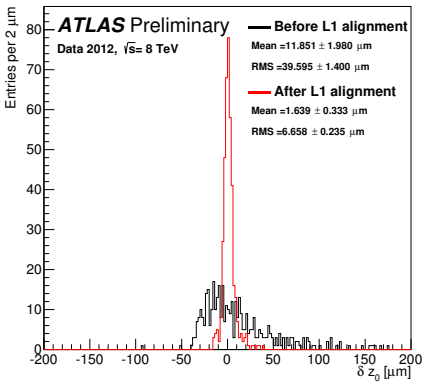

(f) Longitudinal impact parameter

Figure 3.8: Average transverse and longitudinal impact parameter bias in 20×20 bins in η and ϕ. Before the impact parameter constrained alignment (a) and (b) and after the alignment (c) and (d). Histograms of the above maps are reported in plots (e) and (f), with distributions before and after the impact parameter constrained alignment overlaid. The data used in these plots were recorded from July 22nd to August 24th 2012.

added which constraints the impact parameters to their corrected values:

$$\begin{aligned} z_0^{corrected} &= z_0^{measured} - \delta z_0(\eta, \phi), \\ d_0^{corrected} &= d_0^{measured} - \delta d_0(\eta, \phi) \end{aligned} \tag{3.16}$$

After each iteration of the alignment algorithm, a new set of maps with the remaining biases are computed and used as input for the next iteration of the alignment algorithm. This process is repeated until the difference between the impact parameters of the two muons originating from a Z boson is, on average, zero.

The biases prior to corrections for both d_0 and z_0 parameters are shown in figures 3.8(a) and 3.8(b) as a function of η and ϕ. The bias observed in z_0 is most pronounced in the end-caps reaching about 150 μm in the negative η end-cap, while the initial bias in d_0 has a maximum of 8 μm.

The results after the corrections are shown in figures 3.8(c) and 3.8(d). The mean bias is reduced by about 80% in d_0 and by 85% in z_0, and the RMS of the bias distribution is reduced approximately by 60% in d_0 and by 80% in z_0. This large improvement in the impact parameter biases is also shown in Figures 3.8(e) and 3.8(f).

CHAPTER 4

Samples and object selection

After the data delivered by the LHC is collected and filtered by the trigger system of the ATLAS experiment (see Section 2.2.4), the raw data recorded by the detector is a collection of hits in the Inner Detector, energy deposits in both Electromagnetic and Hadronic Calorimeters and hits in the Muon Spectrometer. Several reconstruction algorithms transform the raw data into meaningful physics objects like electrons, muons, jets, etc. (see Section 2.2.6), in order to reconstruct the event signature within the detector volume. Not all the events recorded by ATLAS are of interest for the analysis described in Chapter 5. Therefore, data events are filtered using a series of baseline cuts in order to select events that match the expected signal topology. The events that satisfy these baseline cuts, called preselection cuts, define the preselection region. We call *region* to a subset of events that satisfy a set of requirements. In this analysis we define four different regions which are orthogonal to each other. The signal region is composed of events that satisfy harder cuts to further isolate the t-channel signal events from background events, and is the one used to perform the measurements described in Chapter 5. The other two regions are called *control regions* and they are used for validation and estimation of the backgrounds in the signal region.

This chapter summarizes the datasets and the samples of simulated events used for the analysis in Section 4.1 as well as the definition of the physics objects used described in Section 4.2. The selection criteria of the event selection and control regions used further in the analysis are described in Section 4.3.

4.1 Data and MC samples used in the analysis

The analysis presented in Chapter 5 uses proton-proton collisions delivered by the LHC in 2012 at $\sqrt{s} = 8$ TeV and collected by the ATLAS detector. The data are separated into data periods where the trigger conditions and the LHC operation mode remained stable with the highest data-quality requirements. Each period consists of several runs, which in turn are composed by segments of data known as luminosity blocks. The amount of data used corresponds to an integrated luminosity of 20.2 fb^{-1} with an uncertainty on the integrated luminosity of $\pm 1.9\%$ [89]. The events are required to pass either a single-electron trigger or a single muon trigger [90, 91]. The isolated lepton trigger with a p_T threshold set at 24 GeV was used together with a trigger for non-isolated leptons with a threshold of 60 GeV. The p_T threshold for single isolated muons was 24 GeV while the threshold for non-isolated ones was set to 36 GeV.

In order to study the detector response for different physics processes, to optimize the selection criteria and to have a good understanding of the different background sources, simulated samples based on the Monte Carlo technique (MC) are produced. The MC production process consists of three steps [92]: generation, detector simulation and digitization. In the generation, an event generator is used in order to produce a complete event from the matrix element of the nucleon-nucleon initial state up to the immediate decays and hadronization. The detector simulation, that uses as input the output of the generation step, simulates the interaction and propagation of the particles through the detector. The simulation of the ATLAS detector is done using GEANT4 [93]. Finally, the digitization consists in converting the output of the detector simulation into Raw Data Objects (RDO). At this stage, the output can be run through the same ATLAS trigger and reconstruction algorithms as it is done for the real data.

To generate the t-channel signal events three different generators have been used. The next to leading order (NLO) generator POWHEG-BOX [94] together with the CT10f4 [95] parton distribution functions (PDFs) are used to determine the expected event yields and template distributions. The renormalisation and factorisation scales were set to $\mu_R^2 = \mu_F^2 = 16(m_b^2 + p_{T,b}^2)$, where m_b is the mass of the b-quark and $p_{T,b}$ is the transverse momentum of the b-quark from the initial gluon splitting. The leading order (LO) generator ACERMC [96] using CTEQ6L1 [97] as parton distribution functions is used to test the convergence of the unfolding method. The renormalization and factorization scales were set to $\mu_R = \mu_F = m_t$, where m_t is the top quark

mass. In addition, the LO generator PROTOS together with the CTEQ6L1 are used to compute the parton level unfolding corrections and to check the reliability of the unfolding method. The factorisation scale is set to $\mu^2 = -p_W^2$ for the light quark, where p_W is the four-momentum of the exchanged W boson, and to $\mu_F^2 = m_b^2 + p_{T,b}^2$ for the gluon. The PROTOS generator allows the generation of t-channel single top events with anomalous couplings in the Wtb vertex in both the production and the decay vertices. Four PROTOS samples have been generated with $\mathrm{Im}(g_R)$ in the range $[-0.23, 0.23]$. Five with $\mathrm{Re}(g_R) \in [-0.26, 0.18]$ and two with $\mathrm{Re}(V_R)= 0.25, 0.50$. The values chosen for $\mathrm{Im}(g_R)$ were taken from References [98, 99] in order to study the A_{FB}^N asymmetry, which is the most sensitive asymmetry to variations in $\mathrm{Im}(g_R)$. The values chosen for the real parts of g_R and V_R were chosen following the recommendations from References [100] and [101] respectively. These samples are useful to study asymmetries sensitive to these couplings, like A_{FB} and A_{FB}^l respectively.

All top quark backgrounds, top quark pair [102], s-channel and Wt-channel [103] have been produced using the POWHEG-BOX generator with the CT10 PDFs.

The signal samples as well as the top backgrounds samples, have used PYTHIA [104, 105] with the CTEQ6L1 PDFs in order to simulate the parton shower, the hadronisation and the underlying event of the top quark processes. All these processes have been simulated assuming a top quark mass of 172.5 GeV, and the top quark is assumed to decay exclusively through $t \to Wb$. To generate the $t\bar{t}$ sample, the model parameter h_{damp}, which effectively regulates the high p_T gluon radiation, was set to the top quark mass m_t [106]. The POWHEG-BOX samples are passed through the fully GEANT4 based simulation of the ATLAS detector, while the PROTOS samples are processed through the faster ATLFAST-II simulation [107], which makes use of a parametrised response of the electromagnetic and hadronic calorimeters instead.

The W+jets, Z+jets and diboson (WW, WZ and ZZ) background samples have been simulated using the LO SHERPA generator [108] with its own parameter tune and the CT10 PDFs. SHERPA is used not only to generate the hard process, but also for the parton shower and the modelling of the underlying event. Diboson samples of WW, WZ and ZZ events are also produced using the LO SHERPA generator and the CT10 PDFs. All the generated SHERPA samples are passed through the ATLASFAST-II simulation of the detector.

Finally, the contribution from the QCD multijet background is determined using the data-driven matrix method [109]. In this approach, a set of equations is solved, which relates the observed sample composition in terms of selected leptons of two different categories, loose and tight (see Section 4.2), to its true composition in terms of fake and real leptons. The tight category corresponds to the signal selection while the isolation requirements are removed to define the loose category, which also has a loosened identification quality in the electron case. The number of events passing the tight selection requirements is expressed as:

$$N_{fake}^{tight} = \frac{\epsilon_{fake}}{\epsilon_{real} - \epsilon_{fake}}(\epsilon_{real} N^{loose} - N^{tight}), \tag{4.1}$$

where N^{loose} and N^{tight} are the number of events containing a loose lepton and a tight lepton, respectively. The parameters ϵ_{fake} and ϵ_{real} are respectively the efficiencies of real and fake loose leptons being selected as tight leptons. These efficiencies are determined using dedicated real data samples enriched in real and fake leptons and containing at least two jets [110]. In the electron channel, the fake efficiency is parametrized according to the electron pseudorapidity, the transverse momentum of the leading jet, and the ratio of the leading jet p_T to ΔR_{min}[1]. For the muon channel, the fake efficiency is derived as a function of the muon pseudorapidity and transverse momentum, the distance ΔR_{min}, and the significance of the d_0 parameter. The real and fake efficiencies are in addition extracted as a function of the number of jets and as a function of the number of b-tagged jets, respectively.

4.2 Object reconstruction

After the reconstruction algorithms have provided the different physics objects, a selection criteria is applied to further select the physics objects suitable for the different top quark physics analyses. The definition of the physics objects, which follows the official recommendations for 2012 data analyses [111], are briefly discussed below.

[1]The angular separation between points is defined by: $\Delta R = \sqrt{(\eta' - \eta)^2 + (\phi' - \phi)^2}$. In this case, ΔR_{min} is referred as the minimum angular separation between the lepton and the leading jet.

Electrons

Electron candidates are reconstructed from isolated energy deposits in the electromagnetic calorimeter which are associated to Inner Detector tracks fulfilling strict quality requirements [112]. The electron candidates must have a transverse momentum of $p_T > 25$ GeV and $|\eta| < 2.47$, excluding the barrel-end-cap transition region corresponding to $1.37 < |\eta| < 1.52$. High quality electron candidates are selected using a set of cuts which include stringent requirements on the matching between the track and the calorimeter cluster. Furthermore, the electron candidates should have a longitudinal impact parameter z_0 from the primary vertex smaller than 2 mm. Isolation criteria are in addition required in order to reject candidates coming from other sources than prompt W boson decays.

Electron candidates with relaxed identification criteria and with no isolation cuts applied are also used in the data-driven estimate of fake and real electron selection efficiencies (see Section 4.1). This category of electron candidates is also used to reject dileptonic background events. For that purpose the transverse energy threshold is lowered down to 10 GeV. This dileptonic veto will be describe in Section 4.3.

Muons

Muon candidates are reconstructed using combined tracking information from the Inner Detector and the Muon Spectrometer [113]. They are required to have $p_T > 25$ GeV and $|\eta| < 2.47$. Selected muons must additionally satisfy a series of requirements on the number of track hits present in the various tracking sub-detectors. The longitudinal impact parameter z_0 of the muon candidates with respect to the primary vertex is required to be smaller than 2 mm. Isolation criteria are applied in order to reduce contamination from events in which a muon is produced from a semileptonic b-hadron decay. To that purpose, muon candidates are required to pass a threshold on an isolation variable which is defined as the ratio between the transverse momentum sum over all tracks belonging to a cone of variable size around the muon divided by the muon p_T. In addition, an overlap removal between jets and muons is applied: any candidate muon whose momentum direction is within a cone of size $\Delta R = 0.4$ around a jet with $p_T > 25$ GeV and a jet vertex fraction greater than 0.5 is removed. To estimate the fake and real selection efficiencies in the muon channel (see Section 4.1), candidates muons with no isolation cuts

applied are considered. Non-isolated muon candidates with a p_T threshold lowered to 10 GeV are also considered for the dileptonic veto presented in Section 4.3.

Jets

Jets are reconstructed using the anti-k_t algorithm [114] with a radius parameter of 0.4, starting from topological clusters [115] and calibrated with a local cluster weighting method [116]. Jets are calibrated using an energy and η-dependent simulation-based scheme with in situ corrections based on data. The jet energy is further corrected for the effect of multiple proton-proton interactions. To reject jets from pile-up events, a so-called jet-vertex-fraction criterion [117] is applied to the jets with $p_T < 50$ GeV and $|\eta| < 2.4$: at least 50% of the scalar sum of the p_T of the tracks associated with a jet is required to be from tracks compatible with the primary vertex[2]. Jets overlapping with selected electron candidates within a cone of radius $\Delta R = 0.2$ are removed from events, as the jet and the electron are very likely to correspond to the same physics object. If a remaining jet with $p_T > 25$ GeV is found close to an electron within a cone of radius $\Delta R = 0.4$, then the electron is discarded.

In order to distinguish light jets from b-tagged jets, a neural network discriminant is used, which combines three different algorithms exploiting the properties of a b-hadron decay in a jet [118]. The b-tagging algorithm is optimised to improve the rejection of c-quark jets, since W boson production in association with c-quarks is a major background in this analysis. The requirement applied to the neural network discriminant corresponds to a b-tagging efficiency of 50%, and mistagging rates of 3.9% and 0.07% for c-quark jets and light jets respectively, as predicted in simulated $t\bar{t}$ events.

Finally, jets considered in this analysis should have a transverse momentum $p_T > 30$ GeV and a pseudorapidity $|\eta| < 4.5$. To remove some mis-modelling in the transition region between the central and forward hadronic calorimeters, the p_T threshold is raised to 35 GeV for the jets having a pseudo rapidity $2.7 < |\eta| < 3.5$. The b-tagged jets have the same transverse momentum requirement, however, the detector can only identify b-jets in the central pseudorapidity region, $|\eta| < 2.5$.

[2] A primary vertex candidate is defined as a reconstructed vertex with at least five associated tracks with $p_T > 400$ MeV. The primary vertex associated with the hard scattering collision is the candidate with the largest sum of the squared p_T of the associated tracks.

Missing transverse momentum

The missing transverse momentum, with a magnitude E_T^{miss}, is defined as the momentum imbalance in the transverse plane where momentum conservation is expected. It is a measure of the presence of undetectable particles, such as neutrinos, but also includes energy losses due to detector inefficiencies. It is reconstructed from the vector sum of energy deposits in the calorimeter projected onto the transverse plane. Clusters associated with high p_T jets and electrons are further calibrated using their respective energy corrections and contributions of the selected muons are also included in the calculation of the E_T^{miss} [119].

4.3 Event selection

In order to distinguish a single top t-channel event among all the possible processes that happen in a proton-proton collision, we have to define the signature that such an event leaves in the detector. At leading order, a valence quark interacts with a bottom quark from the sea through the exchange of a W boson, which results in the production of a light quark and a top quark (see Figure 1.4(a)). The top quark produced singly decays into a bottom quark and a W boson, which subsequently can decay to a lepton and a neutrino. Therefore, the detector signature of a t-channel event in the leptonic channel consists of events with only one lepton, two jets, one of them being identified as a b-jet, and missing transverse energy as it is shown in Figure 4.1. However, there are other processes that may lead to the same signature, such as $t\bar{t}$ and W+jets production, which are the main background contributions to t-channel production. The former is difficult to distinguish from the signal since $t\bar{t}$ events contain real top quarks in the final state. The latter contributes to the background if there is a b-quark in the final state or due to mistagging of jets containing other quark flavours. Multijet production via the strong interaction can contribute as well if, in addition to two reconstructed jets, an extra jet is misidentified as a fake lepton. Other minor backgrounds originate from Wt, s-channel single top-quark, Z+jets and diboson production.

The selection is carried out in two stages, the preselection and the selection. The preselection selects event candidates with the t-channel signature. Once we have a collection of preselected events, we can reconstruct the top quark from the decay products. Later, we can apply the selection requirements in order to enhance the signal content over the background in the signal re-

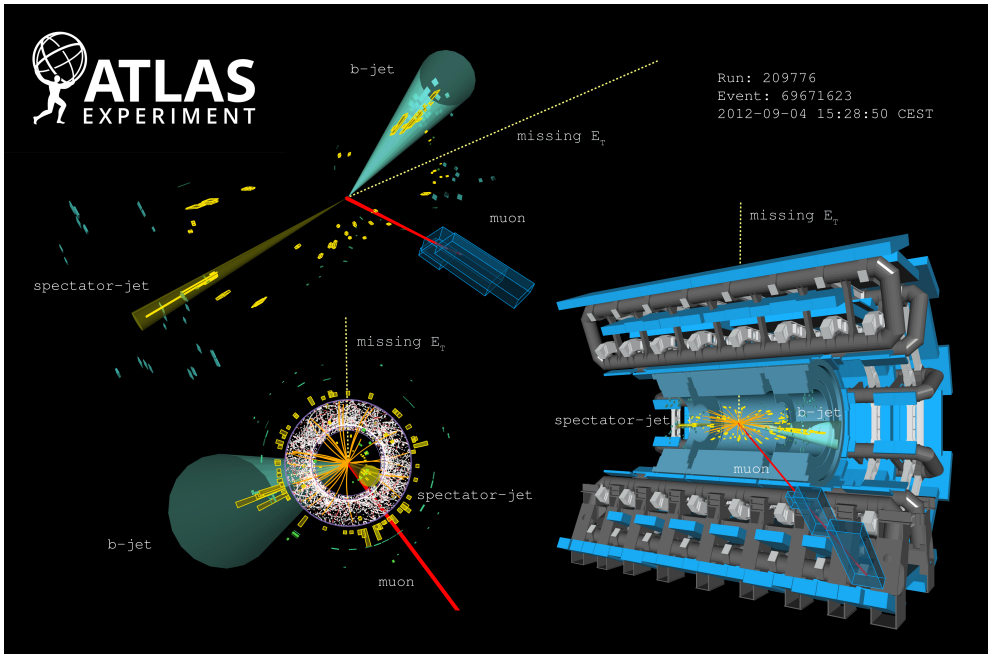

Figure 4.1: Event display of a single top quark t-channel candidate event in the muon channel. The muon is represented by the red line, the spectator quark by a yellow cone, the b-tagged jet with a teal cone and the E_T^{miss} with a dashed yellow line. The p_T of the muon is 40.67 GeV, the E_T^{miss} is 86.06 GeV and the E_T of the spectator quark and of the b-tagged jet are 51.33 GeV and 69.09 GeV respectively [120].

gion. In addition to the signal region, two control regions are defined for this analysis, which are used for validating the MC modelling and for estimating the background in the signal region.

4.3.1 Preselection

The events that form the preselection region are required to contain at least one good primary vertex candidate and no jets failing to satisfy the reconstruction quality criteria. These events should also contain exactly one isolated lepton candidate (electron or muon), exactly two selected jets, one of them being b-tagged and a missing transverse energy $E_T^{miss} > 30$ GeV. The lepton and the two jets of the preselected events should pass the requirements described in Section 4.2. To reduce the contribution from multijet events, two cuts are applied. The first one set a threshold on the transverse mass of the lepton-E_T^{miss} system:

$$m_T(l, E_T^{miss}) = \sqrt{2P_T(l)E_T^{miss}(1 - \cos\Delta\phi(l, E_T^{miss}))} > 50 \text{ GeV}, \qquad (4.2)$$

where $\Delta\phi(l, E_T^{miss})$ is the azimuthal angle between the lepton transverse momentum and the missing transverse energy. The second one applies an isolation cut to low p_T leptons :

$$\frac{p_T(l)}{\left(1 - \frac{\pi - |\Delta\phi(l,\text{jet}_l)|}{\pi - 1}\right)} > 40\text{GeV}, \tag{4.3}$$

where $\Delta\phi(l, \text{jet}_l)$ is the difference between the azimuthal angle of the lepton momentum and the one of the leading jet in p_T. To further reject the contribution from the top quark pair background, a dilepton veto is applied. This veto consists in reject events with an additional lepton, identified with less stringent criteria and with a p_T threshold lowered to 10 GeV.

The preselected events contain the decay products of the leptonic decay of the top quark, thus we can reconstruct the W boson and the top quark at this stage. The method followed to reconstruct the W boson as well as the top quark is explained in the Appendix A.

Table 4.1 shows the event yields for the electron and muon channels after preselection. Plots showing the distributions of the lepton transverse momentum, the missing transverse energy and the transverse W mass for the electron and muon channels are shown in Figure 4.2. In the top panels the data distribution is compared to the predictions for the signal and backgrounds, while the lower panels show the ratio of data to prediction. The uncertainty bands include the statistical uncertainty due to the limited size of the simulation samples and the uncertainty in the normalisation of the multijet background, added in quadrature. The distributions show good overall data-prediction agreement at this stage.

4.3.2 Selection

In order to further reject the background that passes the preselection cuts, four additional requirement are applied defining the signal region:

- The pseudorapidity of the light jet must satisfy $|\eta| > 2.0$, since the spectator quark tends to be produced in the forward direction in the t-channel process.

- The separation in η between the light jet and the b-tagged jet must be larger than 1.5, to reduce the contribution from the top quark pair background events.

Process	Preselection	Selection	$t\bar{t}$ CR	anti-signal CR	W+jets CR
t-channel	19592±39	5985±22	1921±13	13606± 33	10944±30
Wt-channel	5841±65	199±12	2908±46	5642±64	3760±53
s-channel	1217±3	63±1	114±1	1154±3	455±2
$t\bar{t}$	42981±52	1893±11	59586±62	41088±51	23558±40
W+bb	26704±83	804±14	4594±33	25900±82	23789±82
W+cc	16777±157	962±39	1537±47	15816±152	119655±393
W+light jets	2793±135	92±20	240±34	2701±133	115232±696
Z+bb	3518±28	148±6	753±12	3370±28	3333±29
Z+cc	613±40	24±7	125±15	589±39	7633±131
Z+light jets	124±29	0±0	46±1	124±9	6600±544
Diboson	828±7	17±1	198±3	811±7	3877±15
Multijet	9679±6775	417±292	877±614	9262±6483	20677±1447
Total exp.	130668±6780	10604±297	72897±623	120064±6488	339511±14507
Data	134994±367	10527±103	74121±272	124467±353	379527±616
S/B	0.18	1.30	0.03	0.13	0.03

Table 4.1: Predicted and observed event yields in the preselection, selection , $t\bar{t}$ control region (CR), anti-signal CR and W+jets CR. The electron and muon channels are combined. For the simulated processes, the uncertainties correspond to the errors due to the limited size of the MC samples. An uncertainty of ±70% on the data-driven normalization is quoted for the multijet process. No scale factors are applied.

- The mass of the reconstructed top quark is required to be between 130 GeV and 200 GeV, to reject background events from processes not involving the top quarks.

- The scalar sum, H_T, of the p_T of the lepton, the p_T of the jets and E_T^{miss} must be larger than 195 GeV, to further reduce the number of background events, in particular the W+jets background contribution.

Table 4.1 shows the event yields for the electron and muon channels after selection. The signal to background ratio is 1.3, with the t-channel single top quark production representing 56% of the total expectation. The two main background contributions come from W+jets and $t\bar{t}$. Each contribution represents 18% of the total expectation. The other processes that contribute to the background are Z+jets, diboson production and multijet events. Plots showing the distribution of the four variables relevant for the selection requirements are shown in Figure 4.3. The distributions show an overall good agreement between the data and the signal and background predictions.

4.3.3 Control regions

To validate the modelling and estimate the normalization of the top quark background ($t\bar{t}$, Wt and s-channel) and W+jets background contributions,

Process	Scale factor
t-channel	0.95±0.02
$t\bar{t}$, Wt, s-channel	1.01±0.01
W+jets	1.10±0.02

Table 4.2: Scale factors and uncertainties extracted for the signal and background processes from the simultaneous maximum-likelihood fit of the event yields in the signal, anti-signal and $t\bar{t}$ regions. The quoted uncertainties are statistical only.

the simulated events are compared to the data in two dedicated background dominated regions. The $t\bar{t}$ control region is defined by the same cuts that are applied in the preselection, but containing two additional jets that are required to be untagged. The W+jets control region consists in events selected using the preselection cuts but applying a relaxed b-tagging requirement corresponding to an efficiency of 80%. In addition, the dilepton veto is not applied in this control region and all events satisfying the signal b-tagging requirement used to define the signal region are excluded. The last control region used is the so-called anti-signal region. It is defined by events that satisfy the preselection criteria but they fail the final selection. This region is only used in the normalisation fit, in combination with the $t\bar{t}$ control region. The W+jets contribution in this region is of the same order of the $t\bar{t}$ (37% of W+jets contribution and 35% of $t\bar{t}$ contribution). This region is preferred to the W+jets control region to constrain the W+jets normalisation because it has a similar flavour composition to that of the signal region. The predicted fraction of heavy flavour events is around 95% for both, the signal and anti-signal regions, whereas it is 55% in the W+jets control region.

4.3.4 Background normalization

The signal and background normalizations are estimated through a simultaneous maximum-likelihood fit to the numbers of data events observed in the signal, $t\bar{t}$ and anti-signal regions. The likelihood function is given by the product of Poisson probability terms associated with the fitted regions, combined with the product of Gaussian priors to constraint the background rates to their predictions within the associated uncertainties. The likelihood function can be written as:

$$L(\beta^s;\beta_j^b) = \prod_{i=1}^{N_{selections}} \frac{e^{-\mu_i}\cdot\mu_i^{n_i}}{n_i!} \cdot \prod_{j=1}^{N_{backgrounds}} G\left(\beta_j^b;1,\Delta_j\right) \ . \qquad (4.4)$$

where β^s is the scale factor associated to the signal process and β_j^b is the scale factor associated to the background process j. The index i runs over the regions used in the fit, n_i is the observed number of events and μ_i is defined as the sum of the expected contributions from signal and all simulated or data-driven backgrounds. The Δ_j term represents the constrain applied to the normalization of the background process j used in the Gaussian term. The details of the maximum-likelihood fit can be found in Appendix B.

The result of the maximum-likelihood fit is shown in Table 4.2. The normalization of the top background, W+jets and t-channel are corrected using these scale factors to check the modelling of the different distributions, as well as to perform the measurements of the observables in the signal region presented in Chapter 5

Good overal data-prediction is found in the $t\bar{t}$, W+jets and anti-signal control regions. Figure 4.4 shows the distributions in the $t\bar{t}$ control region for the four variables used to define the final selection. The distributions obtained in the anti-signal control region are displayed in Figure 4.5, and the same distributions for the W+jets control region are displayed in Figure 4.6.

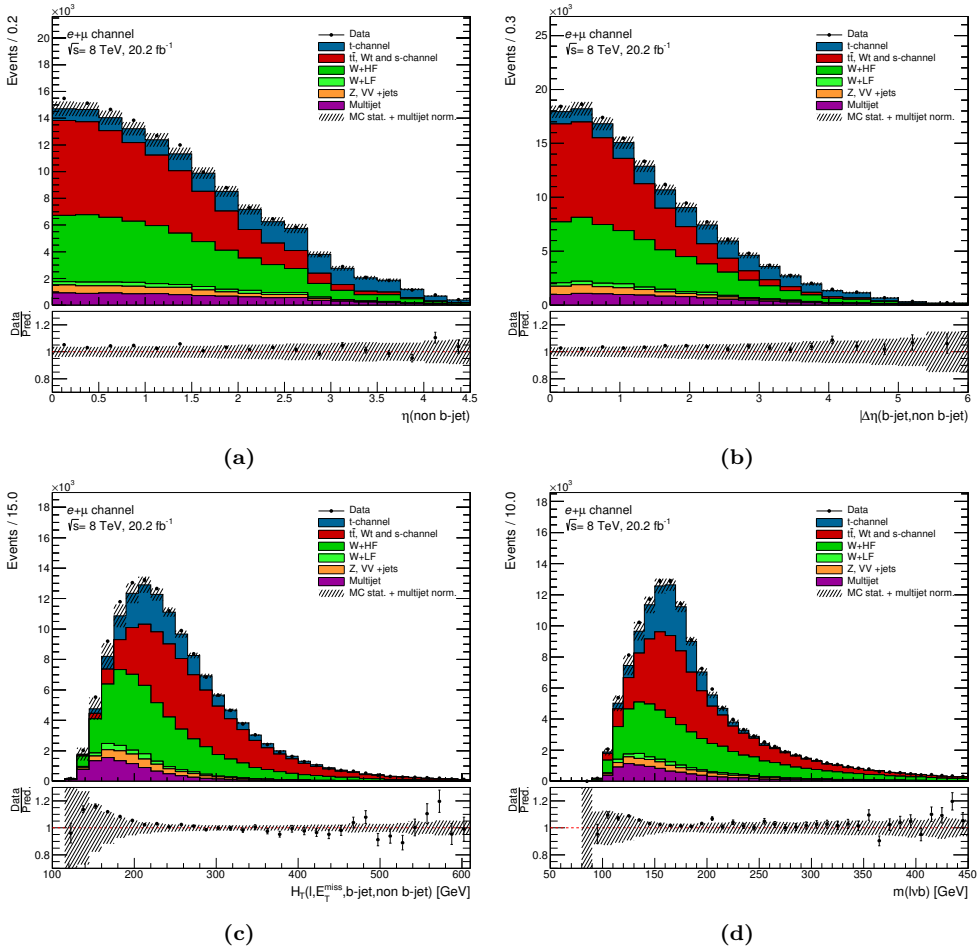

Figure 4.2: Distribution of the selection variables in the preselection region. The electron and muon channel are combined: 4.6(a) η of the light jet, 4.6(b) separation in η between the light jet and the b-tagged jet, 4.6(c) scalar sum of the p_T of the lepton, the p_T of the jets and E_T^{miss}. The observed distributions are compared to the predicted signal and background distributions, normalised to the results of the maximum-likelihood fit (Table 4.2). The lower panels show the ratio of data to prediction. The uncertainty bands include the statistical uncertainty due to the limited size of the simulation samples and the uncertainty in the normalization of the multijet background, added in quadrature.

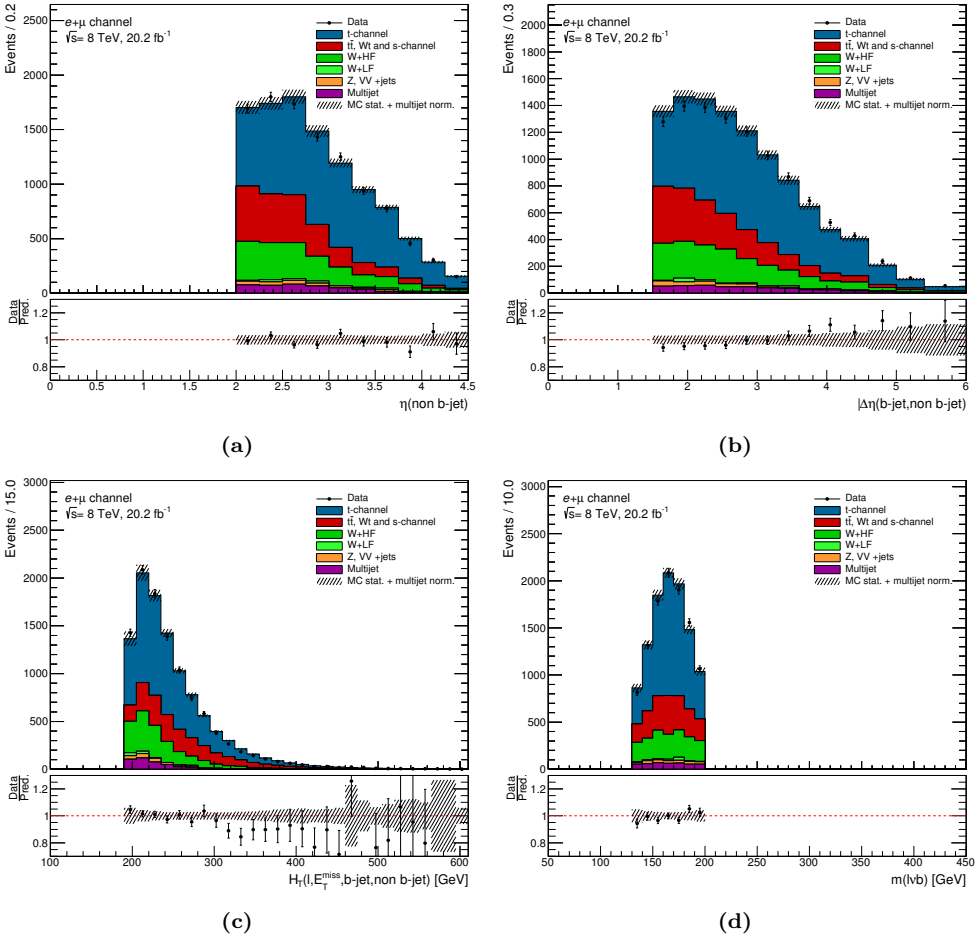

Figure 4.3: Distribution of the selection variables in the signal region. The electron and muon channel are combined: 4.6(a) η of the light jet, 4.6(b) separation in η between the light jet and the b-tagged jet, 4.6(c) scalar sum of the p_T of the lepton, the p_T of the jets and E_T^{miss}. The observed distributions are compared to the predicted signal and background distributions, normalised to the results of the maximum-likelihood fit (Table 4.2). The lower panels show the ratio of data to prediction. The uncertainty bands include the statistical uncertainty due to the limited size of the simulation samples and the uncertainty in the normalization of the multijet background, added in quadrature.

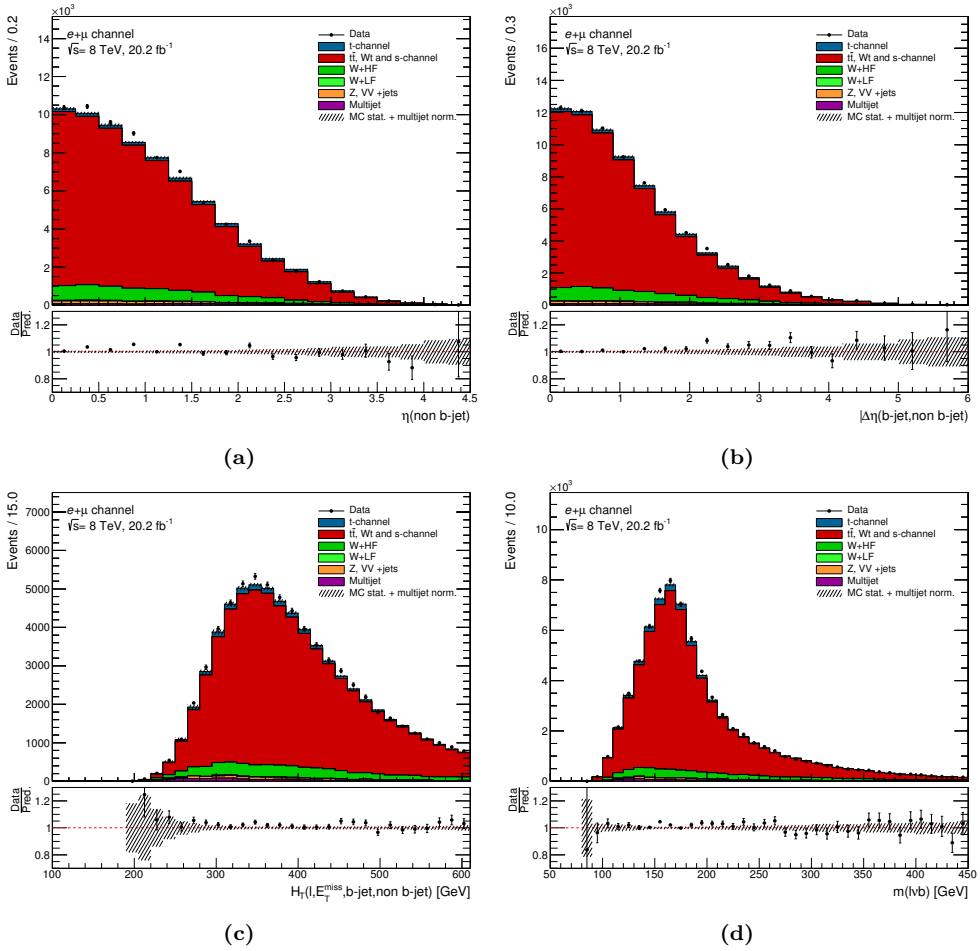

Figure 4.4: Distribution of the selection variables in the $t\bar{t}$ control region. The electron and muon channel are combined: 4.6(a) η of the light jet, 4.6(b) separation in η between the light jet and the b-tagged jet, 4.6(c) scalar sum of the p_T of the lepton, the p_T of the jets and E_T^{miss}. The observed distributions are compared to the predicted signal and background distributions, normalised to the results of the maximum-likelihood fit (Table 4.2). The lower panels show the ratio of data to prediction. The uncertainty bands include the statistical uncertainty due to the limited size of the simulation samples and the uncertainty in the normalization of the multijet background, added in quadrature.

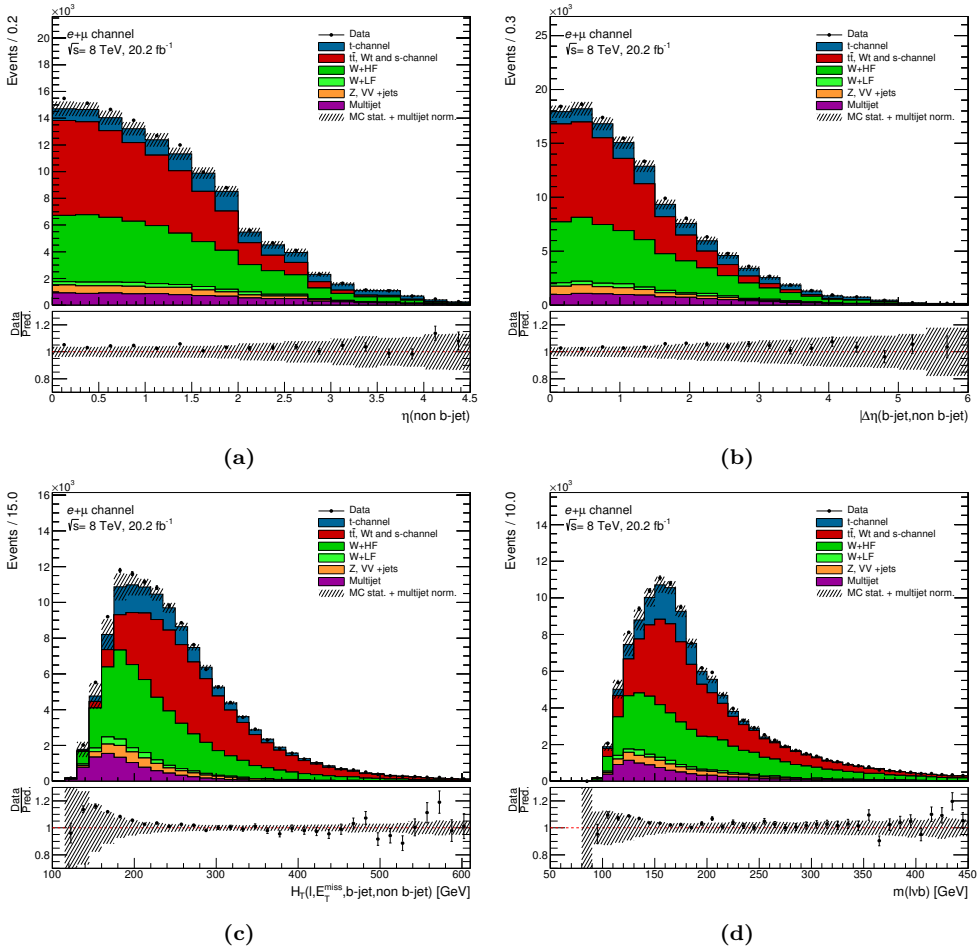

Figure 4.5: Distribution of the selection variables in the anti-signal region. The electron and muon channel are combined: 4.6(a) η of the light jet, 4.6(b) separation in η between the light jet and the b-tagged jet, 4.6(c) scalar sum of the p_T of the lepton, the p_T of the jets and E_T^{miss}. The observed distributions are compared to the predicted signal and background distributions, normalised to the results of the maximum-likelihood fit (Table 4.2). The lower panels show the ratio of data to prediction. The uncertainty bands include the statistical uncertainty due to the limited size of the simulation samples and the uncertainty in the normalization of the multijet background, added in quadrature.

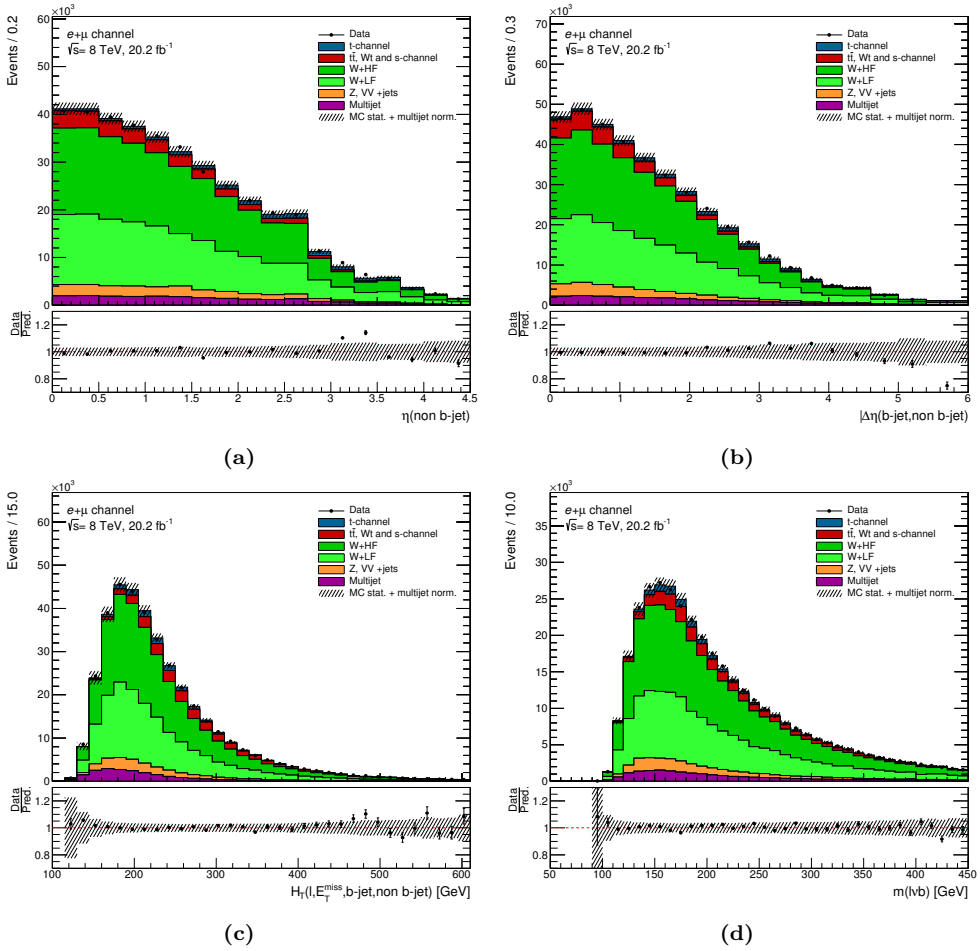

Figure 4.6: Distribution of the selection variables in the W+jets control region. The electron and muon channel are combined: 4.6(a) η of the light jet, 4.6(b) separation in η between the light jet and the b-tagged jet, 4.6(c) scalar sum of the p_T of the lepton, the p_T of the jets and E_T^{miss}. The observed distributions are compared to the predicted signal and background distributions. The W+jets contribution is normalised to match the data event yield. The lower panels show the ratio of data to prediction. The uncertainty bands include the statistical uncertainty due to the limited size of the simulation samples and the uncertainty in the normalization of the multijet background, added in quadrature.

CHAPTER 5

Measurement of polarisation observables

The measurement of the asymmetries related to the polarisation of the top quark and the W boson, together with the helicity fractions of the W boson are presented in this chapter. All measurements are performed in the signal region described in Chapter 4. The background distributions are built using the templates and the normalizations determined in Section 4.3. Then, they are subtracted from the data distributions. After that, the measured angular distributions are corrected for detector effects and selection efficiencies using an iterative Bayes unfolding method. Finally, the uncertainty is estimated by using pseudo-experiments and the compatibility of the measurements with the SM prediction is calculated.

5.1 Unfolding

The measurement of the asymmetries can not be performed directly from the different angular distributions if we pretend to compare our results with those obtained from different experiments or with the theoretical predictions. The recorded events are distorted by detector effects, such as detector resolution and geometric acceptance, and also by the selection criteria of the events, that favour some kinematic distribution against other ones. An example of the impact of the selection criteria is shown in Figure 5.1, where it can be seen that the isolation requirement for leptons prohibits jets to be very close to leptons, removing events from the region $\cos\theta^l \approx 1$. Therefore, the angular

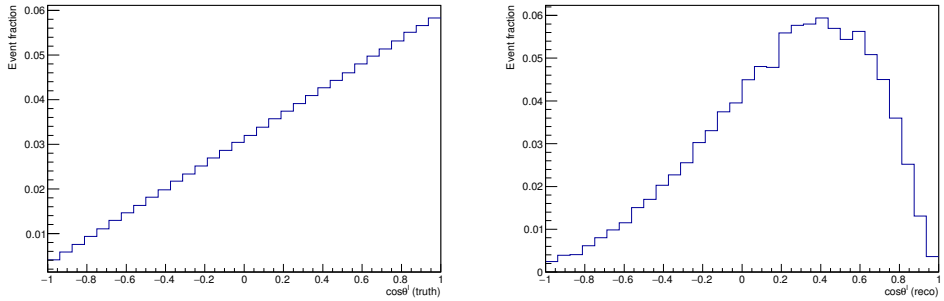

(a) **(b)**

Figure 5.1: Distributions of $\cos\theta^l$ at parton (truth) level, Figure (a), and after object reconstruction and selection, Figure (b).

distributions must be corrected from these effects to fully recover the distributions at parton level, where the asymmetries are extracted. This procedure is called *unfolding* in the field of experimental high energy physics.

5.1.1 Iterative Bayes unfolding

The unfolding algorithm used to perform the measurements for this thesis is implemented in the RooUnfold package [121]. It is based on the Bayes' theorem and was developed by G. D'Agostini [122].

The method is based on describing the problem with an "effect" E and a "cause" C. The reconstructed measured angular distribution corresponds to the effect $n(E_i)$[1]. In this analysis the cause $n(C_j)$[2] is represented by the angular distribution at parton level, before any reconstruction algorithm or selection cut is applied. The effect $n(E_i)$ is known and well measured. However, we are interested in the cause $n(C_j)$ that produces that effect, i.e. the angular distribution at parton level. The cause can not be measured thus it has to be estimated. The probability for an effect to be originated from a cause, $P(E_i|C_j)$, can be estimated assuming the knowledge of the migration matrix and the efficiency which are both determined with Monte Carlo simulation. Using the Bayes theorem, the probability for a cause C_j to be produced from an effect E_i can be written as [121, 122]:

$$P(C_j|E_i) = \frac{P(E_i|C_j) \cdot n_0(C_j)}{\sum_{k=1}^{n_C} P(E_i|C_k) \cdot n_0(C_k)}, \tag{5.1}$$

where the term $n_0(C_j)$ is the prior distribution for the parton level distribution,

[1] i represents the bin number.
[2] j represents the bin number.

initially arbitrary. The term $P(E_i|C_j)$ corresponds to the $n_C \times n_E$ migration matrix since it describes the probability for effect E_i to be originated from cause C_j. Thus, the estimation $\hat{n}(C_j)$ of the cause is given by:

$$\hat{n}(C_j) = \frac{1}{\epsilon_j} \sum_{i=1}^{n_E} P(C_j|E_i) \cdot n(E_i), \tag{5.2}$$

where $n(E_i)$ is the measured angular distribution and ϵ_j is the selection efficiency at bin j. The final result for $\hat{n}(C_j)$ is derived from an iterative procedure starting from the initial distribution $n_0(C_j)$. The number of iterations n_{iter} is the regularization parameter of the unfolding method, and has to be determined for each distribution.

The iterative Bayes unfolding uses as inputs for each angular distribution we want to unfold, the angular distribution at parton level, the efficiency and migration matrix and finally the reconstructed angular distribution to be unfolded.

The angular distribution at parton level, obtained from signal simulation, is used as the initial prior $n_0(C_j)$ in Equation 5.1, which is replaced after each iteration by $\hat{n}(C_j)$ from Equation 5.2. The efficiency is used to restore the number of events expected in each bin at parton level. The migration matrix relates the migration of reconstructed events in bin l into the corresponding parton level event in bin k. This migration of events is due to smearing effects, such as detector resolution, neutrino reconstruction, etc. Finally the reconstructed angular distribution can be obtained from MC simulation in order to validate the unfolding method, or from data after background subtraction. The reconstructed distribution is used as input in Equation 5.2 in order to obtain the estimation of the angular distribution at parton level.

The SM PROTOS sample described in Section 4.1 is used in this analysis in order to obtain the angular distributions at parton level, the migration matrices, and the reconstructed angular distributions. The reconstructed angular distributions from PROTOS are used to validate the unfolding method, while the distributions at parton level as well as the migration matrices are used not only in the validation procedure but also to unfold the data distributions in order to perform the measurement of the asymmetries.

5.1.2 Unfolding validation

The validation of the iterative Bayes unfolding procedure includes first the convergence tests in order to define the optimal number of iteration of

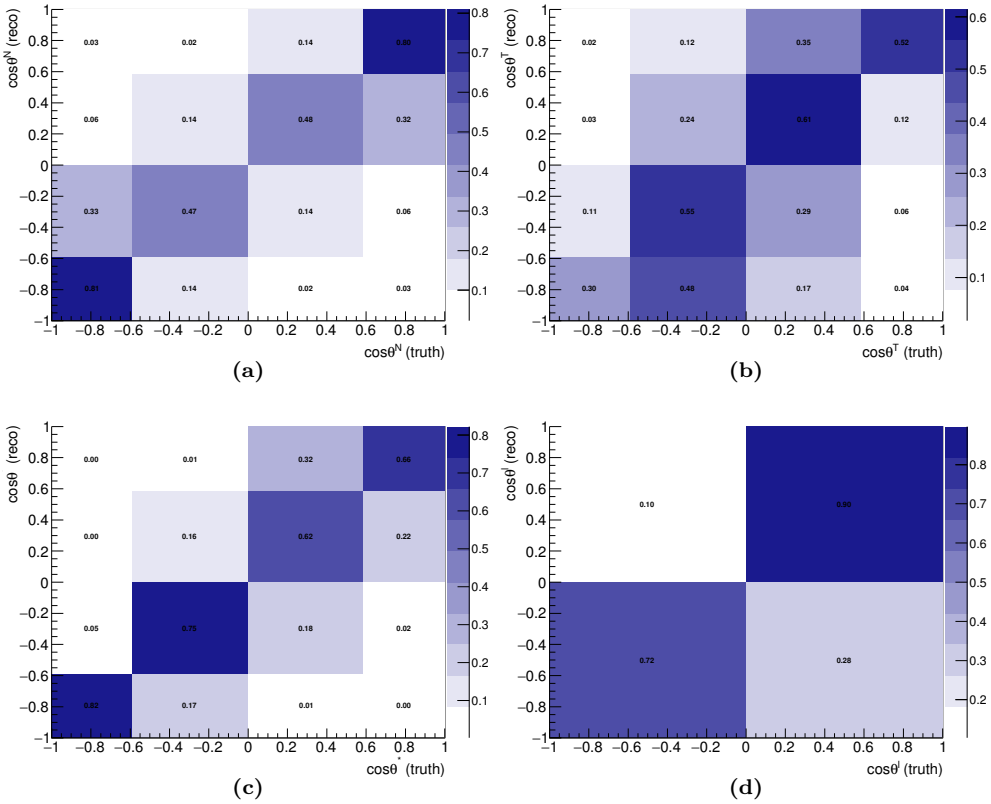

Figure 5.2: Migration matrices for the angles $\cos\theta^N$ (a), $\cos\theta^T$ (b), $\cos\theta^*$ (c) and $\cos\theta^l$ (d). The electron and muon channels are combined. The angle at reconstruction level is shown on the vertical axis, while the angle at parton level, also known as truth level, is shown on the horizontal axis. A minimum of 45% of the events are in the diagonal of the migration matrix, with the exception of the first bin ($\cos\theta^T$ = -1), where a large migration to the next bin is observed.

the algorithm. Subsequently, further tests are performed to check the closure and the linearity of its response. These tests are performed using the various t-channel event samples generated with the POWHEG-BOX, ACERMC and PROTOS generators, all interfaced to PYTHIA for parton showering. The POWHEG-BOX and ACERMC samples are used as signal simulation, while the SM PROTOS sample is used to determine the detector and physics corrections required for the unfolding method. The reason to use a LO generator in order to determine the corrections for the unfolding instead of using a NLO one, is due to the fact that the light quark is unambiguously defined at LO, which is not the case at NLO. The migration and reconstruction effects are similar for both electron and muon channels, therefore both channels are merged. The background processes are not taken into account in the validation step.

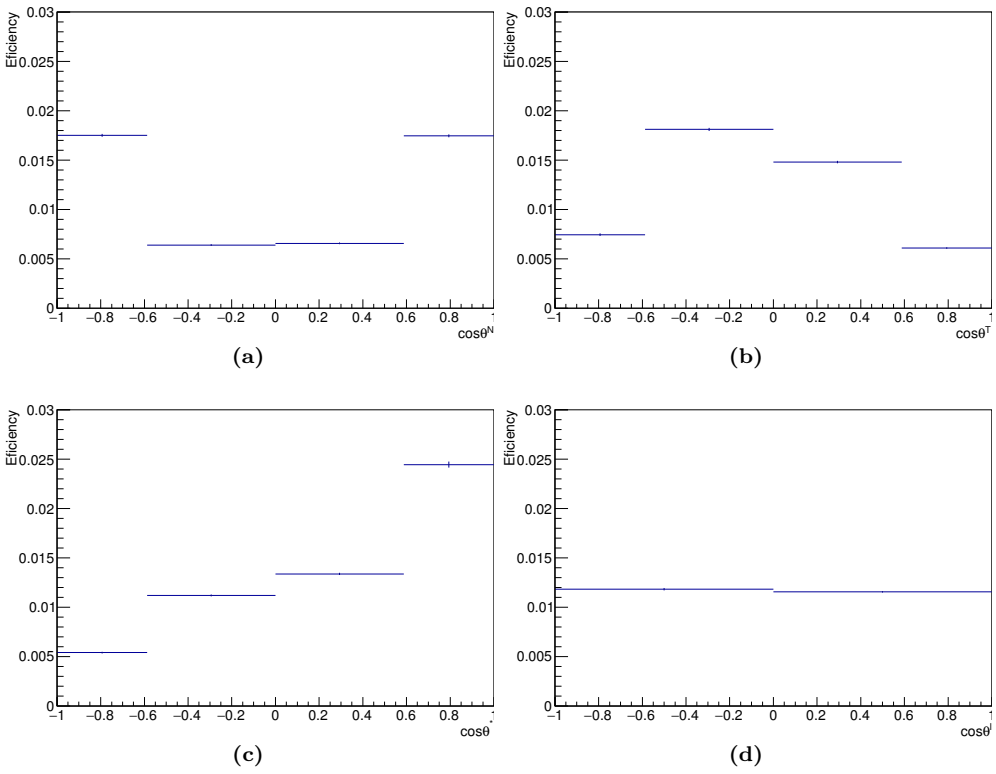

Figure 5.3: Event selection efficiency for $\cos\theta^N$ (a), $\cos\theta^T$ (b), $\cos\theta^*$ (c) and $\cos\theta^l$ (d). The efficiency is defined as the ratio between the number of events measured after selection and the number of events generated at truth level. The electron and muon channels are combined.

Angular binning

The number of bins is chosen taking into account the particularities of the asymmetries that are measured, the population of the diagonal elements of the migration matrix associated with the angular variable, and the statistical and systematic expected precisions.

As it is explained in Chapter 1.3, we can define three values of the cosine of the different angular distributions with respect to which measure the related asymmetry. One value is set at $\cos\theta = 0$, which defines the forward-backward asymmetry, and the other two are $\cos\theta = -(2^{2/3} - 1)$ and $\cos\theta = (2^{2/3} - 1)$, which define the A_+ and A_- asymmetries respectively. These values must lead the binning configuration of the histograms in order to measure the three related to asymmetries for the angles θ^N, θ^T and θ^*. With this requirement, a minimum of 4 bins have to be used, which are in fact of asymmetric width. The second criteria is related with the population of the diagonal elements of the migration matrices. The binning configuration has to ensure a population

of events of at least 45% in the diagonal elements in order to have a stable unfolding response. This requirement excludes configurations with 6 and more bins. For the angular distribution θ^l only two bins of same width are considered since only the forward-backward asymmetry is defined for this angle.

In Figure 5.2 it is shown the migration matrices used in the unfolding for each angular distribution. The requirement of at least 45% of entries in the diagonal is fulfilled for all the angular distributions, except by the first bin in $\cos\theta^T$ where only 30% of the events are in the diagonal. These migration matrices are obtained from the PROTOS sample with no anomalous couplings[3], where the parton level is well defined, and they are used as input of the ROOUNFOLDBAYES method from now on in order to unfold the reconstructed angular distributions.

Number of iterations

The convergence studies are performed using the POWHEG-BOX and ACERMC samples as well as the PROTOS sample with the SM couplings. The predicted angular distributions associated with these samples are unfolded with the resolution and efficiency corrections calculated with the SM PROTOS simulation.

Figures 5.4, 5.5, 5.6 and 5.7 show the evolution as a function of the number of iterations, n_{iter}, of the asymmetries extracted from the unfolded angular distributions. Three asymmetries are extracted simultaneously for the $\cos\theta^N$ (A^N_{FB}, A^N_+, A^N_-), $\cos\theta^T$ (A^T_{FB}, A^T_+, A^T_-) and $\cos\theta^*$ (A_{FB}, A_+, A_-) distributions, while just the forward-backward asymmetry can be extracted from $\cos\theta^l$. The unfolding procedure is considered to have converged when the absolute difference between the extracted asymmetries from two successive steps is lower than 0.001 for all the asymmetries that can be measured for a given angular distribution at the same time. With this criterion, we do not introduce a possible bias in the measurement by using a different number of iterations for each observable when they come from the same unfolded angular distribution. In the case of A^l_{FB}, where only this asymmetry is measured from the angular distribution $\cos\theta^l$, a more stringent convergence criterion is taken, considering that the method converges when the absolute difference between the measurements from two successive steps is lower than 0.0005.

The constant behaviour obtained with the PROTOS sample is due to the

[3] The PROTOS sample with no anomalous couplings will be refered to as "SM PROTOS sample" from now on.

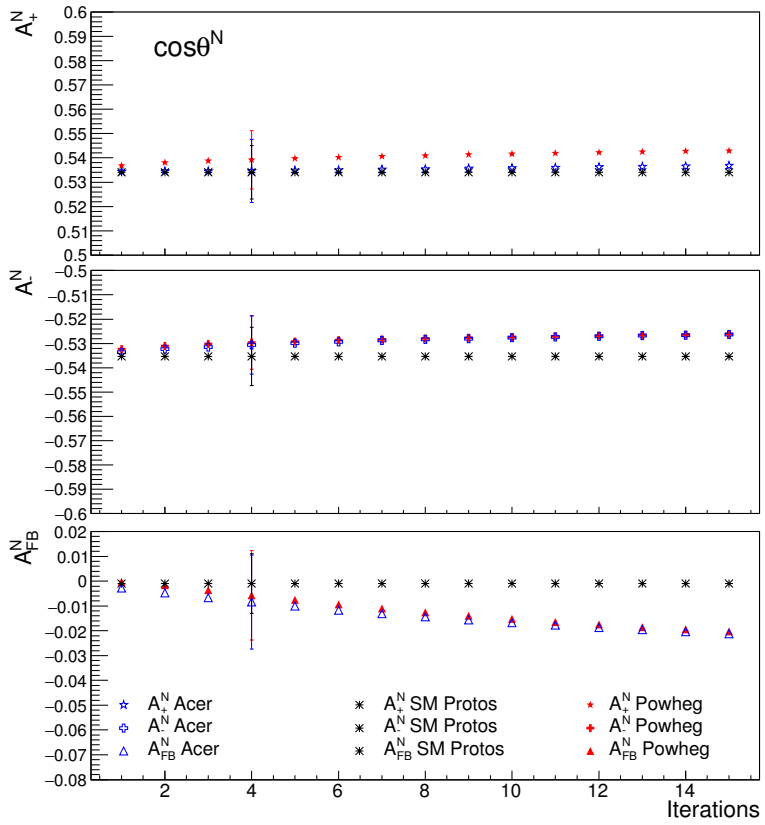

Figure 5.4: Asymmetries values as a function of the number of iterations of the Bayes algorithm for the unfolded angular distribution $\cos\theta^N$. The LO AcerMC (blue points), Protos (black points) and the NLO Powheg-Box (red points) simulation samples are used. The error bars represent the statistical uncertainties for the chosen numbers of iterations.

fact that the same sample of events is used to define the migration matrices and efficiencies as well as the distributions to be unfolded. The optimal number of iterations chosen to unfold each angular distribution is determined using the Powheg-Box sample, and the results are shown in Table 5.1. The only angular distribution that does not accomplish the convergence criterion is $\cos\theta^N$ with the A_{FB}^N asymmetry. In this case, the optimal number of iterations is determined by the other two asymmetries. While the values extracted for the asymmetries A_+^N and A_-^N are stable with respect to the number of iterations, a trend is observed for the A_{FB}^N asymmetry when the NLO Powheg-Box or the LO AcerMC simulated signal is unfolded. This can be explained by the non negligible events migration in the central region of the $\cos\theta^N$ angular distribution shown in Figure 5.2(a). The A_+^N and A_-^N asymmetries are not sensitive to the migrations between the two central bins, while any fluctuation

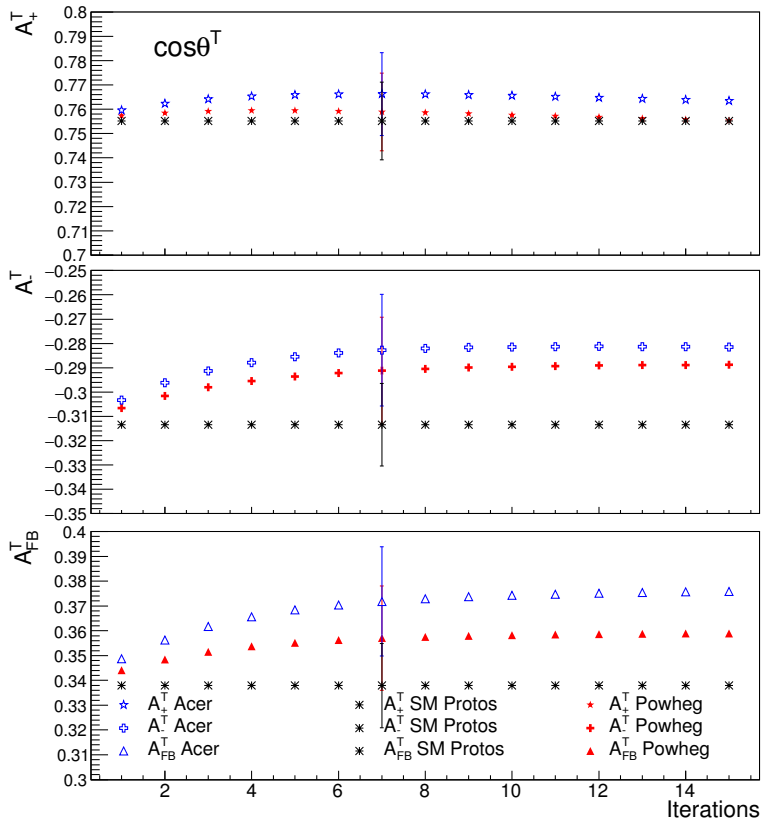

Figure 5.5: Asymmetries values as a function of the number of iterations of the Bayes algorithm for the unfolded angular distribution $\cos\theta^T$. The LO AcerMC (blue points), Protos (black points) and the NLO Powheg-Box (red points) simulation samples are used. The error bars represent the statistical uncertainties for the chosen numbers of iterations.

in those bins deviates the A_{FB}^N asymmetry from zero. In any case, the trend observed in A_{FB}^N is covered by the statistical uncertainty as it is shown in Figure 5.4.

The results displayed Figures 5.4 and 5.6 also show, in most cases, important shifts of the convergence curves between the Protos sample, the AcerMC and the Powheg-Box samples. The statistical uncertainties associated to each sample are drawn in each plot for the chosen number of iterations, representing the uncertainties due to the limited size of the tested samples. The statistical uncertainties do not cover completely the differences between the samples. This means that the unfolding response is very sensitive to the generator used to model the t-channel signal events. To take into account the differences in the unfolding response, a systematic uncertainty evaluated from the comparison between the measurement results obtained when unfolding the

Angular distribution	Number of iterations
$\cos\theta^N$	4
$\cos\theta^T$	7
$\cos\theta^*$	4
$\cos\theta^l$	6

Table 5.1: Numbers of Bayes iterations chosen to unfold the different angular distributions.

PROTOS and POWHEG-BOX angular distribution is properly considered and included in Section 5.2.1.3.

Closure test

The closure test checks the intrinsic bias of the unfolding algorithm using statistically independent event samples for the unfolded angular distributions and for the efficiency and migration corrections. To that end, the SM PROTOS sample is randomly split into two sub-sets of the same size, one sub-set is used to determine the corrections applied to unfold the angular distributions built from the second sub-set of events. The measurement results are then compared to the parton level values taking into account the expected statistical uncertainties related to the limited size of the Monte Carlo simulation samples.

The results of the closure test obtained using the iterative bayes unfolding for the different asymmetries are shown in Figure 5.8. For each measured asymmetry, the relative difference between the unfolded and parton level values is shown with the statistical uncertainty associated with the limited sizes of the split samples. One can see a good closure of the results, whatever the measured asymmetry. Within the expected statistical uncertainties, all the measurement results are compatible with the true parton level values. Therefore, no bias will be considered in the measurement of all asymmetries. Moreover, in Figure 5.8 the results obtained are compared with alternative unfolding procedures in order to check the reliability of the iterative Bayes unfolding method.

The alternative unfolding methods used are the SVD algorithm [123], which results are shown in red, and a simple inversion of the migration matrix, represented in green. The SVD algorithm consists in a single value decomposition of the migration matrix where a normalization term is added to regularize the solution[4]. The SVD algorithm is used to unfold the $\cos\theta^N$, $\cos\theta^T$ and

[4]The regularization parameter is an integer value that should be chosen between 2 and

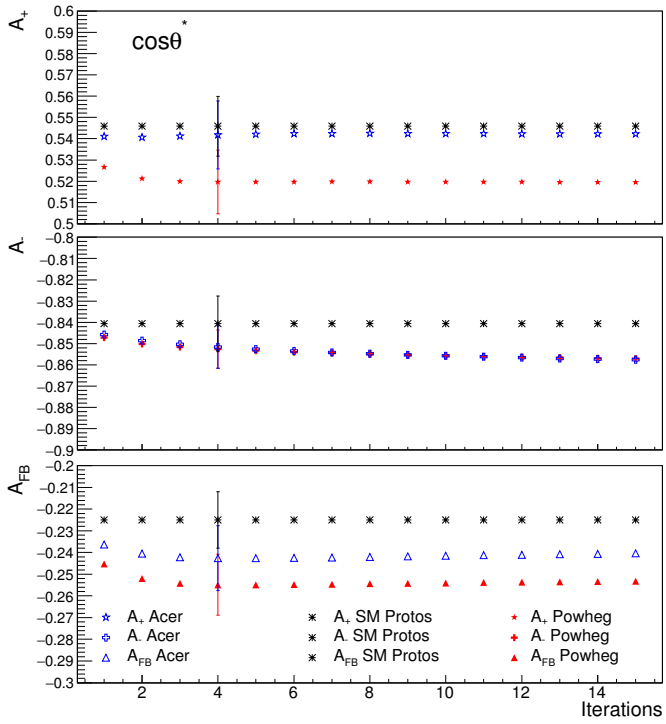

Figure 5.6: Asymmetries values as a function of the number of iterations of the Bayes algorithm for the unfolded angular distribution $\cos\theta^*$. The LO AcerMC (blue points), Protos (black points) and the NLO Powheg-Box (red points) simulation samples are used. The error bars represent the statistical uncertainties for the chosen numbers of iterations.

$\cos\theta^*$ angular distributions while the $\cos\theta^l$ distribution is unfolded using the matrix inversion procedure, since its migration matrix is a 2×2 matrix.

The results of the closure tests obtained with the alternative procedures show good agreement with the values given by the iterative Bayes unfolding method. Therefore, we do not need to add an additional systematic uncertainty due to the unfolding method. Slightly larger statistical uncertainties are obtained with the SVD and matrix inversion methods. Consequently, the iterative Bayes unfolding procedure is kept in order to perform the measurements.

Linearity test

The linearity test consists in measuring the response of the unfolding method when a simulated distribution with non standard Wtb couplings is unfolded. To that end, several Protos samples implementing non standard

the number of bins of the considered angular distribution.

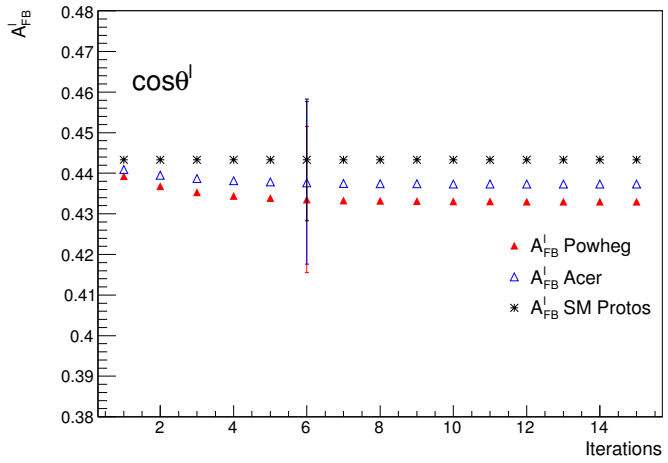

Figure 5.7: Asymmetries values as a function of the number of iterations of the Bayes algorithm for the unfolded angular distribution $\cos\theta^l$. The LO AcerMC (blue points), Protos (black points) and the NLO Powheg-Box (red points) simulation samples are used. The error bars represent the statistical uncertainties for the chosen numbers of iterations.

Wtb couplings are used. Then, the angular distributions predicted by these simulated samples are unfolded using the resolution and efficiency corrections calculated with the SM Protos sample. Finally, the extracted asymmetries are compared to the values derived from the parton level distributions.

The non-SM Protos samples can be categorized in three types: samples with non vanishing imaginary part of g_R ($\mathrm{Im}(g_R)$=$\pm 0.094, \pm 0.23$); samples with non vanishing real part of g_R ($\mathrm{Re}(g_R)$=$0.18, 0.07, -0.075, -0.131, -0.26$) and finally samples with non vanishing real part of V_R ($\mathrm{Re}(V_R)$=$0.25, 0.50$). The samples with $\mathrm{Im}(g_R) \neq 0$ where chosen following the recommendations from References [98] and [99], in order to explicitly check the linearity response of the unfolding method in the measurement of the asymmetry A^N_{FB}, which its value is proportional to the imaginary part of g_R ($A^N_{FB} = 0.64 P \mathrm{Im}(g_R)$). The values chosen for the real part of the couplings g_R and V_R were chosen following the recommendations from References [101] and [100]. These samples are useful to check the linearity response of the unfolding method in the measurement of the asymmetries sensitive to these couplings, like A_{FB} and A^l_{FB} respectively.

The results of the linearity test obtained for the forward-backward asymmetries are shown in Figures 5.9(a), 5.9(b), 5.10(a) and 5.10(b), where the extracted asymmetries as a function of their parton level values are shown. The lines corresponding to a linear response, with slope 1 and no offset, are also displayed.

For most of the observables, one can see an important spreading of the

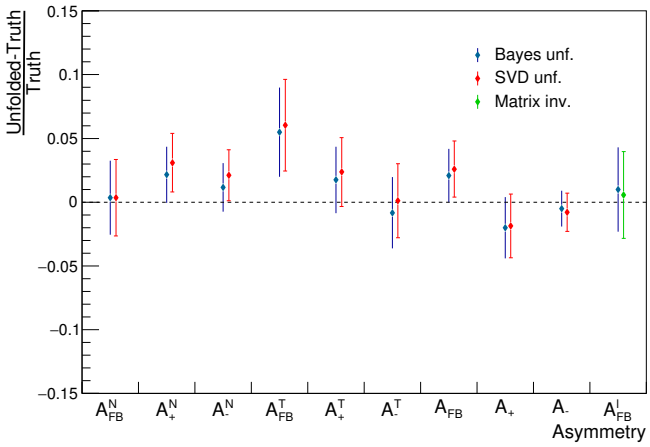

Figure 5.8: Relative differences between the asymmetry values derived from the unfolded and parton level angular distributions. The results obtained with the iterative Bayes unfolding, blue points, are compared with the ones obtained using the SVD algorithm, red points. The SM PROTOS sample is divided into two sub-sets, from which the unfolding corrections and the unfolded distributions are defined. The regularization parameter of the SVD algorithm is set to 4 in all cases. The error bars represent the statistical uncertainties due to the limited sizes of the two sub-samples. The horizontal dashed line corresponds to the closure. The absolute differences between the unfolded and parton level values are plotted for the A_{FB}^{N} asymmetry.

unfolded values around the linear response for the non SM PROTOS samples. Only the results of the SM PROTOS sample are in perfect agreement with what is expected. The closest behaviour to the linearity is found for the asymmetry A_{FB}^{N}, Figure 5.9(a), for which the configurations with $\mathrm{Im}(g_R) \neq 0$ were targeted. The response is almost linear with a slope not very far from 1. It should be noted that varying $\mathrm{Re}(g_R)$ or $\mathrm{Re}(V_R)$ has no impact on the asymmetry, which remains almost 0 after unfolding the $\cos\theta^{N}$ distribution.

It is also worthwhile to note that the asymmetry A_{FB}, which is related to the W boson helicity distribution, has unfolded values not strongly sensitive to the coupling $\mathrm{Re}(g_R)$, see Figure 5.10(a). A rather flat response is indeed found whatever the value of the coupling $\mathrm{Re}(g_R)$ is injected in the unfolded angular distribution. Therefore, a modest sensitivity on the coupling $\mathrm{Re}(g_R)$ is expected from the measurement of the asymmetries related with the $\cos\theta^{*}$, although a strong sensitivity is inferred from the theoretical calculations (see Figures 2 and 5 in Reference [51]).

In order to recover a linear response of the unfolding method, an iterative interpolation technique, based on the Lagrange polynomial approach, has been recently developed. These studies are beyond the scope of this thesis. The complete description of this method was recently published in Reference [124].

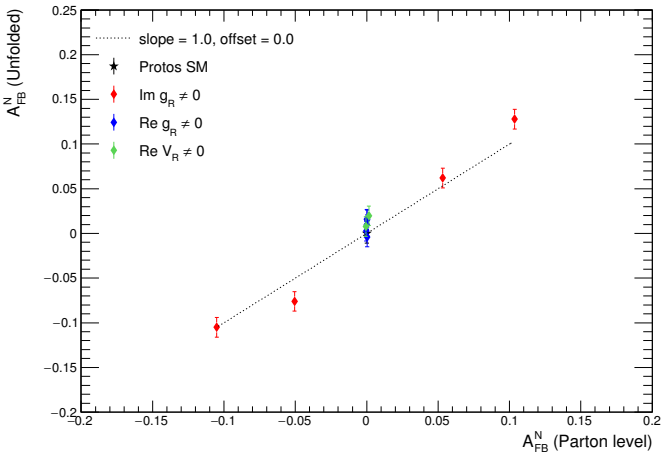

(a)

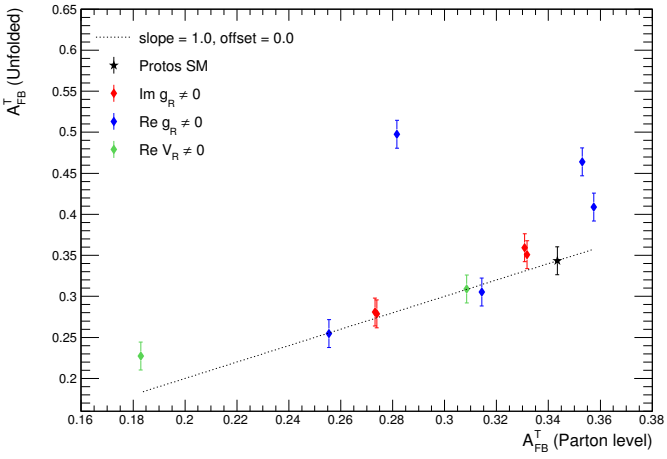

(b)

Figure 5.9: Asymmetries of the unfolded angular distributions as a function of the values at parton level A_{FB}^{N} (a), and A_{FB}^{T} (b). The PROTOS sample with the SM Wtb parametrization is displayed in black, while the PROTOS samples with non SM parametrization are shown in red ($\mathrm{Im}(g_R) \neq 0$), blue ($\mathrm{Re}(g_R) \neq 0$) and green ($\mathrm{Re}(V_R) \neq 0$). The error bars represent the uncertainties due to the limited statistics of the unfolded event distributions and the dashed line in each figure corresponds to the perfect linear response.

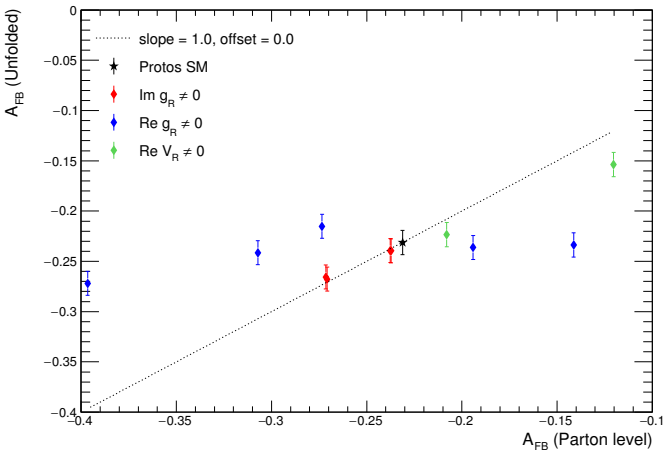

(a)

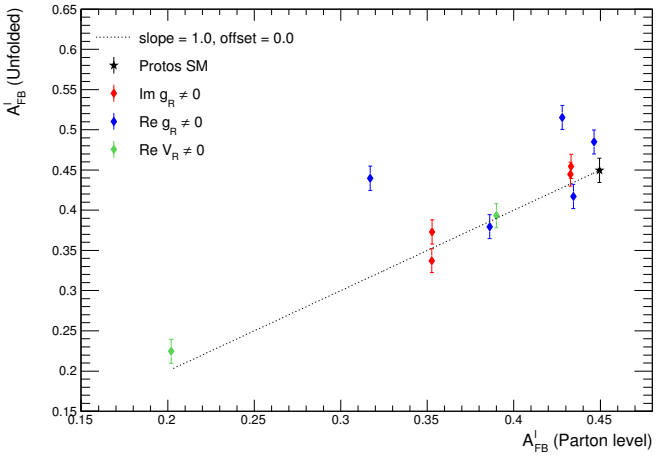

(b)

Figure 5.10: Asymmetries of the unfolded angular distributions as a function of the values at parton level A_{FB} (a), and A^l_{FB} (b). The PROTOS sample with the SM Wtb parametrization is displayed in black, while the PROTOS samples with non SM parametrization are shown in red ($\mathrm{Im}(g_R) \neq 0$), blue ($\mathrm{Re}(g_R) \neq 0$) and green ($\mathrm{Re}(V_R) \neq 0$). The error bars represent the uncertainties due to the limited statistics of the unfolded event distributions and the dashed line in each figure corresponds to the perfect linear response.

5.1.3 Final unfolding configuration

According to the results obtained from the different validation tests performed, the final configuration of the iterative Bayes unfolding method is the use of four bins for the $\cos\theta^N$, $\cos\theta^T$ and $\cos\theta^*$ angular distributions while two bins are used for the $\cos\theta^l$ angular distributions. The number of iterations used to unfold each angular distribution are those from the Table 5.1. Finally, as the scope of this thesis is to test the consistency of the SM predictions for the asymmetries A_{FB}^N, A_+^N, A_-^N, A_{FB}^T, A_+^T, A_-^T, A_{FB}^l and the helicity fractions F_0, F_L, F_R, obtained from the angular distributions $\cos\theta^N$, $\cos\theta^T$, $\cos\theta^l$ and $\cos\theta^*$, the data distributions will be unfolded using the efficiency corrections and migration matrices obtained from the SM Protos sample.

5.2 Uncertainties

In this section the treatment of the uncertainties that affect the measurement of the asymmetries is described. In addition to the statistical uncertainty, inherent to the limited size of the samples, the signal and background processes have systematic uncertainties which have an impact on the rate of the individual contributions as well as on the shape of their associated angular distributions. The different systematic uncertainties treated for this analysis are described in Section 5.2.1.

Once the different sources of systematic uncertainty are identified, we have to estimate their impact on the measurement of the asymmetries. The systematic and statistical variations described hereafter are propagated in a correlated way to the rates and to the shapes of the different angular distributions in the signal, $t\bar{t}$ and anti-signal regions simultaneously[5]. A set of scale factors associated to the top quark and W+jets backgrounds together with the t-channel signal events, are extracted for each source of systematic or statistical variation through the procedure explained in Chapter 4.3.3. The backgrounds are then re-normalized with the extracted scale factors before being subtracted to the data. Thanks to this procedure, the systematic and statistical uncertainties on the fitted normalization factors are propagated to the measured asymmetries. In section 5.2.2 is explained the procedure used to estimate the uncertainties.

[5]For the statistical uncertainties, the variations in the signal and control regions are considered as independent.

5.2.1 Sources of uncertainties

In addition to the statistical uncertainties, the systematic uncertainties can be grouped into three main categories: background normalization, detector modelling and signal and background modelling uncertainties.

5.2.1.1 Background normalization uncertainties

Cross section normalization: The event yields associated to the simulated $t\bar{t}$, single top, Z+jets and diboson processes are evaluated using the selection acceptances and the theoretically predicted cross sections. From the theoretical calculations of the cross sections, relative uncertainties of $\pm 6\%$, $\pm 7\%$ and $\pm 4\%$ are assigned to $t\bar{t}$, Wt and s-channel processes respectively. For the $t\bar{t}$ process, the PDF and α_s uncertainties, calculated using the PDF4LHC prescription with the MSTW2008 NNLO, CT10 NNLO and NNPDF2.3 5f FFN PDF sets, are added in quadrature to the QCD scale uncertainty. For the Z+jets process, a total cross section uncertainty of $\pm 20\%$ is considered as well as for the diboson contribution. For background processes that are merged in the statistical analysis presented in Chapter 4.3.3, the theoretical cross section uncertainties are combined in proportion to the contribution of each individual process in the selected event samples. In this manner, relative uncertainties of $\pm 6\%$ are considered for the $t\bar{t}$, Wt and s-channel. A relative uncertainty of $\pm 20\%$ is applied to the Z+jets and diboson backgrounds. For the W+jets normalization, a relative uncertainty of $\pm 20\%$ is considered; this uncertainty is evaluated from studies carried out with SHERPA samples generated with various configurations and reported in Reference [125].

The normalization uncertainties on the top quark background and W+jets processes are taken from the data driven fit procedure used to constrain the background normalizations and explained in Chapter 4.3.3. The constraints implemented in the fit are taken to the theoretical uncertainties discussed above. The uncertainties given by the likelihood fit and listed in Table 4.2 are propagated to the measurements by varying the total rates accordingly.

Multijet normalization: The multijet background is normalized through the data-driven analysis as described in Chapter 4.1. After studies varying the real/fake efficiencies, a relative systematic uncertainty of $\pm 70\%$ is assigned to this data-driven normalization.

Luminosity: The uncertainty on the integrated luminosity is ±1.9% [89]. The impact of this uncertainty is estimated by varying accordingly the overall normalizations of all Monte Carlo samples.

5.2.1.2 Detector modelling uncertainties

Lepton energy/momentum scale and resolution: The lepton momentum scale and resolution differ slightly between data and simulation and are corrected for, according to the charge of the lepton, by using reconstructed distributions of the $Z \to l^+l^-$ and $J/\psi \to l^+l^-$ masses [113, 126]. In the case of muons, momentum scale and resolution corrections are only apply to the simulation, while for electrons these corrections are applied to both data and simulation [113, 126].

Lepton reconstruction, trigger and identification efficiency: The charge-dependent reconstruction and identification efficiency of electrons and muons, their isolation, as well as the efficiency of the triggers used to record the event, differ slightly between data and simulation. The corrections to the simulation efficiencies are extracted via tag-and-probe techniques using $Z \to ll$ and $J/\psi \to \mu^+\mu$ events from data and simulation [112, 113], and the uncertainties associated with the tag-and-probe techniques are propagated through to the results.

Jet energy scale: The jet energy scale (JES) calibrates the measured calorimeter-level jet energy to the particle-level, taking into account the effect from neutrons, dead materials, other detector effects and algorithm specific biases. The JES and its uncertainty are derived by combining information from test-beam data, LHC collision data and simulation [127]. The JES is split into 22 uncorrelated sources, each of which can have different p_T and η dependencies.

Jet energy resolution: The jet energy resolution (JER) has been determined separately for data and simulation using two *in situ* techniques [128]. The fractional p_T resolution for a given jet is measured as a function of its p_T and η. A systematic uncertainty is defined as the difference between the JER for data and simulation and is applied as an additional smearing to the simulation.

Jet reconstruction efficiency: The jet reconstruction efficiency is derived by matching jets reconstructed from tracks to the calorimeter based jets. The uncertainty on the jet reconstruction efficiency is evaluated by randomly dropping jets from Monte Carlo events and determining the induced production rate variations [127].

Jet vertex fraction efficiency: The efficiency for each jet to satisfy the jet vertex fraction requirement is measured in $Z(\rightarrow l^+l^-)+$ 1-jet events in data and simulation [127], selecting separately events enriched in hard-scatter jets and events enriched in jets from other proton interactions in the same bunch crossing. The corresponding uncertainty is evaluated by changing the nominal JVF requirements value.

Jet b-tagging: The b-tagging efficiency scale factors, defined for b-quark, c-quark and light-flavour induced jets have been evaluated in data, and corresponding correction factors have been derived for jets in simulation [129,130]. These scale factors and their uncertainties are applied to the each jet depending on its flavour and p_T in the Monte Carlo simulations, leading to three uncorrelated sources of systematic uncertainties: b-tagging efficiency, c-tagging efficiency (which also includes the τ-tagging efficiency) and mis-tagging rate.

Missing transverse momentum: The missing transverse momentum is reconstructed from the leptons and jets in the event. The uncertainties from the energy scale and resolution of these objects are propagated into the calculation of the missing transverse momentum. The effects of the energy scale and resolution uncertainties on the cell out and soft jet terms are also included[6] [131].

5.2.1.3 Signal and background modelling uncertainties

Monte Carlo generator and parton shower modelling: The NLO generator modelling uncertainty associated with the single top t-channel is estimated by comparing the POWHEG-BOX+HERWIG sample with the alternative a MC@NLO+HERWIG one. The parton shower modelling uncertainty is estimated from the comparison between the POWHEG-BOX+PYTHIA and

[6]The cell out term is calculated from the cells in clusters which are not included in the reconstructed objects, while the soft jet term is reconstructed from cells in clusters associated to jets with 7 GeV$< p_T <$20 GeV.

POWHEG-BOX+HERWIG. All these samples have been produced using the detector ATLFAST-II simulation.

An additional generator uncertainty is considered for the signal process by comparing the NLO POWHEG-BOX+PYTHIA samples to the LO PROTOS+PYTHIA sample with the Standard Model parametrization of the Wtb couplings. This uncertainty takes into account the fact that the PROTOS sample is used to calculate the unfolding corrections, migration matrices and efficiencies. It also takes into account the differences in the detector simulation between the full and ATLFAST-II simulations. Note that no background contributions are considered when estimating this modelling uncertainty, since it is associated to the signal unfolding corrections.

For the $t\bar{t}$ and Wt background processes, the dependence on the Monte Carlo event generator is estimated by comparing the POWHEG-BOX+HERWIG and MC@NLO+HERWIG event samples. To estimate the uncertainty on the parton shower model on these background events, the POWHEG-BOX+PYTHIA and POWHEG-BOX+HERWIG samples are additionally compared. All these samples have been produced using the detector ATLFAST-II simulation.

For the single top quark s-channel background process, the dependence on the Monte Carlo event generator and parton showering is estimated from the full difference between the POWHEG-BOX+PYTHIA and the alternative MC@NLO+HERWIG event samples, both produced using the full detector simulation. For the Wt associated production, the systematic uncertainty associated to the NLO calculation schemes, namely the so-called diagram removal (DR) and diagram subtraction (DS), is also considered. It is evaluated by comparing POWHEG-BOX+PYTHIA samples generated with the two schemes. In this case both samples have been produced using the full detector simulation.

Scales and initial/final state radiation (IRS/FSR): The effects of varying the amount of radiation are studied by changing the hard-process and parton shower scales simultaneously in the POWHEG-BOX+PYTHIA simulations. In the single top quark samples the factorisation and renormalisation scales are increased or decreased by a factor of two or one-half, respectively, in combination with the Perugia 2012 radLo and radHi tunes [132]. In the $t\bar{t}$ samples, the parameter h_{damp} is set to m(top) or $2m$(top) with the radLo and radHi parametrisations, respectively. All these samples have been produced using the detector ATLFAST-II simulation.

Parton distribution functions: To estimate the systematic uncertainties related to the parton distribution functions (PDFs), the signal and all background simulation samples are reweighted according to each of the PDF uncertainty eigenvectors. The uncertainty is estimated, following the PDF4LHC prescription [133], by calculating the envelope of the uncertainties at 68% confidence level of the CT10 [134], MSTW2008nlo68cl [135] and NNPDF2.3 [136] sets and normalizing to the nominal cross-section. The largest up and down variations are then taken as systematic uncertainties.

5.2.2 Evaluation of the uncertainties

The impact on the measurement of the various sources of systematic uncertainties described in the previous section is determined in two ways according to the type of the uncertainty to be treated. Statistical uncertainties as well as background normalization and detector modelling uncertainties are computed using a frequentist method based on the generation of pseudo-experiments. On the other hand, signal and background modelling uncertainties are evaluated by comparing the values obtained for the measurements of the different observables with nominal samples to the ones obtained using a different set of samples with different configurations.

5.2.2.1 Pseudo-experiments method

The effects of the different sources of systematic uncertainties are estimated through random drawings with respect to the nominal event yields and template distributions of the considered polarisation observable, with these random drawings being constrained by the associated systematically varied sample. By performing the polarisation measurement from these pseudo-experiments, one obtains an estimator of the probability density of all possible outcomes of the measurement and the standard deviation of this estimator distribution is an estimator of the measurement uncertainty.

In each pseudo-experiment, the expectation values ($\tilde{\nu}_j$) associated with the different processes (labelled by index j) are varied within their normalization uncertainties. This is performed by throwing for each process j a random number (β_j^{pseudo}) according to a log-normal distribution with mean one and with the corresponding normalization systematic uncertainty (Δ_j) as width[7].

[7]The Δ_j values correspond to the uncertainties on the theoretical cross-sections for the simulated processes and on the data-driven normalization for the multijet background.

Using a log-normal distribution has the advantage of avoiding unphysical negative β_j^{pseudo} values. All the normalization variations are additionally convolved with a variation due to the uncertainty on the integrated luminosity through the drawing of a common random number (γ) according to a Gaussian distribution centred on one. The expected values for the background ($\tilde{\nu}_j$) and signal ($\tilde{\nu}_s$) processes are then varied by including the up and down rate uncertainties ($\epsilon_{ij}^{\pm}$) associated with the different systematic sources (labelled by index i). This is done by throwing a Gaussian distributed random number (δ_i) for each type i of systematic uncertainty using a mean of zero and a width equal to one. To create the pseudo-experiment, the varied expectation values are then given by:

$$\tilde{\nu}_j^{pseudo} = \gamma \cdot \beta_j^{pseudo} \cdot \tilde{\nu}_j \cdot \left[1 + \sum_i |\delta_i| \cdot \left(H(\delta_i) \cdot \epsilon_{ij}^{+} + H(-\delta_i) \cdot \epsilon_{ij}^{-}\right)\right] \quad , \quad (5.3)$$

where H denotes the Heaviside function. In the next step, the numbers of events (n_j) for the individual background and signal processes are determined from Poisson distributions with means $\tilde{\nu}_j^{pseudo}$. In the last step of the pseudo-experiment generation, a final distribution of the considered observable is built for each contributing process by drawing n_j times the observable value according to the corresponding template distribution defined by a set (α_{jk}^{pseudo}) of normalized event fractions. The up and down uncertainties on the template shapes ($\Delta\alpha_{ijk}^{\pm}$) are included by varying bin-by-bin (labelled by index k) the nominal distributions in a similar way than for the expectation values and using the same random number (δ_i):

$$\alpha_{jk}^{pseudo} = \left[\alpha_{jk} + \sum_i |\delta_i| \cdot \left(H(\delta_i) \cdot \Delta\alpha_{ijk}^{+} + H(-\delta_i) \cdot \Delta\alpha_{ijk}^{-}\right)\right] \quad . \quad (5.4)$$

The pseudo-experiments generated as described above are performed simultaneously in the signal and control regions, in order to compute the scale factors associated to the top quark, W+jets and t-channel contributions as explained in Chapter 4.3.3 and therefore propagating the uncertainties on the fitted normalization factors to the asymmetries.

Using pseudo-experiments also allows to estimate the statistical errors coming from the data; they are indeed included via the Poissonian drawings of the numbers of events n_j around the varied expectation values $\tilde{\nu}_j^{pseudo}$, providing

Systematic	ΔA_{FB}^{N}	ΔA_{+}^{N}	ΔA_{-}^{N}
Data statistics	0.022/-0.022	0.018/-0.018	0.017/-0.017
Simulation statistics	0.019/-0.019	0.014/-0.014	0.012/-0.012
Luminosity	0.000/-0.000	0.000/-0.000	0.000/-0.000
Background normalization	0.006/-0.006	0.006/-0.006	0.005/-0.005
Background modelling	0.015/-0.024	0.007/-0.005	0.012/-0.007
E_T^{miss} reconstruction	0.003/-0.003	0.006/-0.004	0.004/-0.004
Lepton reconstruction	0.002/-0.002	0.004/-0.003	0.003/-0.003
Jet reconstruction	0.009/-0.009	0.011/-0.011	0.015/-0.015
Jet energy scale	0.020/-0.033	0.010/-0.011	0.015/-0.022
Jet flavour tagging	0.003/-0.003	0.002/-0.002	0.002/-0.002
PDF	0.000/-0.000	0.000/-0.000	0.000/-0.000
$t\bar{t}$ ISR/FSR	0.004/-0.004	0.001/-0.001	0.007/-0.007
$t\bar{t}$ generator	0.002/-0.002	0.002/-0.002	0.008/-0.008
$t\bar{t}$ parton shower	0.015/-0.015	0.011/-0.011	0.004/-0.004
Wt,s-channel generator	0.003/-0.003	0.004/-0.004	0.002/-0.002
Wt,s-channel scale	0.006/-0.006	0.005/-0.005	0.006/-0.006
$t-$channel NLO generator	0.001/-0.001	0.017/-0.017	0.022/-0.022
$t-$channel LO-NLO generator	0.004/-0.004	0.005/-0.005	0.005/-0.005
$t-$channel parton shower	0.005/-0.005	0.001/-0.001	0.009/-0.009
$t-$channel generator scale	0.008/-0.008	0.014/-0.014	0.007/-0.007
Total systematic (quadratic sum)	+0.034/-0.047	+0.032/-0.031	+0.038/-0.040
Total (quadratic sum)	+0.041/-0.052	+0.037/-0.036	+0.041/-0.044

Table 5.2: Observed uncertainty breakdown for $\cos\theta^N$ asymmetries.

the rate statistical variations, and via the drawings of the resulting numbers of events according to the varied template distributions, obtaining in this latter case the shape statistical variations. The errors due to the limited size of the Monte Carlo simulation samples are additionally incorporated in the pseudo-experiments by throwing for each process a bin-per-bin random number according to a Gaussian distribution of mean one and of width equal to the statistical error associated with the bin, calculated from the root square of the quadratic sum of the event weights.

The software used to generate the pseudo-experiments is based on the Bill tool [137] developed by the Wuppertal group.

5.2.2.2 Uncertainty estimates from statistical, background normalization and detector modelling using pseudo-experiments

When performing pseudo-experiments based on the expected signal and background cross-sections and on the expected signal polarisation, the standard deviation of the output distribution of the measured observable gives its expected uncertainty. However, when using the measured cross-sections,

Systematic	ΔA_{FB}^{T}	ΔA_{+}^{T}	ΔA_{-}^{T}
Data statistics	0.029/-0.029	0.022/-0.022	0.034/-0.034
Simulation statistics	0.023/-0.023	0.018/-0.017	0.024/-0.024
Luminosity	0.000/-0.000	0.000/-0.000	0.000/-0.000
Background normalization	0.010/-0.010	0.004/-0.004	0.010/-0.010
Background modelling	0.016/-0.010	0.011/-0.007	0.017/-0.010
E_T^{miss} reconstruction	0.003/-0.003	0.004/-0.003	0.004/-0.005
Lepton reconstruction	0.013/-0.013	0.004/-0.005	0.014/-0.014
Jet reconstruction	0.009/-0.009	0.008/-0.008	0.015/-0.015
Jet energy scale	0.053/-0.053	0.035/-0.036	0.030/-0.021
Jet flavour tagging	0.006/-0.006	0.003/-0.003	0.005/-0.005
PDF	0.001/-0.001	0.001/-0.001	0.001/-0.001
$t\bar{t}$ ISR/FSR	0.006/-0.006	0.004/-0.004	0.013/-0.013
$t\bar{t}$ generator	0.036/-0.036	0.023/-0.023	0.023/-0.023
$t\bar{t}$ parton shower	0.013/-0.013	0.014/-0.014	0.008/-0.008
Wt,s-channel generator	0.007/-0.007	0.005/-0.005	0.002/-0.002
Wt,s-channel scale	0.006/-0.006	0.005/-0.005	0.005/-0.005
$t-$channel NLO generator	0.041/-0.041	0.008/-0.008	0.046/-0.046
$t-$channel LO-NLO generator	0.020/-0.020	0.004/-0.004	0.022/-0.022
$t-$channel parton shower	0.001/-0.001	0.001/-0.001	0.026/-0.026
$t-$channel generator scale	0.021/-0.021	0.012/-0.012	0.016/-0.016
Total systematic (quadratic sum)	+0.087/-0.086	+0.050/-0.050	+0.077/-0.073
Total (quadratic sum)	+0.092/-0.091	+0.055/-0.054	+0.084/-0.080

Table 5.3: Observed uncertainty breakdown for $\cos\theta^T$ asymmetries.

which are obtained from the measured scale factors with respect to the predicted cross-sections and the measured data distributions, the outcome of the pseudo-experiments provides in that case the observed uncertainty on the actual measurement.

To extract the individual contributions to the total uncertainty coming from the various sources described in previous section, pseudo-experiments are actually generated separately for each type of systematic uncertainty by giving as input only the corresponding varied rates and shapes and by drawing only the associated random numbers (nuisance parameters γ, β_j^{pseudo} or δ_i in Equations 5.3 and 5.4). The individual systematic uncertainties are then derived from the standard deviation of the corresponding output distributions. The contributions of the statistical errors are also estimated from dedicated pseudo-experiments which include only the statistical variations.

In case of an asymmetric response is obtained for a particular source of uncertainty, the difference between the mean and nominal values is added quadratically to the standard deviation to correct the up or down uncertainty according to the sign plus or minus of the calculated difference. The difference

Systematic	ΔA_{FB}	ΔA_{+}	ΔA_{-}
Data statistics	0.021/-0.021	0.024/-0.024	0.009/-0.009
Simulation statistics	0.016/-0.016	0.016/-0.016	0.009/-0.009
Luminosity	0.000/-0.000	0.000/-0.000	0.000/-0.000
Background normalization	0.006/-0.006	0.003/-0.003	0.003/-0.003
Background modelling	0.019/-0.019	0.007/-0.005	0.009/-0.008
E_T^{miss} reconstruction	0.008/-0.006	0.003/-0.003	0.005/-0.004
Lepton reconstruction	0.013/-0.013	0.008/-0.008	0.007/-0.007
Jet reconstruction	0.009/-0.009	0.001/-0.001	0.004/-0.004
Jet energy scale	0.031/-0.032	0.019/-0.018	0.014/-0.014
Jet flavour tagging	0.005/-0.005	0.002/-0.002	0.003/-0.003
PDF	0.000/-0.000	0.001/-0.001	0.000/-0.000
$t\bar{t}$ ISR/FSR	0.011/-0.011	0.005/-0.005	0.004/-0.004
$t\bar{t}$ generator	0.003/-0.003	0.004/-0.004	0.000/-0.000
$t\bar{t}$ parton shower	0.027/-0.027	0.018/-0.018	0.013/-0.013
Wt,s-channel generator	0.004/-0.004	0.005/-0.005	0.003/-0.003
Wt,s-channel scale	0.004/-0.004	0.005/-0.005	0.002/-0.002
$t-$channel NLO generator	0.008/-0.008	0.014/-0.014	0.001/-0.001
$t-$channel LO-NLO generator	0.028/-0.028	0.024/-0.024	0.011/-0.011
$t-$channel parton shower	0.022/-0.022	0.007/-0.007	0.011/-0.011
$t-$channel generator scale	0.007/0.007	0.014/-0.014	0.008/-0.008
Total systematic (quadratic sum)	+0.063/-0.063	+0.044/-0.043	+0.030/-0.029
Total (quadratic sum)	+0.067/-0.067	+0.050/-0.050	+0.031/-0.031

Table 5.4: Observed uncertainty breakdown for $\cos\theta^*$ asymmetries.

between the up and down uncertainties defines the bias of the measurement.

The total uncertainty on the measurement is estimated by adding quadratically all the individual uncertainty values extracted from the outcomes of separate pseudo-experiments.

5.2.2.3 Uncertainty estimates from signal and background modelling

Unlike in the case of statistical or detector modelling uncertainties, where all physical processes are varied at the same time in a similar manner using the pseudo-experiments method, the systematic variation of the signal and background modelling only affects one process at a time remaining the other processes unmodified. In other words, if we want to estimate the impact of the $t\bar{t}$ generator, only the $t\bar{t}$ sample is varied while the other processes remain unmodified using their nominal samples.

For each source of systematic, a Monte Carlo sample is defined as a reference sample while another one is defined as the systematic variation. Then, we obtain the different angular distributions using these samples. In order to

Systematic	ΔF_R	ΔF_L	ΔF_0
Data statistics	0.014/-0.014	0.033/-0.033	0.043/-0.043
Simulation statistics	0.013/-0.013	0.022/-0.022	0.030/-0.031
Luminosity	0.000/-0.000	0.000/-0.000	0.000/-0.000
Background normalization	0.004/-0.004	0.005/-0.005	0.008/-0.008
Background modelling	0.010/-0.009	0.005/-0.007	0.007/-0.007
E_T^{miss} reconstruction	0.006/-0.005	0.003/-0.003	0.004/-0.006
Lepton reconstruction	0.007/-0.007	0.008/-0.009	0.003/-0.002
Jet reconstruction	0.006/-0.006	0.002/-0.002	0.008/-0.008
Jet energy scale	0.014/-0.014	0.020/-0.021	0.015/-0.013
Jet flavour tagging	0.003/-0.003	0.002/-0.002	0.004/-0.004
PDF	0.000/-0.000	0.001/-0.001	0.001/-0.001
$t\bar{t}$ ISR/FSR	0.003/-0.003	0.005/-0.005	0.003/-0.003
$t\bar{t}$ generator	0.001/-0.001	0.005/-0.005	0.006/-0.006
$t\bar{t}$ parton shower	0.011/-0.011	0.021/-0.021	0.010/-0.010
Wt,s-channel generator	0.002/-0.002	0.006/-0.006	0.005/-0.005
Wt,s-channel scale	0.004/-0.004	0.007/-0.007	0.011/-0.011
$t-$channel NLO generator	0.007/-0.007	0.020/-0.020	0.027/-0.027
$t-$channel LO-NLO generator	0.006/-0.006	0.029/-0.029	0.023/-0.023
$t-$channel parton shower	0.013/-0.013	0.006/-0.006	0.007/-0.007
$t-$channel generator scale	0.010/-0.010	0.018/-0.018	0.019/-0.019
Total systematic (quadratic sum)	+0.031/-0.030	+0.052/-0.053	+0.049/-0.049
Total (quadratic sum)	+0.034/-0.034	+0.062/-0.063	+0.065/-0.065

Table 5.5: Observed uncertainty breakdown for W boson helicity fractions.

include these variations on top of the nominal angular distribution we define the shift per bin δ_i as:

$$\delta_i = \frac{\nu_i^{sys} - \nu_i^{ref}}{\nu_i^{ref}}, \tag{5.5}$$

where ν_i^{sys} is the number of events in bin i from the sample defined as systematic variation and ν_i^{ref} is the number of events in bin i from the sample defined as reference. Then, the nominal distribution is varied using this shift, defining the new nominal distribution which will be used to compute the systematic variation:

$$\nu_i^{new} = \nu_i^{nominal} \cdot (1 + \delta_i) \tag{5.6}$$

where $\nu_i^{nominal}$ is the number of events in bin i from the nominal distribution and ν_i^{new} is the number of events in bin i for the new distribution to be used.

Then, the new distribution replaces the nominal one for the process under study and after that, the nominal background is subtracted to the systematically varied distribution. Finally, the varied signal is unfolded and the observables are measured. The systematic uncertainty is defined as $\Delta = \pm|O' - O|$,

where O' is the observable value obtained from the varied signal and O is the nominal value of the observable.

A special case is considered when estimating the ISR/FSR systematic uncertainty. In this case, several samples with different configurations are defined as systematic samples. The procedure followed is the same as the explained above, but repeating it for each systematic sample. Then, the systematic uncertainty is defined as $\Delta = \pm\text{Max}(|O' - O|)$, where the maximum value obtained from the different samples used is the systematic uncertainty associated to the ISR/FSR.

5.2.2.4 Observed uncertainties

To estimate the observed systematic uncertainties, which correspond to the actual measurement of the polarisation observables, first we perform the variations to the angular distributions following the procedures explained above in the signal and control regions simultaneously. Then, the signal and background normalizations are re-scaled with the scale factors extracted from the likelihood fit to the real data distributions. After that, the pseudo-signal is obtained by subtracting to the data the re-normalized background contributions. Finally, the pseudo-signal is unfolded and the asymmetries are extracted.

The observed uncertainties obtained for each observable are shown in Tables 5.2 to 5.6. The largest contributions are due to the uncertainties in the modelling of the t-channel and $t\bar{t}$ processes and the jet energy scale components. The statistical uncertainty of the data sample, although lower than the systematic uncertainty, also has a sizeable impact on the measurement precision.

5.3 Results

The angular distributions from which the different asymmetries are measured are shown in Figure 5.11. As explained before, in order to extract the signal from these distributions the background contributions are subtracted after constraining their normalizations to the data. Subsequently, the extracted signal is unfolded using the iterative Bayes unfolding method using the setup described previously. The efficiencies and migration matrices used as input for the unfolding method are determined from the t-channel PROTOS simulation implementing the Standard Model values of the Wtb couplings.
Finally, the asymmetries are measured from the unfolded distributions.

Systematic	ΔA^{l}_{FB}
Data statistics	0.024/-0.024
Simulation statistics	0.025/-0.025
Luminosity	0.000/-0.000
Background normalization	0.007/-0.007
Background modelling	0.015/-0.014
E_T^{miss} reconstruction	0.007/-0.004
Lepton reconstruction	0.007/-0.005
Jet reconstruction	0.020/-0.020
Jet energy scale	0.043/-0.029
Jet flavour tagging	0.007/-0.007
PDF	0.001/-0.001
$t\bar{t}$ ISR/FSR	0.002/-0.002
$t\bar{t}$ generator	0.020/-0.020
$t\bar{t}$ parton shower	0.006/-0.006
Wt,s-channel generator	0.009/-0.009
Wt,s-channel scale	0.009/-0.009
$t-$channel NLO generator	0.014/-0.014
$t-$channel LO-NLO generator	0.013/-0.013
$t-$channel parton shower	0.003/-0.003
$t-$channel generator scale	0.011/-0.011
Total systematic (quadratic sum)	+0.062/-0.052
Total (quadratic sum)	+0.066/-0.057

Table 5.6: Observed uncertainty breakdown for $\cos\theta^{l}$ asymmetry.

The values measured for the asymmetries related to the top quark polarisation and to the W boson helicity fractions and polarisation observables are:

$$
\begin{aligned}
A^{l}_{FB} &= 0.486 \pm 0.024(stat.)\ ^{+0.062}_{-0.052}(syst.) &&= 0.486^{+0.066}_{-0.057}\\
A^{N}_{FB} &= -0.055 \pm 0.022(stat.)\ ^{+0.034}_{-0.047}(syst.) &&= -0.055^{+0.041}_{-0.052}\\
A^{N}_{+} &= 0.491 \pm 0.018(stat.)\ ^{+0.032}_{-0.031}(syst.) &&= 0.491^{+0.037}_{-0.036}\\
A^{N}_{-} &= -0.543 \pm 0.017(stat.)\ ^{+0.038}_{-0.040}(syst.) &&= -0.549^{+0.041}_{-0.044}\\
A^{T}_{FB} &= 0.384 \pm 0.029(stat.)\ ^{+0.087}_{-0.086}(syst.) &&= 0.384^{+0.092}_{-0.091}\\
A^{T}_{+} &= 0.765 \pm 0.022(stat.)\ \pm 0.050(syst.) &&= 0.765 \pm 0.055\\
A^{T}_{-} &= -0.255 \pm 0.034(stat.)\ ^{+0.077}_{-0.073}(syst.) &&= -0.261^{+0.084}_{-0.080}\\
A_{FB} &= -0.258 \pm 0.021(stat.)\ \pm 0.063(syst.) &&= -0.258 \pm 0.067\\
A_{+} &= 0.543 \pm 0.024(stat.)\ ^{+0.044}_{-0.043}(syst.) &&= 0.543 \pm 0.050\\
A_{-} &= -0.864 \pm 0.009(stat.)\ ^{+0.030}_{-0.029}(syst.) &&= -0.864 \pm 0.031
\end{aligned}
$$

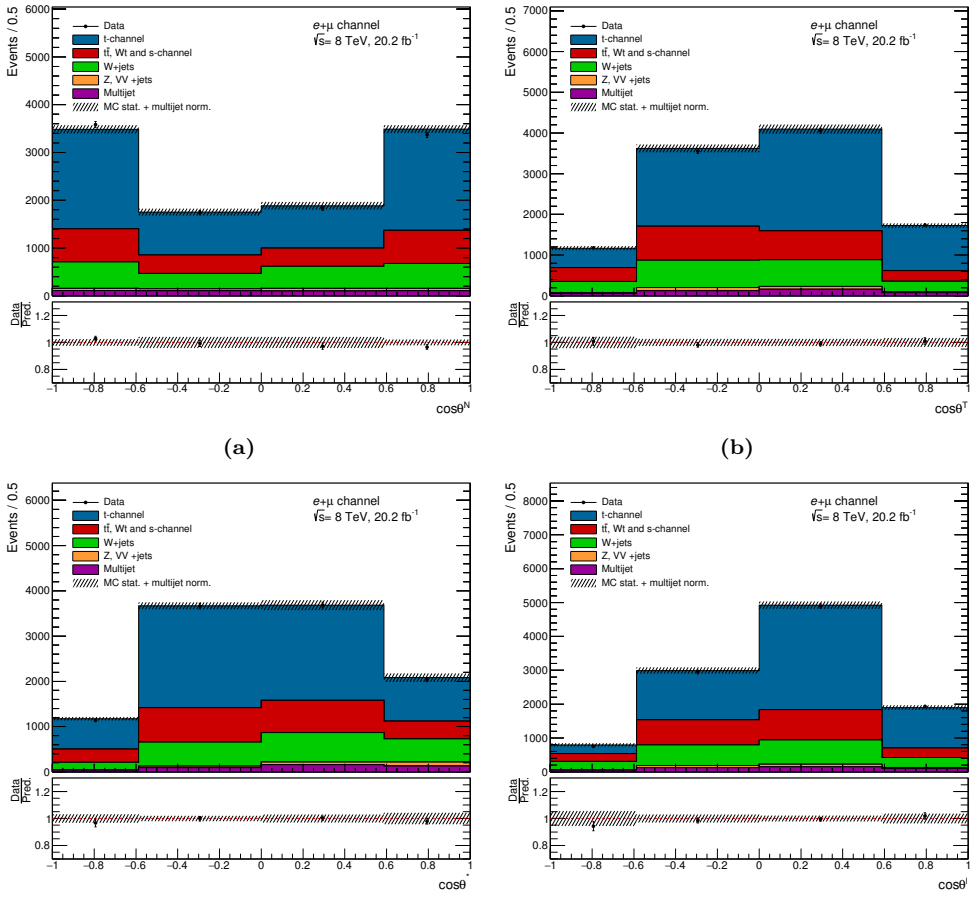

Figure 5.11: Angular distributions in the signal region used to measure the different observables: $\cos\theta^{LN}$ (a), $\cos\theta^{LT}$ (b), $\cos\theta^{S}$ (c), $\cos\theta^{X}$ (d). The normalization of the top quark and W+jets background contributions as well as the t-channel contribution are re-scaled using the values given in Table 4.2. The uncertainty bands correspond to the errors due to the limited size of the simulation samples added in quadrature with the data-driven normalization uncertainty estimated from the multijet contribution. The distributions associated with the electron and muon channels are combined.

From these asymmetries, the top quark polarisation P combined to the spin analysing power α_l and the W boson helicity fractions can be extracted as explained in Chapter 1.3. The values measured are:

$$\begin{aligned}
\alpha_l P &= 0.972 \pm 0.048(stat.) \ {}^{+0.124}_{-0.104}(syst.) &&= 0.972 \ {}^{+0.132}_{-0.114} \\
F_0 &= 0.737 \pm 0.043(stat.) \ \pm 0.049(syst.) &&= 0.737 \pm 0.065 \\
F_L &= 0.295 \pm 0.033(stat.) \ {}^{+0.052}_{-0.053}(syst.) &&= 0.295 \ {}^{+0.062}_{-0.063} \\
F_R &= -0.032 \pm 0.014(stat.) \ {}^{+0.031}_{-0.030}(syst.) &&= -0.032 \pm 0.034
\end{aligned}$$

Despite the non convergence of the unfolding method for the A_{FB}^{N} asymmetry, shown in Section 5.1.2, the result obtained for this asymmetry is consistent with the one published in Reference [124] ($A_{FB}^{N} = -0.04 \pm 0.02(stat.) \quad \pm 0.03(syst.)$), where two bins were used to measure the asymmetry instead of four and a perfect convergence of the unfolding method was found.

The overall compatibility of the measurements with the Standard model predictions is evaluated through the construction of a χ^2 statistic test taking into account all measured asymmetries with their correlations. The theoretical uncertainties, which are negligible compared to the measurement uncertainties, are not taken into account in the χ^2 calculation. The overall covariance matrix is computed from the sum of the covariance matrices associated with the various sources of statistical and systematic uncertainty. The overall p-value computed for the seven measured asymmetries[8] and the helicity fractions is found to be 0.91, thus, the measured observables are in agreement with the Standard Model.

[8]The helicity fractions have been used instead of the A_{FB}, A_{+} and A_{-} asymmetries in order to calculate the p-value.

CHAPTER 6

Conclusions

The first part of this thesis is focused on the alignment of the ATLAS Inner Detector tracking system. With the work developed and described in Chapter 3, the baseline track-based alignment algorithm was enriched with the application of new constraints, allowing for an efficient suppression of systematic biases on the reconstructed momentum as well as on the measured impact parameters of charged particles. To this end, two methods based on the study of $Z \to \mu^+\mu^-$ events have been developed. The first method consists in measuring shifts in the invariant mass of the Z boson (see Section 3.3.3) while the second one measures shifts in the impact parameters of muons originated from a Z boson decay, the latter being the first time it was included in the alignment procedure (see Section 3.3.5). In addition, physical detector movements driven by occasional environmental changes were tracked at the level of large detector structures in order to minimize their impact on the reconstruction, using as a new monitoring tool the web application described in Section 3.3.2. Measurements of the charge-antisymmetric momentum bias showed good uniformity across the entire acceptance of the detector. After the dedicated alignment described in Section 3.3.1, the biases on the reconstructed track impact parameters were measured to be below 1 μm in the transverse direction and under 10 μm along the beam line. All the knowledge gained during 2012 in the alignment procedure was applied to the data registered in 2010 and 2011, providing the latest and the best alignment constants for the Run I up to now.

Finally, the studies shown in Chapter 3 together with all the work developed by the alignment team in 2012 [85], was of great interest in order to understand the impact of the tracking system on the systematic uncertainties in the Higgs boson mass measurement [138]. An uncorrected momentum bias in tracks measured by the Inner Detector gave rise to systematic uncertainties on the momentum scale of the leptons, therefore affecting the mass measurements of the Higgs boson in the $H \rightarrow ZZ^* \rightarrow \mu\mu\mu\mu$ channel, but as it is shown in Chapter 3, the biases on momentum and impact parameters were minimized and kept under control. The effort done to the understanding of the experimental uncertainties affecting Higgs mass measurements was compiled in the communication note [139].

The second part of this thesis is focused on the study of the Wtb vertex through the measurement of the asymmetries related to the top quark and W boson polarisation observables, using t-channel single top quark events. To that end, the full dataset collected by ATLAS at $\sqrt{s} = 8$ TeV during 2012, with an integrated luminosity of 20.2 fb^{-1} has been analysed.

A feature of top quarks produced singly is that they are polarised along the direction of the light quark. This feature is exploited in the analysis by using t-channel single top events and building different frames that allow to measure various angular distributions of the top quark decay products. In the top quark rest frame, the vector triple product of the momentum direction $\vec{p}$ of the W boson and the top quark spin direction $\vec{s}$ defines the normal $\vec{N}$ direction. Then, the transverse $\vec{T}$ direction is obtained from the vector triple product of the normal direction and the momentum direction of the W boson. In this frame, we can measure the angular distribution of the momentum of the lepton between the normal and the transverse directions, which are the θ^N and θ^T distributions. For the W boson helicity fractions, the θ^* distribution is defined between the lepton in the W boson rest frame and the W boson momentum in the top quark rest frame, while for the top quark polarisation the angular distribution between the momentum of the lepton and the top quark spin direction (θ^l) is measured in the top quark rest frame. Using these angular distributions a set of asymmetries related to the W boson polarisation, the W boson helicity fractions and the top quark polarisation together with the spin analysing power of the lepton can be measured (see Section 1.3.2). The measurement of these observables, proposed in Reference [51], is of crucial importance since they are sensitive to anomalous couplings in the Wtb vertex, therefore, they can provide some hints about new sources of CP violation. For

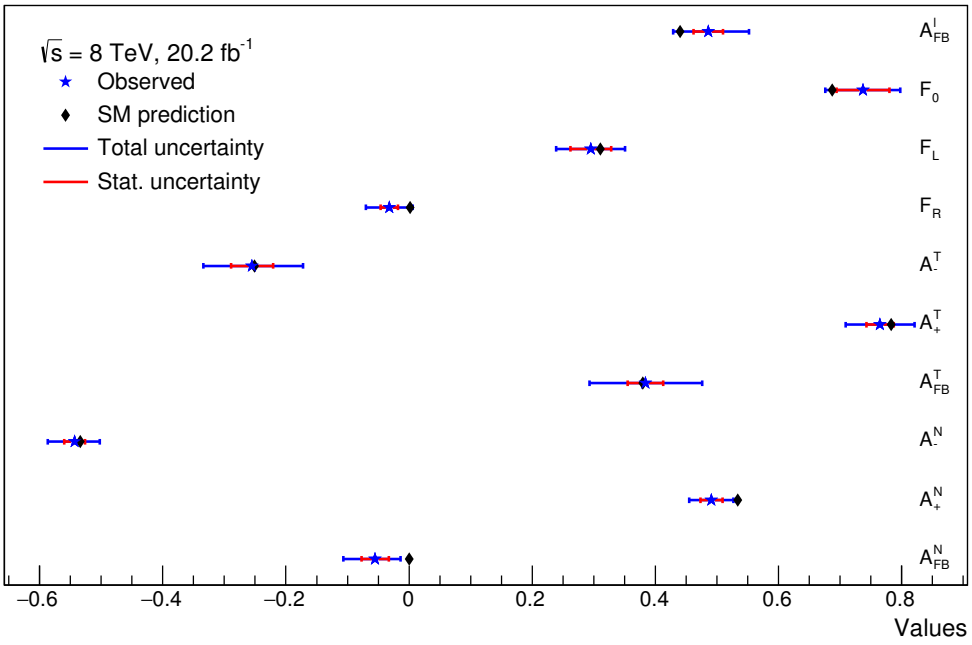

Figure 6.1: Summary of the measured asymmetries for the angular distributions $\cos\theta^N$, $\cos\theta^T$ and $\cos\theta^l$; and the W boson helicity fractions. All the measurements are compared with the Standard Model predictions.

instance, the asymmetry A_{FB}^N is proportional to the imaginary part of the tensor coupling g_R, therefore a non zero value of this asymmetry would imply CP violation.

The strategy followed in this analysis is similar to the $\sqrt{s} = 7$ TeV ATLAS measurement documented in Reference [98]. The experimental signature of t-channel single top quark candidate events is defined by one isolated charged lepton, electron or muon, large values of missing transverse energy and two jets, one of them being b-tagged. As described in Section 4.3, a cut based selection is applied in order to suppress background contributions and enhance the amount of t-channel events, obtaining a signal to background of about 1.30. The main background sources after the selection comes from $t\bar{t}$ and W+jets events. The normalization of the $t\bar{t}$ and W+jets background contributions together with the normalization of the t-channel signal events have been estimated through a likelihood fit to the data events, fitting simultaneously the three processes in the W+jets and $t\bar{t}$ control regions as well as in the signal region, as explained in Section 4.3.3. Then, all the background contributions are subtracted to the measured angular distributions and subsequently the signal is unfolded at parton level using the iterative Bayes method, described in Section 5.1. Statistical and systematic uncertainties were exhaustively eval-

uated using a elaborated methodology based on pseudo-experiments (see Section 5.2.2). Finally the asymmetries and the W boson helicity fractions are measured.

The values measured for the asymmetries are:

$$
\begin{aligned}
A_{FB}^{l} &= 0.486 \pm 0.024(stat.) \ ^{+0.062}_{-0.052}(syst.) &&= 0.486^{+0.066}_{-0.057} \\
A_{FB}^{N} &= -0.055 \pm 0.022(stat.) \ ^{+0.034}_{-0.047}(syst.) &&= -0.055^{+0.041}_{-0.052} \\
A_{+}^{N} &= 0.491 \pm 0.018(stat.) \ ^{+0.032}_{-0.031}(syst.) &&= 0.491^{+0.037}_{-0.036} \\
A_{-}^{N} &= -0.543 \pm 0.017(stat.) \ ^{+0.038}_{-0.040}(syst.) &&= -0.549^{+0.041}_{-0.044} \\
A_{FB}^{T} &= 0.384 \pm 0.029(stat.) \ ^{+0.087}_{-0.086}(syst.) &&= 0.384^{+0.092}_{-0.091} \\
A_{+}^{T} &= 0.765 \pm 0.022(stat.) \ \pm 0.050(syst.) &&= 0.765 \pm 0.055 \\
A_{-}^{T} &= -0.255 \pm 0.034(stat.) \ ^{+0.077}_{-0.073}(syst.) &&= -0.261^{+0.084}_{-0.080} \\
A_{FB} &= -0.258 \pm 0.021(stat.) \ \pm 0.063(syst.) &&= -0.258 \pm 0.067 \\
A_{+} &= 0.543 \pm 0.024(stat.) \ ^{+0.044}_{-0.043}(syst.) &&= 0.543 \pm 0.050 \\
A_{-} &= -0.864 \pm 0.009(stat.) \ ^{+0.030}_{-0.029}(syst.) &&= -0.864 \pm 0.031
\end{aligned}
$$

and the values measured for the top quark polarisation P combined to the spin analysing power α_l and the W boson helicity fractions are:

$$
\begin{aligned}
\alpha_l P &= 0.972 \pm 0.048(stat.) \ ^{+0.124}_{-0.104}(syst.) &&= 0.972 \ ^{+0.132}_{-0.114} \\
F_0 &= 0.737 \pm 0.043(stat.) \ \pm 0.049(syst.) &&= 0.737 \pm 0.065 \\
F_L &= 0.295 \pm 0.033(stat.) \ ^{+0.052}_{-0.053}(syst.) &&= 0.295 \ ^{+0.062}_{-0.063} \\
F_R &= -0.032 \pm 0.014(stat.) \ ^{+0.031}_{-0.030}(syst.) &&= -0.032 \pm 0.034
\end{aligned}
$$

The overall compatibility of the measurements with the Standard model predictions has been evaluated through the construction of a χ^2 statistic test taking into account all measured asymmetries with their correlations. The overall computed p-value is found to be 0.91, therefore the measured observables are in agreement with the Standard Model predictions. A summary plot comparing the measurements with its uncertainties is displayed in Figure 6.1.

The value measured for the A_{FB}^{N} asymmetry improves the result obtained in the previous ATLAS measurement performed at $\sqrt{s} = 7$ TeV [98]. The improvement is mainly due to the larger dataset sample recorded at $\sqrt{s} = 8$ TeV.

In this thesis is shown the first measurement of the W boson helicity fractions using t-channel single top events in ATLAS. This measurement is

traditionally performed using $t\bar{t}$ events, which benefits from the high statistic samples of such events due to its large production cross section. The results obtained could complement those obtained using $t\bar{t}$ events. Currently the best values obtained by the ATLAS [140] and CMS [141] collaborations using $t\bar{t}$ events at $\sqrt{s}$= 8 TeV are:

- ATLAS :

$$F_0 = 0.709 \pm 0.012(stat.) \pm 0.015(syst.)$$
$$F_L = 0.299 \pm 0.008(stat.) \pm 0.013(syst.)$$
$$F_R = -0.008 \pm 0.006(stat.) \pm 0.012(syst.)$$

- CMS :

$$F_0 = 0.681 \pm 0.012(stat.) \pm 0.023(syst.)$$
$$F_L = 0.323 \pm 0.008(stat.) \pm 0.014(syst.)$$
$$F_R = -0.004 \pm 0.005(stat.) \pm 0.014(syst.)$$

Finally, the analysis work done for this thesis has contributed to the publication [124]. In that publication a wider set of asymmetries have allowed an interpretation in terms of the W boson spin observables proposed in Reference [142].

CHAPTER 7

Resumen en español

La Física de Partículas, o Física de Altas Energías, es la rama de la ciencia que estudia los constituyentes elementales del Universo y sus interacciones fundamentales. Se considera que un constituyente es elemental cuando éste no tiene estructura interna, es decir, no está compuesto por ningún otro elemento. Actualmente sabemos que las partículas elementales se clasifican en dos grupos, fermiones y bosones, y que las interacciones fundamentales de la naturaleza son cuatro: la gravedad, el electromagnetismo, la fuerza nuclear débil y la fuerza nuclear fuerte. El modelo teórico que describe cómo se comportan las partículas elementales bajo tres de las cuatro fuerzas fundamentales se denomina Modelo Estándar. De acuerdo al Modelo Estándar, las fuerzas están descritas por el intercambio de bosones, siendo el fotón el responsable de la fuerza electromagnética, los bosones masivos W^+, W^- y Z los responsables de la interacción débil y los gluones los mediadores de la interacción fuerte. El bosón de Higgs es el responsable de la generación de las masas de las partículas fundamentales y los fermiones, que a su vez se clasifican en leptones y quarks, son los constituyentes de toda la materia ordinaria del Universo. Esta teoría se desarrolló durante los años 60 y 70 del siglo pasado y es la teoría que proporciona la descripción más precisa, actualmente, de los fenómenos subatómicos. Entre sus éxitos destacan la predicción de la existencia de diferentes partículas que han sido descubiertas posteriormente, como los bosones masivos W^+, W^- y Z, descubiertos en 1983 en el CERN, el quark top, descubierto en 1995 en Fermilab y por último el bosón de Higgs, descubierto en el CERN en 2012,

siendo éste la última pieza del Modelo Estándar que faltaba por descubrir. Sin embargo, a pesar de todos estos éxitos, aún quedan preguntas por responder a las cuales el Modelo Estándar no proporciona una solución satisfactoria. La gravedad no está incluida en el Modelo Estándar, no explica ni proporciona candidatos a la materia y energía oscura, y no explica por qué el universo está formado por materia y no antimateria. Esta última asimetría se denomina asimetría bariónica y es consecuencia de la violación de la simetría CP. En esta tesis se estudian varios observables relacionados con la polarización del quark top y del bosón W, los cuales son sensibles a posibles acoplamientos anómalos del quark top que a su vez pueden ser una fuente de violación de CP.

Para poder dar respuesta a estas preguntas hay que explorar la naturaleza a una escala de energías sin precedentes, para lo cual se ha diseñado el Gran Colisionador de Hadrones (LHC), que es operado por el Laboratorio Europeo de Física de Partículas (CERN). El concepto del LHC surge en 1984. Sin embargo, debido a limitaciones tecnológicas de la época, no pudo aprobarse el proyecto hasta 1994, comenzando su construcción en 1998 y finalizando ésta en el año 2008. El LHC es un acelerador y colisionador de partículas circular de 26.7 km de circunferencia, diseñado para acelear haces de protones con una energía máxima de 7 TeV, por lo que puede producir colisiones a una energía en el centro de masas de hasta $\sqrt{s}$= 14 TeV con una luminosidad instantánea de hasta $\mathcal{L}_{ins}$=10^{34}. El anillo del LHC está dividido en ocho regiones de inserción. Cuatro de estas regiones se utilizan para los sistemas de control de los haces: una región contiene el sistema de radiofrecuencia para acelerar las partículas y compensar las pérdidas de energía, otra región es utilizada para expulsar los haces y las dos restantes contienen el sistema de colimadores que se encarga de mantener el haz limpio de partículas que se desvían de la trayectoria nominal. En las otras cuatro regiones están colocados los diferentes detectores de partículas, los cuales se encargan de registrar el resultado de las colisiones que se producen en los puntos de interacción.

El trabajo desarrollado en esta tesis se enmarca dentro del experimento ATLAS, que es uno de esos cuatro detectores que operan en el LHC. El experimetno ATLAS está formado por una colaboración internacional de 37 países en el que trabajan unos 2500 científicos repartidos por todo el mundo. El proyecto del experimento se aprobó en 1994 y comenzó a instalarse en el punto de interacción del acelerador en el año 2004, finalizando su ensamblaje en el año 2008. El experimento ATLAS está situado a unos 100 m de pro-

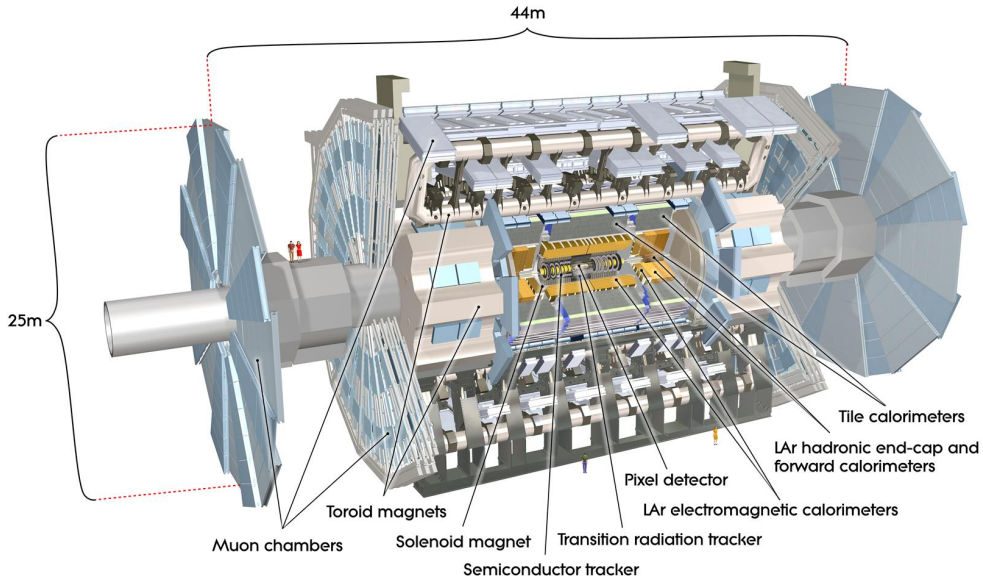

Figura 7.1: Plano del detector ATLAS.

fundidad en el túnel del LHC y es un detector multipropósito, de geometría cilíndrica, diseñado para explorar el Modelo Estándar y nueva física más allá de éste modelo. ATLAS está compuesto por tres subdetectores especializados en la detección de diferentes partículas. El subdetector más externo es el Espectrómetro de Muones (MS), especializado en la detección y en la medida del momento de los muones, la única partícula junto con los neutrinos que puede atravesar el detector. El MS está inmerso en un campo magnético toroidal, el cual se encarga de curvar la trayectoria de los muones para poder medir su momento. Este campo magnético está generado por ocho bobinas en la zona del barril y otras ocho en cada tapa del cilindro, como puede verse en la Figura 7.1. El MS junto con los imanes toroidales definen el volumen total de ATLAS. El siguiente subdetector situado en la región intermedia es el calorímetro. Éste está compuesto a su vez por el calorímetro electromagnético y el calorímetro hadrónico. El primero es el más interno y está diseñado para identificar y medir la energía de fotones, electrones y positrones. El calorímetro hadrónico está diseñado para medir la energía de los jets[1] así como determinar la energía transversa faltante, que es la energía que se llevan los neutrinos que escapan del detector sin ser medidos. El primer calorímetro utiliza argón líquido como medio ionizante y absorbedores de carga de plomo, y el segundo

[1]Un jet es un cono estrecho formado por un chorro de partículas que provienen de la hadronización de un quark o un gluón.

usa una tecnología de tejas centelleadoras con absorbedores de acero. El siguiente subdetector, el más cercano al haz de partículas, es el detector de trazas o Detector Interno (ID). Este subdetector está diseñado para reconstruir con gran precisión las trazas de las partículas cargadas que lo atraviesan, así como la reconstrucción de los vértices primarios y secundarios. El subdetector está inmerso en un campo magnético de 2 T generado por un solenoide que lo rodea y está formado por tres detectores. El más externo, denominado TRT, utiliza tubos de deriva. Los dos detectores restantes usan sensores con tecnología de silicio. El primero, denominado SCT, utiliza detectores de silicio de tipo microbanda y el más interno, denominado detector de Píxeles, utiliza píxeles como su propio nombre indica.

El buen funcionamiento del ID es crucial en el desarrollo de los análisis realizados en ATLAS, ya que practicamente la totalidad de ellos dependen de la reconstrucción de partículas y de algoritmos de identificación que utilizan las trazas reconstruidas por el ID. Para ello, no basta solamente con utilizar dispositivos de alta granularidad y resolución como los usados en el ID, sino que una buena calibración y alineamiento de los mismos son imprescindibles si pretendemos aprovechar completamente las capacidades del ID.

La primera parte del trabajo desarrollado para esta tesis ha consistido en mejorar las técnicas utilizadas en el alineamiento del ID durante la campaña de toma de datos del año 2012. El objetivo del alineamiento del ID consiste en determinar la posición y orientación de cada elemento que lo compone con la máxima precisión, ya que para conseguir los objetivos de física del experimento ATLAS, la degradación en la reconstrucción de las trazas debido a la incertidumbre introducida por el alineamiento del ID tiene que ser inferior al 20% con respecto la resolución intrínseca de cada elemento. Esto implica que la incertidumbre requerida en el alineamiento de los elementos que componen al Pixel y al SCT debe ser inferior a 7 μm y 12 μm respectivamente en el plano perpendicular al eje del haz de partículas, y una incertidumbre inferior a 120 μm en la determinación de la posición de cada tubo que componte el TRT en la dirección perpendicular al eje del tubo.

La técnica de alineamiento del detector interno consiste en la minimización de una función χ^2 construida con los residuos de las trazas, que podemos escribir en notación vectorial como sigue:

$$\chi^2 = \sum_t \mathbf{r}_t(\boldsymbol{\pi}, \mathbf{a})^T V^{-1} \mathbf{r}_t(\boldsymbol{\pi}, \mathbf{a}) \ , \tag{7.1}$$

Los residuos de una traza, $\mathbf{r}_t$, se definen como la distancia que existe entre el punto de impacto de la partícula en el módulo del detector y el punto de intersección de la traza reconstruida que cruza el mismo módulo. Esto hace que los residuos dependan funcionalmente de los parámetros de la traza, $\boldsymbol{\pi}$, y de la posición y orientación de los módulos en el espacio, $\mathbf{a}$. La matriz V es la matriz de covariancia de los errores de los impactos y el sumatorio se realiza sobre todas las trazas, t.

Al minimizar esta función con respecto a los parámetros de alineamiento, obtenemos las correcciones a las posiciones y orientaciones de cada módulo del detector para las cuales, los residuos de cada traza son mínimos. De esta manera, la distancia entre el impacto medido en el módulo y el punto de intersección de la traza reconstruida es mínima, por lo que la traza reconstruida será más parecida a la trayectoria real seguida por la partícula. Todo ello queda expresado en la siguiente ecuación:

$$\frac{d\chi^2}{d\mathbf{a}} = \frac{\partial\chi^2}{\partial\boldsymbol{\pi}}\frac{d\boldsymbol{\pi}}{d\mathbf{a}} + \frac{\partial\chi^2}{\partial\mathbf{a}} = 0 \ . \tag{7.2}$$

El término $d\boldsymbol{\pi}/d\mathbf{a}$ da cuenta de la dependencia de los parámetros de la traza con respecto a las correcciones de alineamiento. Este término es el que marca la diferencia entre los dos tipos de algoritmos usados en el alineamiento del ID, llamados *Local* χ^2 y *Global* χ^2. El algoritmo *Local* χ^2 asume que los parámetros de la traza no dependen de las correcciones de alineamiento ($d\boldsymbol{\pi}/d\mathbf{a} = 0$), lo que implica que la traza reconstruida permanece fija mientras que los módulos se reajustan para minimizar la función χ^2. Sin embargo, el algoritmo *Global* χ^2 asume que los parámetros de la traza sí dependen de las correcciones de alineamiento ($d\boldsymbol{\pi}/d\mathbf{a} \neq 0$), por lo que la minimización de la función χ^2 se logra ajustando simultáneamente la traza reconstruida y la posición de los módulos. Esto puede comprenderse fácilmente ya que al corregir las posiciones de los módulos las posiciones de los impactos de las partículas cambian, por lo que generan una nueva traza reconstruida descartando la anterior. Cabe destacar que la implementación de estos algoritmos en el código de alineamiento permiten alinear el ID con diferentes niveles de granularidad, que van desde alinear cada subdetector como un todo hasta alinear cada módulo que compone el ID, es decir, alinear más de 350000 elementos con hasta seis grados de libertad cada uno.

A pesar de que los algoritmos utilizados proporcionan una descripción precisa de la geometría del detector, es posible encontrar distorsiones en el

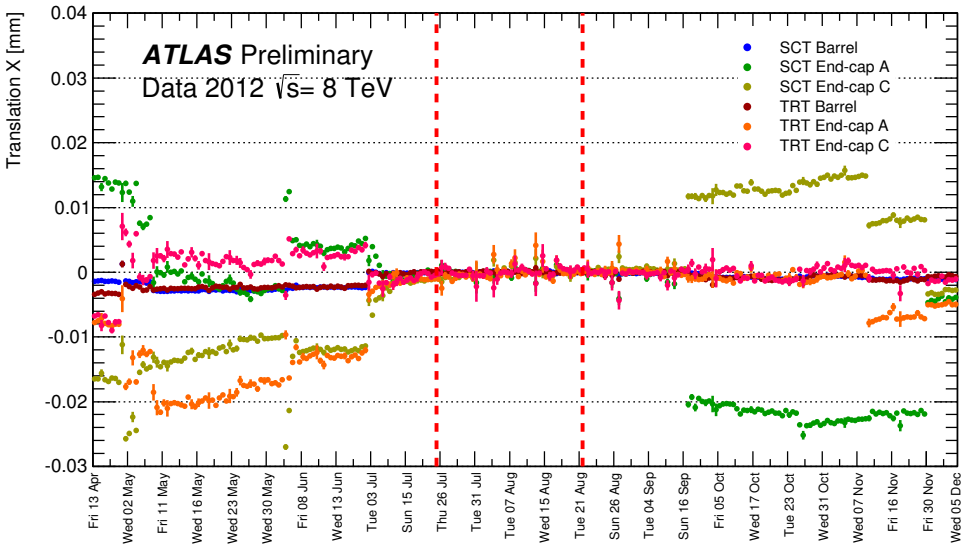

Figura 7.2: Correcciones a nivel 1 en la componente X de la traslación de los distintos subdetectores con respecto al Pixel, que se considera fijo, durante el año 2012. En este nivel el Pixel se considera como un único elemento mientras que el SCT y el TRT se consideran que están formados por un barril y sus dos tapas. Las líneas representan el periodo de mayor estabilidad, en el cual se obtuvieron unas correcciones de alineamiento promedio.

mismo que preservan la trayectoria helicoidal de las trazas permaneciendo la función χ^2 invariante. Estas distorsiones conducen a sesgos sistemáticos en las medidas de magnitudes físicas y reciben el nombre de modos débiles. Estos modos débiles se corresponden con soluciones singulares de la ecuación de autovalores 7.2. Por tanto, atendiendo solamente al criterio de minimización de los residuos no es suficiente para garantizar la calidad del alineamiento del ID y proveer unas correcciones a la geometría del detector libre de sesgos.

En el trabajo desarrollado para esta tesis se realizaron varias contribuciones que han permitido reducir el impacto de los modos débiles y que han sido implementadas en el procedimiento estándar para el alineamiento del ID en ATLAS [85].

La primera contribución consiste en el desarrollo de una aplicación web para la monitorización de las correcciones de alineamiento run[2] a run. Al finalizar un run, éste entra en lo que se denomina bucle de calibración, que consiste en un periodo de 48 horas en las que todos los sistemas de ATLAS realizan las calibraciones necesarias para garantizar la calidad de los datos registrados durante el run. En este periodo se realizan dos iteraciones a nivel 1 de alineamiento, es decir, se alinean las estructuras más grandes del ID. La

[2]Se denomina run al periodo de tiempo en el cual el detector ATLAS está registrando datos.

aplicación de monitorización comprueba que las dos iteraciones hayan finalizado y actualiza la base de datos que registra todos los datos de interés para el grupo de alineamiento de ATLAS.

De esta forma, se facilita la generación de gráficas con la evolución de las correcciones de alineamiento al usuario que esté realizando un turno operacional dedicado a evaluar el buen funcionamiento del alineamiento del ID. Con esta información, el usuario puede decidir si es necesario aplicar las correcciones de alineamiento al run recién procesado, en caso de que éstas no sean despreciables, dentro del bucle de calibración. En la Figura 7.2 se muestran las correcciones obtenidas para la componente X de la traslación de los distintos elementos alineados durante el año 2012. Esta herramienta entró en funcionamiento a finales del año 2011 en el Run I y se sigue utilizando actualmente en el Run II.

Gracias a este procedimiento, el sesgo en el momento de las partículas introducido por los modos débiles se redujo en la campaña de toma de datos de 2012. La mayor reducción del sesgo en momento obtenido al aplicar estas correcciones se observan en los extremos del ID, como puede verse en las Figuras 7.3(a) y 7.3(b), que muestran el estado anterior a la aplicación de las correcciones, y en las Figuras 7.3(c) y 7.3(d), que muestran el estado final. Esas regiones se corresponden con las tapas del SCT y TRT, que son más sensibles a movimientos debidos a causas externas como por ejemplo el apagado y encendido del sistema de imanes, problemas en la criogenia, etc, como puede observarse en la Figura 7.2. Aunque en valor promedio el sesgo en el momento varía poco (Figuras 7.3(e) y 7.3(f)), este procedimiento corrige las distorsiones locales del detector, reduciendo la dispersión de la distribución del sesgo en momento hasta un 50 %, como puede verse en las Figuras 7.3(e) y 7.3(f).

La segunda contribución novedosa desarrollada para este trabajo de tesis, y que ha sido incluida en el procedimiento estándar de alineamiento del ID, es la reducción del sesgo en los parámetros de impacto. En la Ecuación 7.2 pueden añadirse términos adicionales que añadan información adicional acerca del estado del detector. Estos términos introducen ligaduras entre las variables que componen el sistema de ecuaciones, por lo que reducen la contribución de modos débiles a añadir algún tipo de sesgo en los parámetros de las trazas. Con esta idea, se introduce un método en el algoritmo de alineamiento para reducir el sesgo en los parámetros de impacto de las trazas. Para ello se utilizan parejas de muones que provengan de la desintegración de un bosón Z. La traza de cada muón es registrada por distintas zonas del detector, pero al

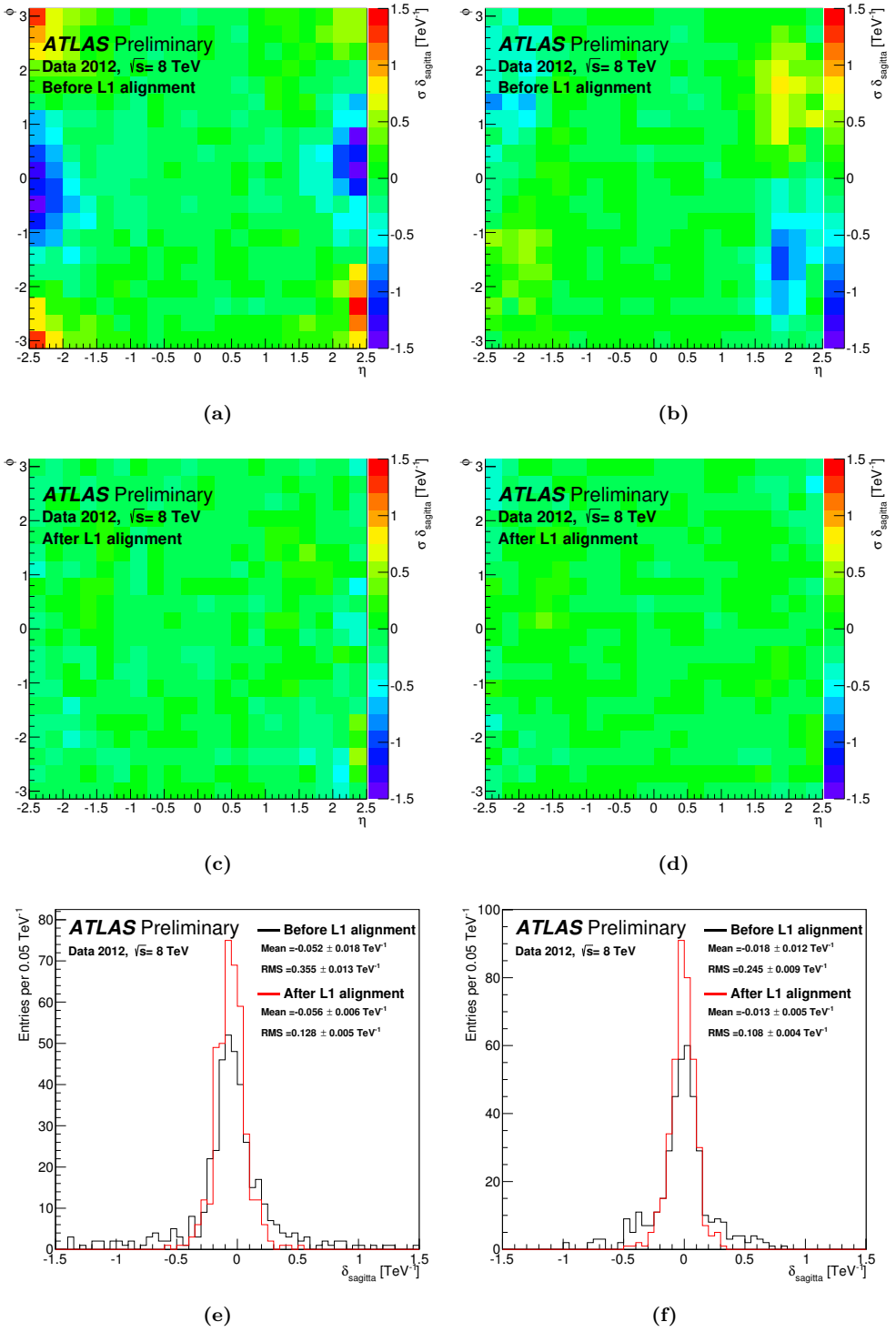

Figura 7.3: En estas gráficas se muestran los resultados obtenidos para el periodo A de toma de datos (del 4 al 16 de abril de 2012) en la izquierda, y para el periodo H en la derecha (del 13 al 26 de octubre de 2012). En la parte superior las Figuras (a) y (b) muestran el sesgo existente inicialmente en el momento de las trazas en el detector para sus respectivos periodos. En la parte central, las Figuras (a) y (b), muestran el sesgo en el momento después de aplicar las correcciones de alineamiento de nivel 1. Finalmente en la zona inferior, las Figuras 7.3(e) y 7.3(f) muestran en un histograma el valor de los sesgos en cada punto del detector antes de aplicar las correcciones (curva negra) y después (curva roja).

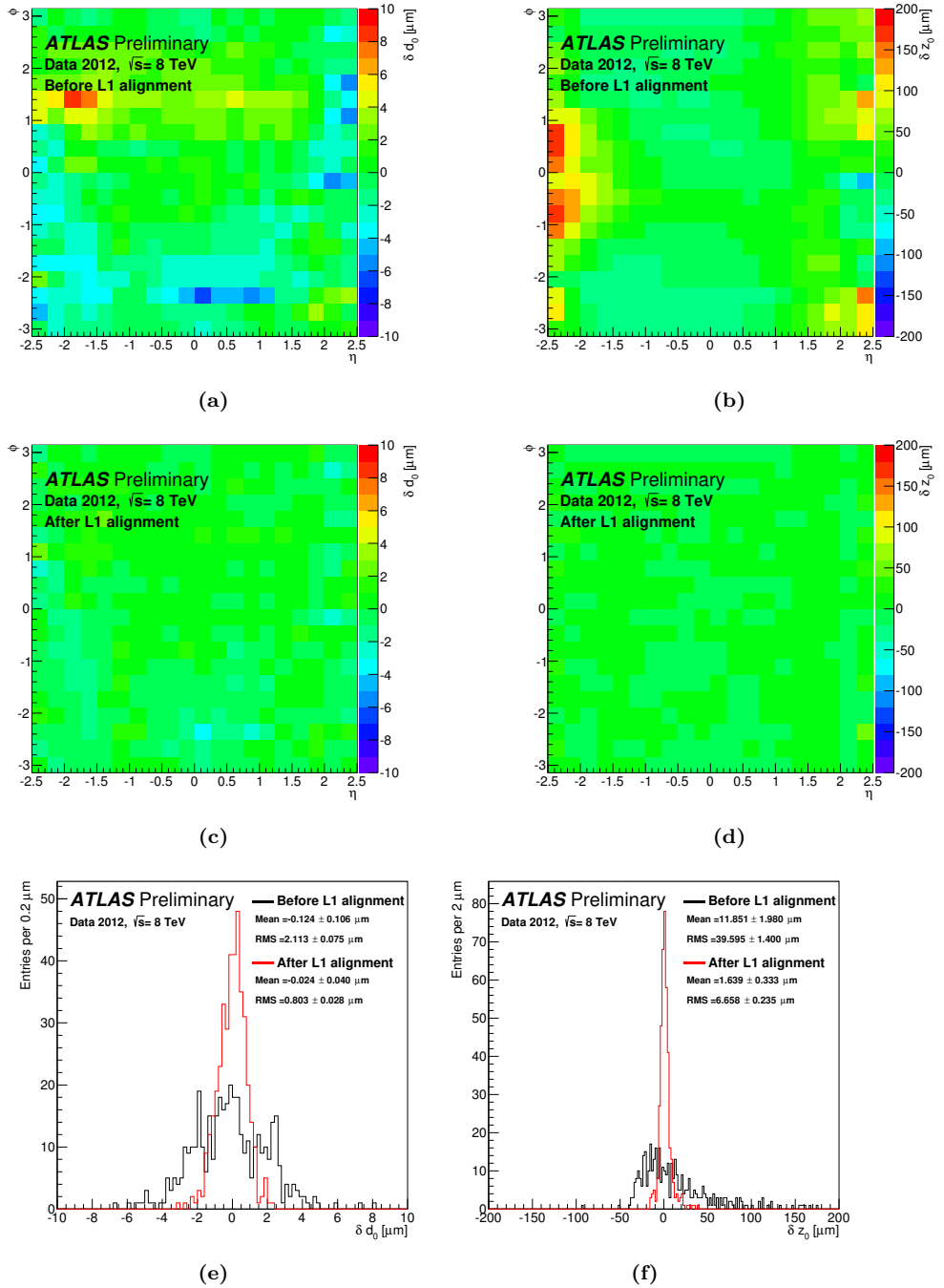

Figura 7.4: En estas gráficas se muestran los resultados obtenidos para la eliminación del sesgo en los parámetros de impacto transversal, gráficas de la izquierda, y transversal, gráficas de la derecha. En la zona superior se muestran los sesgos iniciales del detector. En la zona central se muestran los sesgos medidos después de aplicar las correcciones, donde se puede observar una respuesta homogénea del detector. Finalmente en la zona inferior se muestran en un histograma el valor de los sesgos en cada punto del detector antes de aplicar las correcciones (curva negra) y después (curva roja). Los datos usados fueron registrados entre el 22 de julio y el 24 de agosto de 2012.

tener el mismo origen, deben tener los mismos parámetros de impacto. El sesgo se mide como la diferencia entre los parámetros de impacto medidos para cada muón como función de η y ϕ, creando así un mapa bidimensional de los sesgos como los mostrados en las Figuras 7.4(a) y 7.4(b). En esas figuras se muestran los sesgos iniciales en el detector, antes de aplicar cualquier corrección, y puede observarse que los sesgos se localizan en los extremos del detector. Esta información se introduce en el algoritmo de alineamiento y se procede al cálculo de un nuevo conjunto de correcciones para las posiciones y orientaciones de los elementos que participan en el alineamiento a nivel 1. El resultado obtenido al aplicar estas nuevas correcciones queda reflejado en las Figuras 7.4(c) y 7.4(d), donde puede observarse como los sesgos iniciales que afectaban a los parámetros de impacto han sido reducidos de forma uniforme en todo el detector. Como puede verse en las Figuras 7.4(e) y 7.4(f), el valor medio del sesgo en el parámetro de impacto longitudinal, z_0, ha sido reducido en un 85% mientras que el sesgo en el parámetro de impacto transversal, d_0, ha sido reducido en un 80%. También se ha reducido notablemente la dispersión de estos sesgos, un 60% para d_0 y un 80% para z_0, lo cual hace que la respuesta del detector sea más homogénea.

Las mejoras que proveen estos nuevos métodos desarrollados en durante la campaña de toma de datos de 2012 también fueron aplicados a los datos registrados durante 2010 y 2011, proveyendo las últimas y mejores correcciones de alineamiento para el Run I hasta ahora.

La segunda parte del trabajo desarrollado para esta tesis consiste en la medida de observables relacionados con la polarización del quark top y del bosón W usando eventos con quarks top producidos en solitario y en el canal t.

Como se ha mencionado antes, el quark top fue descubierto en 1995 y tiene una serie de propiedades que lo hacen único entre el resto de quarks. Su vida media es del orden de $\tau \sim 10^{-25}$ s, y por tanto más corta que la escala de tiempos típica de los procesos de QCD. Esto implica que el quark top se desintegre antes de que la hadronización tenga lugar, por lo que prácticamente permite estudiar un quark libre. El top quark se desintegra mediante la interacción débil a través del vértice Wtb produciendo un bosón W y un quark b con prácticamente un 100% de probabilidad. Esto contrasta con la producción del quark top, el cual puede ser producido en parejas top-antitop mediante interacción fuerte o en solitario mediante interacción débil. La ventaja de estudiar el quark top usando eventos con quarks top producidos en

solitario con respecto a usar eventos con parejas top-antitop consiste en que el mismo proceso físico ocurre tanto en la producción como en la desintegración del quark top. Esto permite estudiar la interacción débil y en particular el vértice Wtb reduciendo la contaminación de procesos de QCD. Como hemos dicho antes, el quark top se desintegra antes de hadronizar, por lo que toda la información sobre su estado de spin se transfiere a los productos de su desintegración. Esta información se diluye en los procesos que involucran parejas de quarks top-antitop debido a interacciones de QCD, pero esto no sucede cuando el quark top ha sido producido en solitario. Además, en el caso de producción en el canal t, el quark top está polarizado en la misma dirección y sentido que el quark ligero que interviene en el proceso de producción.

La parametrización más general del lagrangiano que describe el vértice Wtb puede escribirse como [50] :

$$\mathcal{L}_{Wtb} = -\frac{g}{\sqrt{2}}\bar{b}\gamma^{\mu}(V_L P_L + V_R P_R)tW_{\mu}^{-} - \frac{g}{\sqrt{2}}\bar{b}\frac{i\sigma^{\mu\nu}}{M_W}(g_L P_L + g_R P_R)tW_{\mu}^{-} + \text{h.c.}, \tag{7.3}$$

la cual introduce momentos anómalos del quark top, donde V_L y V_R parametrizan los acoplamientos vectoriales mientras que g_L y g_R los tensoriales. En el Modelo Estándar, estos parámetros se reducen a V_L=V_{tb} y V_R=g_R=g_L= 0, por lo que medir observables sensibles a estos parámetros resultan de gran interés, en especial aquellos que puedan ser sensibles a la parte imaginaria de g_R, que de ser distinta de cero implicaría que se viola la simetría CP.

En el análisis desarrollado se miden los siguientes observables, definidos en la Referencia [51].

Fracciones de helicidad del bosón W El bosón W producido en la desintegración del quark top puede presentar tres estados de polarización: longitudinal (F_0), levógira (F_L) o dextrógira (F_R). La probabilidad de encontrar el bosón W en alguno de estos estados está relacionada con la anchura de desintegración del quark top como sigue:

$$\Gamma(t \to Wb) = \Gamma_L + \Gamma_0 + \Gamma_R, \tag{7.4}$$

$$1 = \frac{\Gamma_L}{\Gamma} + \frac{\Gamma_0}{\Gamma} + \frac{\Gamma_R}{\Gamma} = F_L + F_0 + F_R \ . \tag{7.5}$$

A continuación, la distribución angular que sigue el leptón producido en

la desintegración del bosón W puede ser escrita como :

$$\frac{1}{\Gamma}\frac{d\Gamma}{d\cos\theta^*} = \frac{3}{8}(1-\cos\theta^*)^2 F_L + \frac{3}{4}\sin^2\theta^* F_0 + \frac{3}{8}(1+\cos\theta^*)^2 F_R \ , \qquad (7.6)$$

donde el ángulo θ^* es el ángulo medido entre el momento del leptón en el sistema de referencia del bosón W en reposo y el momento del bosón W medido en el sistema de referencia del quark top en reposo (ver Figura 7.5).

De la distribución angular se pueden definir distintos puntos con respecto a los cuales medir diferentes asimetrías que proporcionan la misma información que las fracciones de helicidad, pero que resultan más fáciles de medir que las fracciones. Las asimetrías se definen de la siguiente forma:

$$A_z = \frac{N(\cos\theta^* > z) - N(\cos\theta^* < z)}{N(\cos\theta^* > z) + N(\cos\theta^* < z)}, \qquad (7.7)$$

por lo que, en función del valor z, se definen tres asimetrías que contienen la misma información que las fracciones de helicidad:

$$z = 0 \rightarrow A_{FB} = \frac{3}{4}(F_R - F_L), \qquad (7.8)$$

$$z = -(2^{2/3}-1) \rightarrow A_+ = 3\beta[F_0 + (1+\beta)F_R], \qquad (7.9)$$

$$z = (2^{2/3}-1) \rightarrow A_- = -3\beta[F_0 + (1+\beta)F_L]. \qquad (7.10)$$

Fracciones de polarización del bosón W Estos observables explotan el hecho de que el quark top producido en solitario en el canal t está polarizado en la dirección y sentido del quark ligero. Teniendo en cuenta la Ecuación 7.6 para los ángulos θ^N y θ^T definidos en la Figura 7.5, se definen las fracciones de polarización normales (F_0^N, F_+^N, F_-^N) y transversas (F_0^T, F_+^T, F_-^T). Considerando las Ecuaciones 7.8–7.10 para estos ángulos, se obtienen las asimetrías normales (A_{FB}^N, A_+^N, A_-^N) y las transversas (A_{FB}^T, A_+^T, A_-^T). De todo este conjunto de observables sensibles a acoplamientos anómalos del quark top, cabe destacar la asimetría A_{FB}^N, la cual es directamente proporcional a la parte imaginaria del tensor de acoplamiento g_R [51].

Polarización del quark top Con este observable se puede medir el grado de polarización del quark top usando la dirección definida por el momento del leptón y la dirección del momento del quark ligero, ambos medidos en el sistema de referencia del quark top en reposo como se describe en la Figura

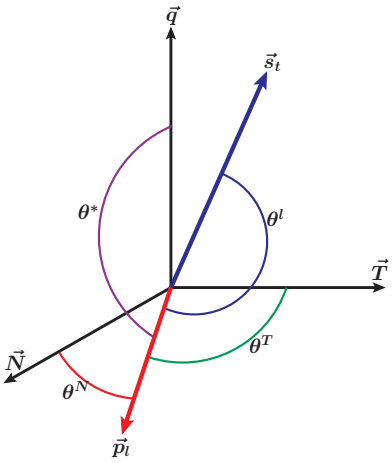

Figura 7.5: El sistema de referencia de polarización es un sistema de referencia cartesiano, dextrógiro, definido por el momento del bosón W medido en el sistema de referencia del quark top en reposo ($\vec{q}$) y los ejes normal y transverso, donde $\vec{N} = \vec{s}_t \times \vec{q}$ y $\vec{T} = \vec{q} \times \vec{N}$. Los ángulos que podemos medir son : θ^*, que es el ángulo entre el momento del leptón ($\vec{p}_l$) medido en el sistema de referencia del bosón W en reposo y el momento del bosón W en el sistema de referencia del quark top en reposo; θ^N, que es el ángulo entre el momento del leptón cargado medido en el sistema de referencia del bosón W en reposo y el eje normal y θ^T, que es el ángulo entre el momento del leptón cargado medido en el sistema de referencia del bosón W en reposo y el eje transverso. El ángulo θ^l está relacionado con la polarización del quark top y es el ángulo medido entre el momento del leptón y el momento del quark ligero ($\vec{s}_t$), estando ambas partículas en el sistema de referencia del quark top en reposo.

7.5. En este caso sólo una asimetría puede medirse $A_{FB} = 0.5\alpha_l\mathcal{P}$, la cual es proporcional a la polarización del quark top, $\mathcal{P}$, y al poder analizador del leptón, α_l.

El análisis que se presenta en esta tesis consiste en una medida de las asimetrías anteriormente descritas junto con las fracciones de helicidad del bosón W, usando la muestra de datos de 20.2 fb^{-1} registrados por ATLAS con una energía en el centro de masas de $\sqrt{s}$= 8 TeV.

Los candidatos a eventos con producción de quark top en solitario y en el canal t son seleccionados de la muestra mediante un proceso de selección de dos pasos basados en cortes. El primer paso, llamado preselección, consiste en la aplicación de unos cortes que se corresponden con la firma básica que deja este tipo de eventos en el detector. Los requerimientos de la preselección son: eventos con al menos un candidato a vértice primario; que contengan exactamente un candidato a leptón aislado; con exactamente dos jets, y uno de ellos etiquetado como b-jet; la energía faltante transversa del evento debe ser superior a 30 GeV; la masa transversa del bosón W reconstruido debe ser superior a 50 GeV; y por último, el momento del lepton debe cumplir la

condición:

$$\frac{p_T(l)}{\left(1-\frac{\pi-|\Delta\phi(l,\mathrm{jet}_l)|}{\pi-1}\right)} > 40\mathrm{GeV}\ . \tag{7.11}$$

Una vez que tenemos una muestra de eventos que satisfacen los criterios de preselección realizamos el siguiente paso del análisis, que consiste en separar los eventos candidatos en diferentes regiones cinemáticas. En total se definen cuatro regiones, tres de ellas se denominan de control y la última es la región de señal. Las regiones de control son ortogonales a la región de señal y se construyen para estudiar el modelado de los procesos que forman el fondo. De esta forma obtenemos una buena estimación de los eventos de fondo que contribuyen en la región de señal. La primera región de control se denomina $t\bar{t}$, ya que el fondo de parejas de quarks top-antitop contribuyen al ∼80% del total. Esta región de control está definida por los mismos cortes aplicados para la preselección con la diferencia en el número de jets requeridos, los cuales son cuatro siendo uno de ellos un b-jet. La segunda región de control se denomina antiselección, y está formada por todos los eventos que satisfacen los requerimientos de preselección pero que no cumplen los requerimientos de selección. En esta región los fondos dominantes son los eventos formados por parejas de quarks top-antitop y los eventos de W+jets. Por último, la región de control denominada W+jets consiste en eventos que satisfacen los criterios de selección salvo por el algoritmo de identificación de b-jets, cuyo criterio de identificación se relaja y se eliminan los eventos que satisfagan la identificación de b-jets más restrictiva requerida para la preselección. Por último, la región de señal está definida por unos cortes más exigentes para reducir las contribuciones de los fondos y tener una muestra más pura de quarks top producidos en solitario en el canal t. Los eventos que componen esta región se caracterizan por satisfacer los siguientes requisitos:

- La pseudorapidez del jet ligero debe ser $|\eta| > 2$.
- La separación en η entre el jet ligero y el jet etiquetado como b-jet debe ser mayor que 1.5
- La masa del quark top reconstruido debe estar comprendida entre 130 GeV y 200 GeV.
- La suma de los momentos transversos del leptón, de los jets y la energía transversa faltante debe ser mayor que 195 GeV.

La relación señal/fondo obtenida con esta configuración de cortes es de S/R

= 1.30 para la región de señal, siendo los fondos predominantes los eventos de parejas de quarks top-antitop (18%) y eventos de W+jets (18%), mientras que los eventos con quarks top producidos en solitario en el canal t representan el 57% del total de eventos.

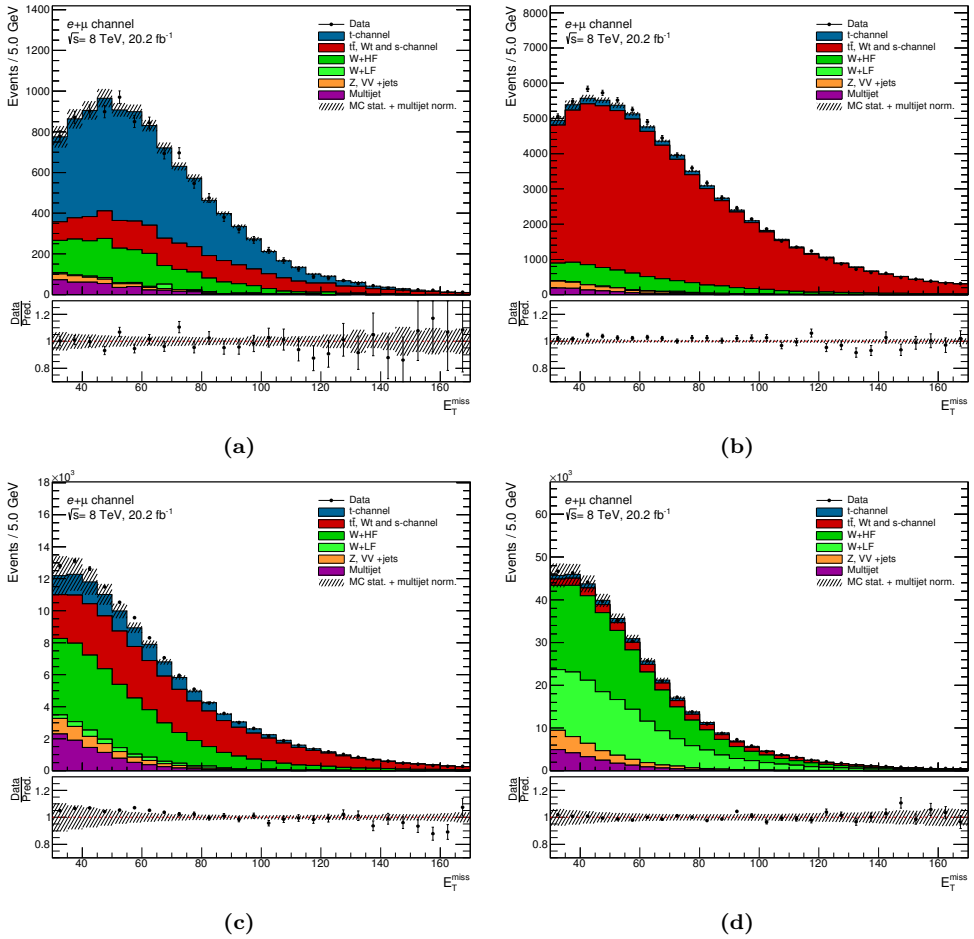

Figura 7.6: Distribucion de la energía faltante transversa obtenida para las regiones: señal (a), $t\bar{t}$ (b), antiselección (c) y W+jets (d).

Las regiones de control $t\bar{t}$ y antiselección junto con la región de señal, se utilizan para calcular la estimación del fondo. Esta estimación se realiza calculando unos factores de escala que corrigen la normalización de los procesos $t\bar{t}$, W+jets y procesos con quarks producidos en solitario. Los factores de escala se calculan mediante un ajuste de máxima verosimilitud de una función de probabilidad que tiene en cuenta el número de eventos observados en las tres regiones de control, y la cantidad de eventos esperados de cada proceso. Estos factores de escala calculados se aplican tanto en las regiones de control como en la región de señal, ya que una buena estimación del fondo es crucial

Distribución angular	Iteraciones	Número de bines
$\cos\theta^N$	4	4
$\cos\theta^T$	7	4
$\cos\theta^*$	4	4
$\cos\theta^l$	6	2

Tabla 7.1: Configuración final utilizada para realizar la deconvolución de cada distribución angular.

para poder realizar la medida. La región de control de W+jets no interviene en este proceso ni se le aplican los factores de escala así obtenidos, debido a que la contribución de W+jets que domina esa región tiene una composición de sabores diferente a las del resto de regiones.

Para realizar la medida de las diferentes asimetrías se ha utilizado una técnica de deconvolución llamada *"Iterative Bayesian Unfolding"* [121, 122], utilizada ampliamente en la colaboración ATLAS. Esta técnica consiste en recuperar la distribución original, eliminando el efecto de la eficiencia de los cortes y las distorsiones del detector, mediante el uso iterativo del teorema de Bayes, siendo el número de iteraciones el parámetro de regularización del método. Los ingredientes de entrada que necesita el método para realizar la deconvolución de la señal son la matriz de migraciones y la distribución a nivel de partones de las distintas distribuciones angulares descritas previamente. Para obtener las distribuciones a nivel de partones y sus correspondientes matrices de migración, se han generado diferentes muestras simuladas de eventos con quarks top producidos en solitario en el canal t mediante el generador de Monte Carlo Protos. En particular, la muestra producida con los parámetros del vértice Wtb ajustados a los valores del Modelo Estándar es la utilizada para configurar el algoritmo de deconvolución.

Esta técnica ha sido validada diseñando diferentes tests para poder determinar la configuración optima del algoritmo de deconvolución. Se han realizado tests de convergencia, tests de cierre y se ha comprobado la compatibilidad de los resultados obtenidos con otros métodos de deconvolución. La Tabla 7.1 muestra la configuración óptima del método de deconvolución para cada distribución angular. Los parámetros de la configuración son el número de iteraciones que realiza el algoritmo *"Iterative Bayesian Unfolding"*, así como el número de bines utilizados para construir el histograma de cada distribución angular.

Finalmente, los distintos observables son medidos después de sustraer los fondos nominales simulados a la distribución de datos reales para cada dis-

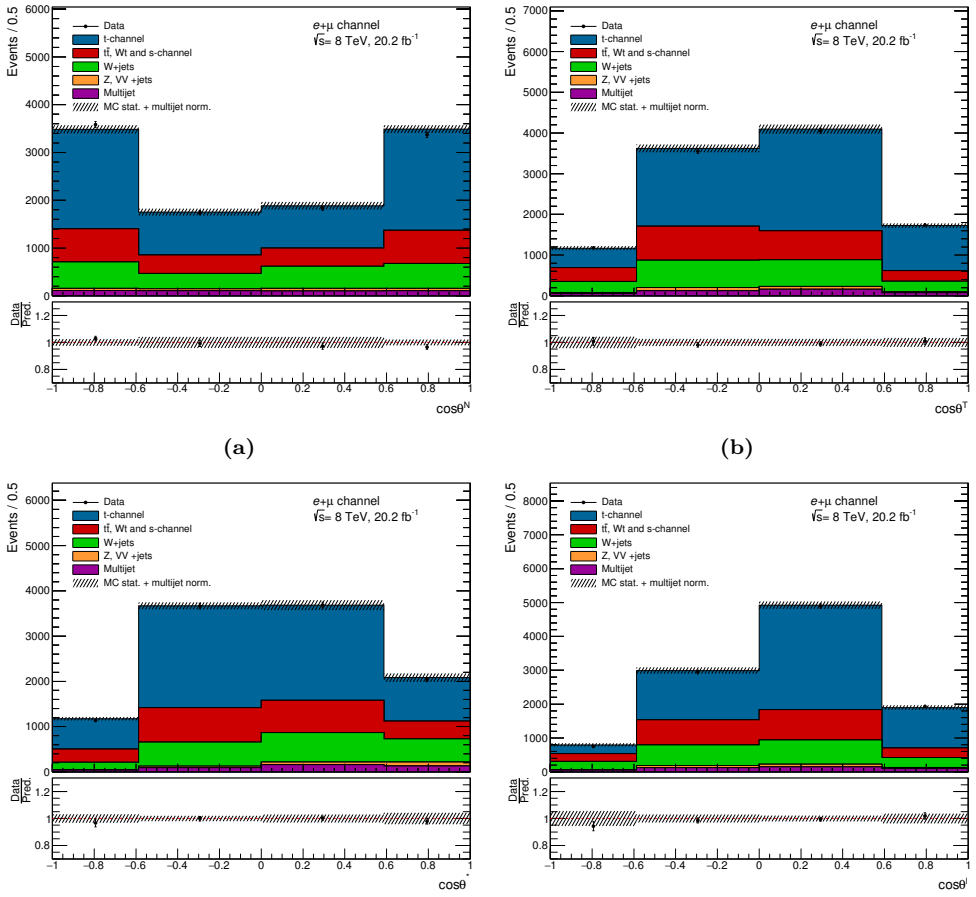

Figura 7.7: Distribuciones angulares medidas en la región de señal, usadas para medir los distintos observables: $\cos\theta^N$ (a), $\cos\theta^T$ (b), $\cos\theta^*$ (c), $\cos\theta^l$ (d). La normalización de los fondos de quarks top y de W+jets así como la normalización de los eventos de quarks top producidos en solitario en el canal t están reescalados usando los valores mostrados en la Tabla 4.2. Las bandas de incertidumbre se corresponden a la incertidumbre estadística de las muestras simuladas añadida en cuadratura con la incertidumbre en la normalización de los procesos de multijets. Los canales de electrones y muones han sido combinados.

tribución angular, mostradas en la Figura 7.7. A continuación, los eventos restantes son nuestra señal, la cual es deconvolucionada utilizando la técnica descrita anteriormente. Por último, los observables son medidos utilizando las distribuciones angulares deconvolucionadas.

Los resultados obtenidos se muestran en la Figura 7.8, y son detallados a continuación:

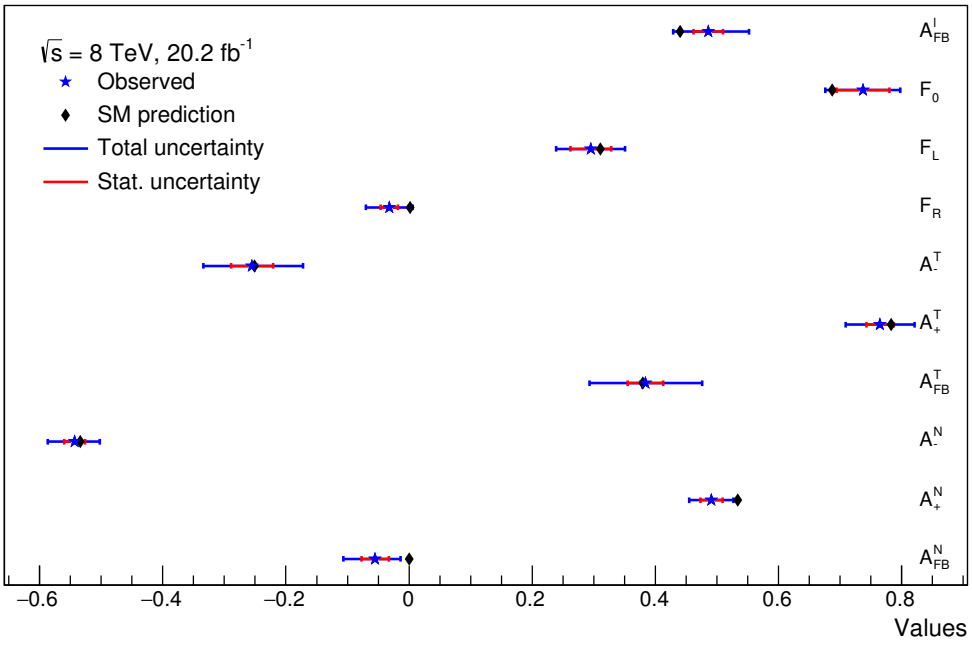

Figura 7.8: Figura resumen de las medidas de las asimetrías para las distribuciones $\cos\theta^N$, $\cos\theta^T$ y $\cos\theta^l$. Para la distribución $\cos\theta^*$ se muestran los valores de las fracciones de helicidad del bosón W. El valor predicho por el Modelo Estándar para los diferentes observables ha sido añadido para su comparación.

$$
\begin{aligned}
A_{FB}^{l} &= 0.486 \pm 0.024(stat.)\ ^{+0.062}_{-0.052}(syst.) &&= 0.486^{+0.066}_{-0.057}\\
A_{FB}^{N} &= -0.055 \pm 0.022(stat.)\ ^{+0.034}_{-0.047}(syst.) &&= -0.055^{+0.041}_{-0.052}\\
A_{+}^{N} &= 0.491 \pm 0.018(stat.)\ ^{+0.032}_{-0.031}(syst.) &&= 0.491^{+0.037}_{-0.036}\\
A_{-}^{N} &= -0.543 \pm 0.017(stat.)\ ^{+0.038}_{-0.040}(syst.) &&= -0.549^{+0.041}_{-0.044}\\
A_{FB}^{T} &= 0.384 \pm 0.029(stat.)\ ^{+0.087}_{-0.086}(syst.) &&= 0.384^{+0.092}_{-0.091}\\
A_{+}^{T} &= 0.765 \pm 0.022(stat.) \pm 0.050(syst.) &&= 0.765 \pm 0.055\\
A_{-}^{T} &= -0.255 \pm 0.034(stat.)\ ^{+0.077}_{-0.073}(syst.) &&= -0.261^{+0.084}_{-0.080}\\
A_{FB} &= -0.258 \pm 0.021(stat.) \pm 0.063(syst.) &&= -0.258 \pm 0.067\\
A_{+} &= 0.543 \pm 0.024(stat.)\ ^{+0.044}_{-0.043}(syst.) &&= 0.543 \pm 0.050\\
A_{-} &= -0.864 \pm 0.009(stat.)\ ^{+0.030}_{-0.029}(syst.) &&= -0.864 \pm 0.031\\
\alpha_l P &= 0.972 \pm 0.048(stat.)\ ^{+0.124}_{-0.104}(syst.) &&= 0.972\ ^{+0.132}_{-0.114}\\
F_0 &= 0.737 \pm 0.043(stat.) \pm 0.049(syst.) &&= 0.737 \pm 0.065\\
F_L &= 0.295 \pm 0.033(stat.)\ ^{+0.052}_{-0.053}(syst.) &&= 0.295\ ^{+0.062}_{-0.063}\\
F_R &= -0.032 \pm 0.014(stat.)\ ^{+0.031}_{-0.030}(syst.) &&= -0.032 \pm 0.034
\end{aligned}
$$

El cálculo de la incertidumbre sistemática y estadística ha sido realizado mediante la generación de pseudoexperimentos utilizando muestras sistemáticamente variadas con las diferentes fuentes de incertidumbre que se propagan en la medida.

La compatibilidad de estos resultados con los valores predichos con el Modelo Estándar ha sido evaluada mediante un test estadístico construyendo una función χ^2 teniendo en cuenta las correlaciones e incertidumbres de cada observable, obteniendo un valor para el p-value de 0.91.

En esta tesis se muestra la primera medida de las fracciones de helicidad del bosón W usando eventos con quarks top producidos en solitario realizada en ATLAS. El valor medido para la asimetría A_{FB}^{N} mejora el resultado obtenido anteriormente por ATLAS en el análisis realizado a $\sqrt{s}$= 7 TeV [98]. Esta mejora se debe principalmente a la mayor cantidad de datos registrados a $\sqrt{s}$= 8 TeV. Finalmente, el trabajo realizado en esta tesis ha conducido al trabajo posterior publicado recientemente en [124], donde se ha considerado un conjunto más amplio de asimetrías que ha permitido una interpretación en términos de los observables de spin del bosón W descritos en la Referencia [142], y en la cual se han extraidos límites a la parte imaginaria del acoplamiento g_R gracias al desarrollo de una técnica de interpolación para realizar la deconvolución de la distribución angular $\cos\theta^N$.

APPENDIX A

Neutrino longitudinal momentum

After applying the preselection requirements, described in Section 4.3, the remaining events contain all the physics objects that can be associated to all the decay products of the top quark: a lepton, a neutrino as missing transverse energy and a b-tagged jet. Therefore, in order to reconstruct the top quark four-momentum, we need first to reconstruct the W boson one.

The W boson four-momentum can be reconstructed from the lepton and the neutrino four-momenta:

$$W \to l\nu \longrightarrow \quad \mathcal{P}^W = \mathcal{P}^l + \mathcal{P}^\nu, \tag{A.1}$$

$$(\mathcal{P}^W)^2 = (\mathcal{P}^l + \mathcal{P}^\nu)^2 \longrightarrow \quad M_W^2 = m_l^2 + m_\nu^2 + 2(E^l, \mathbf{p}^l) \cdot (E^\nu, \mathbf{p}^\nu) \quad . \tag{A.2}$$

From now on, the neutrino mass is neglected, $m_\nu \approx 0$. We assume that the measured missing transverse energy fully corresponds to the neutrino transverse momentum. Consequently, the energy of the neutrino in Equation A.1 can be written as:

$$p_x^\nu = E_T^{miss} \cos\phi_{E_T^{miss}}, \tag{A.3}$$

$$p_y^\nu = E_T^{miss} \sin\phi_{E_T^{miss}}, \tag{A.4}$$

$$E^\nu = \sqrt{E_T^{miss} + (p_z^\nu)^2}. \tag{A.5}$$

As a result, the equation A.1 can be written as:

$$M_W^2 = m_l^2 + 2E^l\sqrt{E_T^{miss} + (p_z^\nu)^2} - 2(p_x^l p_x^\nu + p_y^l p_y^\nu + p_z^l p_z^\nu). \tag{A.6}$$

In Equation A.6, all the terms are known except the longitudinal momentum of the neutrino, p_z^ν. Using as the W boson pole-mass constrain, M_W = 80.4 GeV, the p_z^ν can be determined from the following quadratic equation:

$$p_z^2(\nu) - 2\frac{\mu p_z(l)}{E^2(l) - p_z^2(l)} \cdot p_z(\nu) + \frac{E^2(l)(E_T^{miss})^2 - \mu^2}{E^2(l) - p_z^2(l)} = 0, \tag{A.7}$$

with

$$\mu = \alpha + \beta E_T^{miss}, \tag{A.8}$$

$$\alpha = \frac{M_W^2 - m_l^2}{2}, \tag{A.9}$$

$$\beta = p_x(l)\cos\phi_{E_T^{miss}} + p_y(l)\sin\phi_{E_T^{miss}}. \tag{A.10}$$

Depending on the momentum of the lepton and the E_T^{miss}, Equation A.7 may have 0, 1 or 2 real solutions for the longitudinal momentum of the neutrino. The candidate with the smallest $p_z(\nu)$ value is chosen to reconstruct the W boson. This is possible when there are two real solutions for $p_z(\nu)$. When there are no real solutions, that means the discriminant of the quadratic equation is $\Delta < 0$[1], we have to apply a different strategy to reconstruct the W boson.

The charged lepton is usually very well reconstructed while the neutrino four-momentum has to be inferred from the reconstructed $E_{\mathrm{T}}^{\mathrm{miss}}$. In consequence, complex solutions in Equation A.7 point to a defective $E_{\mathrm{T}}^{\mathrm{miss}}$ determination. This can be due to the non-perfect resolution and calibration of the $E_{\mathrm{T}}^{\mathrm{miss}}$ measurement, and also to additional contributions to the missing transverse momentum, such as extra neutrinos from B-hadron and τ decays, etc. In order to find a possible solution to Equation A.7, the measured missing transverse momentum is modified while preserving its azimuthal angle. This is done in such a way that the W boson transverse mass matches the pole-mass, which is equivalent to solve the discriminant equation $\Delta = 0$. The re-scaled value $E_{\mathrm{T}}^{\mathrm{miss}'}$ of the magnitude of the missing transverse momentum is obtained

[1]The solution of a quadratic equation, $a \cdot x^2 + b \cdot x + c = 0$, is given by the formula: $x = (-b \pm \sqrt{b^2 - 4ac})/(2a)$, where we can define the discriminant as $\Delta = b^2 - 4ac$. Depending on the value of the discriminant, the quadratic equation can have two real solutions ($\Delta > 0$), one ($\Delta = 0$) or no real solutions ($\Delta < 0$).

from the new quadratic equation:

$$\left(\beta^2 - (E^2(\ell) - p_z^2(\ell))\right) \cdot {E_{\mathrm{T}}^{\mathrm{miss}}}'^2 + 2 \cdot \alpha \cdot \beta \cdot E_{\mathrm{T}}^{\mathrm{miss}'} + \alpha^2 = 0 \quad . \tag{A.11}$$

Two solutions for $E_{\mathrm{T}}^{\mathrm{miss}'}$ are provided by Equation A.11. If only one solution is positive, this is the one that is chosen. If the two solutions are positive, the one closest to the initial $E_{\mathrm{T}}^{\mathrm{miss}}$ value is taken. Once the $E_{\mathrm{T}}^{\mathrm{miss}'}$ solution is chosen, it is increased by few eV in order to make $\Delta > 0$, and it is used in Equation A.7 to finally compute the $p_z(\nu)$ solutions. Two real solutions are then obtained, and the solution giving the smallest magnitude of the longitudinal neutrino momentum is taken to reconstruct the W boson.

Finally, by adding the four-momentum of the b-tagged jet as it is measured by the detector, as well as the four-momentum of the W boson reconstructed as described above, the top quark four-momentum is reconstructed.

APPENDIX B

Constrained normalizations

A data-driven method, based on the maximum-likelihood fit of the numbers of data events obtained in the $t\bar{t}$ and anti-signal control regions defined in Section 4.3 is applied to constrain simultaneously the overall normalizations of the W+jets and top quark background ($t\bar{t}$, single top Wt and s-channel) contributions. The simultaneous fit also includes the number of events observed in the signal region, in order to constrain the low, but non-negligible contribution of t-channel events in the two control regions.

In the fitting procedure, the scale factors associated with the predicted W+jets and top quark background event yields are considered as constrained parameters of the fit, while all other background contributions, Z+jets, diboson and multijet productions, are fixed to their simulated or data-driven predictions. The overall normalization of the signal is completely left free in the fit.

In order to reduce the statistical fluctuations, the $t\bar{t}$, single top Wt and s-channel processes are merged into a single contribution, as well as the W+light and W+heavy flavour processes, which are also merged. The used likelihood function is given by the product of the Poisson distributions of the individual signal and background rates per selection, signal and control regions, being the background rates constrained by Gaussian priors:

$$L(\beta^s;\beta_j^b) = \prod_{i=1}^{N_{selections}} \frac{e^{-\mu_i}\cdot\mu_i^{n_i}}{n_i!} \cdot \prod_{j=1}^{N_{backgrounds}} G\left(\beta_j^b;1,\Delta_j\right) \ , \tag{B.1}$$

$$\text{with} \quad \mu_i = \mu_i^s + \sum_{j=1}^{N_{backgrounds}} \mu_{ij}^b \ , \ \mu_i^s = \beta^s\cdot\tilde{\nu}_i^s \ \ and \ \ \mu_{ij}^b = \beta_j^b\cdot\tilde{\nu}_{ij}^b \ . \tag{B.2}$$

This likelihood function includes for each selection index i, a Poisson term in the observed number of events n_i, with the expectation value, μ_i, defined as the sum of the expected contributions from signal μ_i^s, and all simulated or data-driven backgrounds μ_{ij}^b, where the index j runs over the background processes. For a given process, the expectation value in each selection is given by the the product of the predicted number of events $\tilde{\nu}_i^s$, for signal or $\tilde{\nu}_{ij}^b$ for backgrounds in the considered sample, and a scale factor β^s or β_j^b.

The Gaussian constraints Δ_j used in the likelihood fit for the top quark and W+jets background normalizations are set to the theoretical cross section uncertainties. For the merged top quark background processes, a constraint value of 6% that combines the theoretical cross section uncertainties in proportion to the contribution of each individual process, is applied; for the W+jets contribution, a constraint of 20% is considered [125]. For the Z+jets, diboson and data-driven multijet backgrounds, which are not allowed to vary, the constraint values are set to 0.

The scale factors extracted for the W+jets, top quark backgrounds and t-channel signal contribution are reported in Table B.1 for the electron and muon channels and for the two lepton flavours merged.

Values very close to 1.0 are found for the merged top quark background processes which are dominated by $t\bar{t}$ production. Therefore, the evaluated data-driven normalizations are consistent with the NNLO cross section calculations, which central values are used to normalize the corresponding simulations samples, and which theoretical uncertainties are used to constrain the fit.

The impact of the normalization constraints imposed to the fitted background contributions have been checked. It has been found that the extracted scale factors for the W+jets, top quark backgrounds and t-channel signal are not at all sensitive to the fit constraints applied on Z+jets and diboson background contributions. A very strong constraint is already imposed by the two

Process	e-channel	μ-channel	e+μ-channels
t-channel	0.952±0.028	0.952±0.026	0.952±0.019
W+jets	1.062±0.019	1.130±0.016	1.101±0.012
$t\bar{t}$,Wt,s-channel	1.015±0.007	1.008±0.007	1.011±0.005

Table B.1: Scale factors extracted for the t-channel signal contribution, and for the W+jets and top quark background processes from the simultaneous maximum-likelihood fit of the numbers of data events observed in the signal region and in the $t\bar{t}$-enriched and anti-signal control regions. The uncertainties come from the likelihood fit; they are related to the Poissonian and Gaussian terms of the likelihood function B.1.

considered control regions described in Section 4.3.3. The same set of scale factors is also found when the multijet contribution is not kept fixed but allowed to float within a 70% normalization constraint, showing that there is also no significant sensitivity of the likelihood fit results to the multijet contribution.

The normalization correction factors given in Table B.1 are used to control the good modelling of the kinematic and angular variable distributions in the $t\bar{t}$ control region, and in the preselection and anti-signal regions. These normalization correction factors are also used to compare to the data the kinematic and angular variable distributions predicted for the samples of selected signal events.

For the polarisation measurement, which is carried out with the unfolding method presented in Section 5.1.1, the W+jets and top quark backgrounds are re-normalized using the scale factors reported in B.1. The re-normalization is applied before subtracting the predicted background contributions to the observed angular distributions.

To check the good modelling of the simulated W+jets events in the W+jets control region defined in Section 4.3, another set of scale factors is applied on the simulated W+jets distributions.

It is noted in Figures B.1 that the simulated W+jets events do not describe the data very well in this region. In order to check if a better data description can be achieved, the W+jets events are re-weighted using scale factors extracted in the W+jets control region from the bin-per-bin data-prediction matching of the $p_T(W)$ distribution. Before calculating the re-weighting factors, an overall normalization factor is simply calculated by matching the total predicted W+jets event yields to the number of events observed in the W+jets control region for each lepton channel, whereas all other contributions are kept to their predicted or data-driven normalizations. Then, all other contributions are subtracted to the data and lastly, the re-weighting factors are extracted

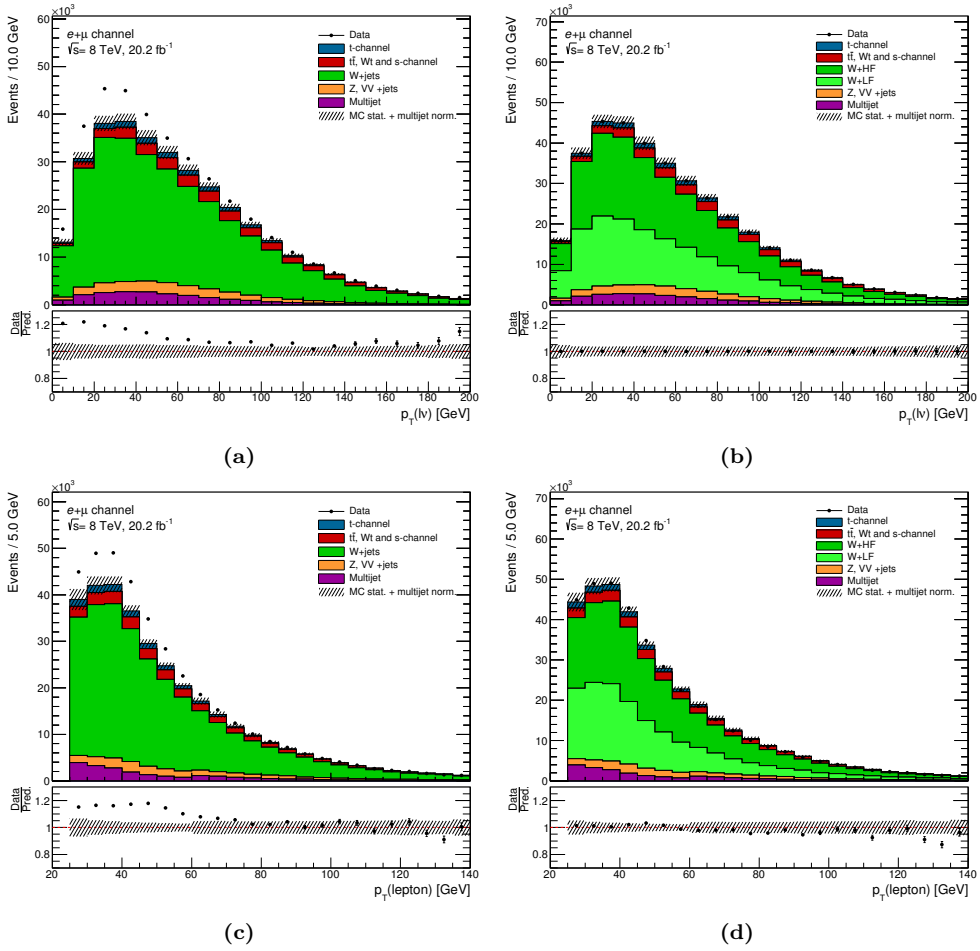

Figure B.1: Distributions of the W boson $p_T(W)$ and the lepton $p_T(l)$ in the W+jets control region before applying the corrections, (a), (c), and after having applied them (b), (d). The normalization of the W+jets as well as the trends observed in the distributions are improved after the corrections.

by matching bin-per-bin the predicted $p_T(W)$ distribution from the W+jets contribution to the remaining data distribution. The distributions before and after apply the overall scale factors and the re-weighting are displayed in Figure B.1. It can be seen that a better data-prediction agreement is reached after all corrections are applied. In the analysis, neither the overall scale factors nor the re-weighting are applied to the W+jets events in the $t\bar{t}$, anti-signal and signal regions. However, the W+jets mis-modelling is taken into account through an additional systematic uncertainty, which is evaluated by comparing the measurement results obtained without and with the bin-per-bin scale factors. This re-weighting method has been previously used in the search for FCNC in single top quark production at 8 TeV [44]

APPENDIX C

Unfolding iterations

In the incoming tables C.1–C.4, the results of the convergence test performed to find the optimal number of iterations to be used in the RooUnfold Bayes method are shown. The yellow background denotes when the convergence criterion is fulfilled by one of the observables, while the row highlighted in red indicates when all the observables fulfilled the criterion, which defines the number of iterations as it is explained in Section 5.1.2.

n_{iter}	A_{FB}^N	ΔA_n	A_+^N	ΔA_n	A_-^N	ΔA_n
1	-0,000230	0,001444	0,536832	0,001181	-0,532370	0,001319
2	-0,001674	0,001977	0,538013	0,000706	-0,531052	0,000796
3	-0,003650	0,002014	0,538719	0,000546	-0,530256	0,000600
4	-0,005664	0.001913	0.539265	0.000478	-0.529657	0.000507
5	-0.007577	0.001780	0.539743	0.000438	-0.529150	0.000448
6	-0.009357	0.001646	0.540181	0.000407	-0.528702	0.000404
7	-0.011003	0.001519	0.540587	0.000378	-0.528298	0.000367
8	-0.012522	0.001400	0.540966	0.000352	-0.527931	0.000335
9	-0.013922	0.001291	0.541317	0.000326	-0.527596	0.000306
10	-0.015213	0.001190	0.541643	0.000302	-0.527289	0.000281
11	-0.016403	0.001097	0.541946	0.000280	-0.527009	0.000258
12	-0.017500	0.001011	0.542225	0.000259	-0.526751	0.000237
13	-0.018511	0.001001	0.542484	0.000239	-0.526515	0.000218
14	-0.019512	0.000997	0.542723	0.000221	-0.526297	0.000200
15	-0.020509		0.542944		-0.526097	

Table C.1: This table shows the asymmetry values measured for the $\cos\theta^N$ distribution as a function of the number of iterations used in the RooUnfold Bayes method. The absolute difference between the extracted asymmetries from two successive steps ($\Delta A_n = |A_{n+i} - A_n|$) is also shown.

n_{iter}	A_{FB}^T	ΔA_n	A_+^T	ΔA_n	A_-^T	ΔA_n
1	0,344175	0,004335	0,757306	0,001225	-0,306633	0,004963
2	0,348510	0,003048	0,758530	0,000654	-0,301670	0,003585
3	0,351557	0,002144	0,759184	0,000262	-0,298085	0,002596
4	0,353702	0,001511	0,759446	0,000006	-0,295489	0,001884
5	0,355213	0,001068	0,759440	0,000187	-0,293605	0,001370
6	0,356281	0,000758	0,759253	0,000307	-0,292234	0,000999
7	0,357039	0,000541	0,758946	0,000385	-0,291236	0,000729
8	0,357580	0,000391	0,758561	0,000433	-0,290507	0,000532
9	0,357971	0,000287	0,758128	0,000461	-0,289975	0,000387
10	0,358257	0,000214	0,757667	0,000475	-0,289589	0,000279
11	0,358472	0,000165	0,757192	0,000479	-0,289309	0,000200
12	0,358637	0,000131	0,756714	0,000476	-0,289110	0,000139
13	0,358768	0,000108	0,756237	0,000470	-0,288970	0,000094
14	0,358877	0,000093	0,755768	0,000461	-0,288876	0,000059
15	0,358970		0,755307		-0,288817	

Table C.2: This table shows the asymmetry values measured for the $\cos\theta^T$ distribution as a function of the number of iterations used in the RooUnfold Bayes method. The absolute difference between the extracted asymmetries from two successive steps ($\Delta A_n = |A_{n+i} - A_n|$) is also shown.

n_{iter}	A_{FB}	ΔA_n	A_+	ΔA_n	A_-	ΔA_n
1	-0,245290	0,006724	0,526699	0,005471	-0,847248	0,002875
2	-0,252014	0,002191	0,521228	0,001349	-0,850123	0,001532
3	-0,254205	0,000639	0,519879	0,000225	-0,851655	0,000997
4	-0,254844	0,000087	0,519654	0,000024	-0,852652	0,000747
5	-0,254931	0,000115	0,519678	0,000043	-0,853398	0,000608
6	-0,254816	0,000188	0,519721	0,000017	-0,854006	0,000518
7	-0,254629	0,000209	0,519738	0,000009	-0,854524	0,000451
8	-0,254419	0,000210	0,519729	0,000026	-0,854975	0,000399
9	-0,254210	0,000200	0,519703	0,000035	-0,855375	0,000356
10	-0,254010	0,000187	0,519668	0,000039	-0,855731	0,000319
11	-0,253823	0,000172	0,519629	0,000039	-0,856050	0,000287
12	-0,253650	0,000158	0,519590	0,000038	-0,856338	0,000259
13	-0,253492	0,000144	0,519552	0,000036	-0,856597	0,000234
14	-0,253348	0,000131	0,519517	0,000033	-0,856831	0,000211
15	-0,253218		0,519484		-0,857042	

Table C.3: This table shows the asymmetry values measured for the $\cos\theta^*$ distribution as a function of the number of iterations used in the RooUnfold Bayes method. The absolute difference between the extracted asymmetries from two successive steps ($\Delta A_n = |A_{n+i} - A_n|$) is also shown.

n_{iter}	A^l_{FB}	ΔA_n
1	0,439270	0,002451
2	0,436819	0,001492
3	0,435327	0,000907
4	0,434420	0,000551
5	0,433868	0,000335
6	0,433533	0,000204
7	0,433330	0,000124
8	0,433206	0,000075
9	0,433131	0,000046
10	0,433085	0,000028
11	0,433058	0,000017
12	0,433041	0,000010
13	0,433031	0,000006
14	0,433024	0,000004
15	0,433021	

Table C.4: This table shows the asymmetry value measured for the $\cos\theta^l$ distribution as a function of the number of iterations used in the RooUnfold Bayes method. The absolute difference between the extracted asymmetries from two successive steps ($\Delta A_n = |A_{n+i} - A_n|$) is also shown.

APPENDIX D

Expected uncertainties

In the next tables the breakdown of the expected systematic uncertainties on the polarisation observables related the angular distributions $\cos\theta^N$ (Table D.1), $\cos\theta^T$ (Table D.2), $\cos\theta^*$ (Tables D.3 and D.4) and $\cos\theta^l$ (Table D.5) are shown. These expected uncertainties are evaluated following the methodology of pseudo-experiments described in Section 5.2.2. To that end, signal acceptance, background rates and angular distribution shapes given by the simulated event or data-driven samples are used. The systematic uncertainties are then included by varying the rates and shapes according to Equations 5.3 and 5.4 in order to produce pseudo-data distributions from which the polarisation observables are measured. Then, the expected nominal background contributions are subtracted from the pseudo-data distribution in order to extract the signal contribution. Finally, the signal contribution is deconvolved from the migration and efficiency effects using the unfolding method described in Section 5.1.1.

Systematic	ΔA_{FB}^{N}	ΔA_{+}^{N}	ΔA_{-}^{N}
Data statistics	0.023/-0.023	0.017/-0.017	0.017/-0.017
Simulation statistics	0.018/-0.018	0.013/-0.013	0.012/-0.012
Luminosity	0.000/-0.000	0.000/-0.000	0.000/-0.000
Background normalization	0.007/0.007	0.005/0.005	0.005/0.005
Background modelling	0.015/0.025	0.006/0.004	0.013/0.008
E_T^{miss} reconstruction	0.004/0.004	0.005/0.004	0.004/0.004
Lepton reconstruction	0.002/0.002	0.004/0.003	0.003/0.003
Jet reconstruction	0.010/0.010	0.011/0.011	0.015/0.015
Jet energy scale	0.021/0.034	0.009/0.010	0.015/0.023
Jet flavour tagging	0.003/0.003	0.002/0.002	0.002/0.002
PDF	0.000/-0.000	0.000/-0.000	0.000/-0.000
$t\bar{t}$ ISR/FSR	0.004/0.004	0.001/0.001	0.007/0.007
$t\bar{t}$ generator	-0.002/0.002	0.002/-0.002	-0.008/0.008
$t\bar{t}$ parton shower	0.014/-0.014	0.010/-0.010	0.003/-0.003
Wt,s-channel generator	0.003/0.003	0.004/0.004	0.002/0.002
Wt,s-channel scale	0.005/0.005	0.005/0.005	0.006/0.006
$t-$channel NLO generator	0.001/-0.001	-0.016/0.016	0.023/-0.023
$t-$channel LO-NLO generator	0.004/-0.004	0.004/-0.004	0.004/-0.004
$t-$channel parton shower	-0.005/0.005	-0.001/0.001	-0.010/0.010
$t-$channel generator scale	0.008/0.008	0.013/0.013	0.007/0.007
Total systematic (quadratic sum)	+0.035/-0.048	+0.030/-0.029	+0.039/-0.042
Total (quadratic sum)	+0.041/-0.053	+0.034/-0.034	+0.043/-0.045

Table D.1: Expected uncertainty breakdown for $\cos\theta^N$ observables

Systematic	ΔA_{FB}^{T}	ΔA_{+}^{T}	ΔA_{-}^{T}
Data statistics	0.030/-0.030	0.022/-0.022	0.033/-0.033
Simulation statistics	0.022/-0.022	0.017/-0.017	0.023/-0.023
Luminosity	0.000/-0.000	0.000/-0.000	0.000/-0.000
Background normalization	0.010/0.010	0.004/0.004	0.010/0.010
Background modelling	0.016/0.010	0.011/0.007	0.016/0.010
E_T^{miss} reconstruction	0.003/0.003	0.004/0.003	0.004/0.005
Lepton reconstruction	0.013/0.013	0.004/0.005	0.014/0.014
Jet reconstruction	0.009/0.009	0.008/0.008	0.015/0.015
Jet energy scale	0.055/0.054	0.036/0.036	0.030/0.021
Jet flavour tagging	0.006/0.006	0.003/0.003	0.005/0.005
PDF	0.001/-0.001	0.001/-0.001	0.001/-0.001
$t\bar{t}$ ISR/FSR	0.006/0.006	0.004/0.004	0.012/0.012
$t\bar{t}$ generator	-0.034/0.034	-0.022/0.022	-0.022/0.022
$t\bar{t}$ parton shower	0.012/-0.012	0.013/-0.013	0.007/-0.007
Wt,s-channel generator	0.007/0.007	0.005/0.005	0.002/0.002
Wt,s-channel scale	0.005/0.005	0.004/0.004	0.004/0.004
$t-$channel NLO generator	-0.042/0.042	-0.008/0.008	-0.045/0.045
$t-$channel LO-NLO generator	0.020/-0.020	0.014/-0.014	0.014/-0.014
$t-$channel parton shower	0.001/-0.001	-0.001/0.001	-0.025/0.025
$t-$channel generator scale	0.021/0.021	0.012/0.012	0.015/0.015
Total systematic (quadratic sum)	+0.088/-0.087	+0.052/-0.051	+0.074/-0.070
Total (quadratic sum)	+0.093/-0.092	+0.056/-0.056	+0.081/-0.077

Table D.2: Expected uncertainty breakdown for $\cos\theta^{T}$ observables

Systematic	ΔA_{FB}	ΔA_{+}	ΔA_{-}
Data statistics	0.021/-0.021	0.025/-0.025	0.010/-0.010
Simulation statistics	0.015/-0.015	0.016/-0.016	0.009/-0.009
Luminosity	0.000/-0.000	0.000/-0.000	0.000/-0.000
Background normalization	0.006/0.006	0.003/0.003	0.003/0.003
Background modelling	0.019/0.019	0.008/0.006	0.009/0.009
E_T^{miss} reconstruction	0.008/0.007	0.003/0.003	0.006/0.004
Lepton reconstruction	0.014/0.014	0.008/0.008	0.007/0.007
Jet reconstruction	0.009/0.009	0.001/0.001	0.005/0.005
Jet energy scale	0.032/0.032	0.020/0.019	0.016/0.016
Jet flavour tagging	0.005/0.005	0.002/0.002	0.003/0.003
PDF	0.000/-0.000	0.001/-0.001	0.000/-0.000
$t\bar{t}$ ISR/FSR	0.011/0.011	0.005/0.005	0.004/0.004
$t\bar{t}$ generator	-0.003/0.003	-0.004/0.004	-0.000/0.000
$t\bar{t}$ parton shower	0.026/-0.026	0.018/-0.018	0.013/-0.013
Wt,s-channel generator	0.004/0.004	0.005/0.005	0.003/0.003
Wt,s-channel scale	0.003/0.003	0.005/0.005	0.002/0.002
$t-$channel NLO generator	0.008/-0.008	0.015/-0.015	-0.001/0.001
$t-$channel LO-NLO generator	0.028/-0.028	0.013/-0.013	0.017/-0.017
$t-$channel parton shower	0.023/-0.023	0.008/-0.008	0.012/-0.012
$t-$channel generator scale	0.008/0.008	0.014/0.014	0.009/0.009
Total systematic (quadratic sum)	+0.064/-0.064	+0.040/-0.039	+0.034/-0.034
Total (quadratic sum)	+0.067/-0.067	+0.047/-0.046	+0.035/-0.035

Table D.3: Expected uncertainty breakdown for $\cos\theta^S$ observables

Systematic	ΔF_+	ΔF_-	ΔF_0
Data statistics	0.015/-0.015	0.034/-0.034	0.044/-0.044
Simulation statistics	0.013/-0.013	0.021/-0.021	0.029/-0.030
Luminosity	0.000/-0.000	0.000/-0.000	0.000/-0.000
Background normalization	0.004/0.004	0.005/0.005	0.008/0.008
Background modelling	0.010/0.010	0.005/0.007	0.007/0.006
E_T^{miss} reconstruction	0.007/0.005	0.003/0.003	0.004/0.007
Lepton reconstruction	0.007/0.007	0.009/0.009	0.003/0.002
Jet reconstruction	0.007/0.007	0.002/0.002	0.008/0.009
Jet energy scale	0.016/0.016	0.021/0.022	0.015/0.013
Jet flavour tagging	0.004/0.004	0.002/0.002	0.004/0.004
PDF	0.000/-0.000	0.001/-0.001	0.001/0.001
$t\bar{t}$ ISR/FSR	0.004/0.004	0.005/0.005	0.002/0.002
$t\bar{t}$ generator	0.001/-0.001	0.005/-0.005	-0.006/0.006
$t\bar{t}$ parton shower	0.011/-0.011	-0.020/0.020	0.009/-0.009
Wt,s-channel generator	0.002/0.002	0.006/0.006	0.004/0.004
Wt,s-channel scale	0.004/0.004	0.007/0.007	0.011/0.011
$t-$channel NLO generator	-0.007/0.007	-0.021/0.021	0.028/-0.028
$t-$channel LO-NLO generator	0.018/-0.018	0.011/-0.011	0.006/-0.006
$t-$channel parton shower	0.014/-0.014	-0.006/0.006	-0.008/0.008
$t-$channel generator scale	0.011/0.011	0.019/0.019	0.020/0.020
Total systematic (quadratic sum)	+0.037/-0.036	+0.045/-0.046	+0.044/-0.044
Total (quadratic sum)	+0.040/-0.039	+0.056/-0.057	+0.062/-0.062

Table D.4: Expected uncertainty breakdown for $\cos\theta^*$ polarisation fractions

Systematic	ΔA^{l}_{FB}
Data statistics	0.025/-0.025
Simulation statistics	0.025/-0.025
Luminosity	0.000/-0.000
Background normalization	0.007/0.007
Background modelling	0.015/0.014
E_T^{miss} reconstruction	0.007/0.004
Lepton reconstruction	0.008/0.006
Jet reconstruction	0.022/0.022
Jet energy scale	0.045/0.030
Jet flavour tagging	0.008/0.008
PDF	0.001/-0.001
$t\bar{t}$ ISR/FSR	0.002/0.002
$t\bar{t}$ generator	-0.020/0.020
$t\bar{t}$ parton shower	-0.006/0.006
Wt,s-channel generator	0.009/0.009
Wt,s-channel scale	0.008/0.008
$t-$channel NLO generator	0.015/-0.015
$t-$channel LO-NLO generator	0.013/-0.013
$t-$channel parton shower	0.003/-0.003
$t-$channel generator scale	0.012/0.012
Total systematic (quadratic sum)	+0.064/-0.054
Total (quadratic sum)	+0.069/-0.059

Table D.5: Expected uncertainty breakdown for $\cos\theta^{l}$ asymmetry

References

[1] ATLAS Higgs public results, *https://twiki.cern.ch/twiki/bin/view/atlaspublic/higgspublicresults*, .

[2] S. L. Glashow, *Partial-symmetries of weak interactions*, *Nuclear Physics* **22** (1961), no. 4 579 – 588.

[3] Salam, A. and Ward, J. C., *Electromagnetic and weak interactions*, *Physics Letters* **13** (nov, 1964) 168–171.

[4] Weinberg, Steven, *A Model of Leptons*, *Phys. Rev. Lett.* **19** (Nov, 1967) 1264–1266.

[5] P. W. Higgs, *Broken symmetries and the masses of gauge bosons*, *Phys. Rev. Lett.* **13** (Oct, 1964) 508–509.

[6] P. W. Higgs, *Spontaneous symmetry breakdown without massless bosons*, *Phys. Rev.* **145** (May, 1966) 1156–1163.

[7] F. Englert and R. Brout, *Broken symmetry and the mass of gauge vector mesons*, *Phys. Rev. Lett.* **13** (Aug, 1964) 321–323.

[8] **ATLAS** Collaboration, *Observation of a new particle in the search for the Standard Model Higgs boson with the ATLAS detector at the LHC*, *Phys. Lett.* **B716** (2012) 1–29, [arXiv:1207.7214].

[9] **CMS** Collaboration, *Observation of a new boson at a mass of 125 GeV with the CMS experiment at the LHC*, *Phys. Lett.* **B716** (2012) 30–61, [arXiv:1207.7235].

[10] The Royal Swedish Academy of Sciences, *The Nobel Prize in Physics 2013*, .

[11] ATLAS Standard Model public results, *https://twiki.cern.ch/twiki/bin/view/atlaspublic/standardmodelpublicresults*, .

[12] D. V. Forero, M. Tortola, and J. W. F. Valle, *Global status of neutrino oscillation parameters after Neutrino-2012*, *Phys. Rev.* **D86** (2012) 073012, [arXiv:1205.4018].

[13] A. H. G. Peter, *Dark Matter: A Brief Review*, *ArXiv e-prints* (Jan., 2012) [arXiv:1201.3942].

[14] G. R. Farrar and M. E. Shaposhnikov, *Baryon asymmetry of the universe in the minimal standard model*, *Phys. Rev. Lett.* **70** (May, 1993) 2833–2836.

[15] S. Dawson, *SUSY and such*, *NATO Sci. Ser. B* **365** (1997) 33–80, [hep-ph/9612229].

[16] A. Perez-Lorenzana, *An Introduction to extra dimensions*, *J. Phys. Conf. Ser.* **18** (2005) 224–269, [hep-ph/0503177].

[17] M. Kobayashi and T. Maskawa, *Cp-violation in the renormalizable theory of weak interaction*, *Progress of Theoretical Physics* **49** (1973), no. 2 652–657, [http://ptp.oxfordjournals.org/content/49/2/652.full.pdf+html].

[18] **CDF** Collaboration, F. Abe et al., *Observation of top quark production in $\bar{p}p$ collisions*, *Phys. Rev. Lett.* **74** (1995) 2626–2631, [hep-ex/9503002].

[19] **D0** Collaboration, S. Abachi et al., *Observation of the top quark*, *Phys. Rev. Lett.* **74** (1995) 2632–2637, [hep-ex/9503003].

[20] M. Czakon and A. Mitov, *Top++: A Program for the Calculation of the Top-Pair Cross-Section at Hadron Colliders*, *Comput. Phys. Commun.* **185** (2014) 2930, [arXiv:1112.5675].

[21] N. Kidonakis, *Next-to-next-to-leading-order collinear and soft gluon corrections for t-channel single top quark production*, *Phys. Rev.* **D83** (2011) 091503, [arXiv:1103.2792].

[22] N. Kidonakis, *Two-loop soft anomalous dimensions for single top quark associated production with a W- or H-*, *Phys. Rev.* **D82** (2010) 054018, [arXiv:1005.4451].

[23] N. Kidonakis, *NNLL resummation for s-channel single top quark production*, *Phys. Rev.* **D81** (2010) 054028, [arXiv:1001.5034].

[24] P. Kant, O. M. Kind, T. Kintscher, T. Lohse, T. Martini, S. Mölbitz, P. Rieck, and P. Uwer, *HatHor for single top-quark production: Updated predictions and uncertainty estimates for single top-quark production in hadronic collisions*, *Comput. Phys. Commun.* **191** (2015) 74–89, [arXiv:1406.4403].

[25] M. Aliev, H. Lacker, U. Langenfeld, S. Moch, P. Uwer, and M. Wiedermann, *HATHOR: HAdronic Top and Heavy quarks crOss section calculatoR*, *Comput. Phys. Commun.* **182** (2011) 1034–1046, [arXiv:1007.1327].

[26] **ATLAS** Collaboration, *Measurement of the $t\bar{t}$ production cross-section using $e\mu$ events with b -tagged jets in pp collisions at $\sqrt{s} = 7$ and 8 TeV with the ATLAS detector*, *Eur. Phys. J.* **C74** (2014), no. 10 3109, [arXiv:1406.5375]. [Addendum: Eur. Phys. J.C76,no.11,642(2016)].

[27] **ATLAS** Collaboration, *Measurement of the $t\bar{t}$ production cross-section using $e\mu$ events with b-tagged jets in pp collisions at $\sqrt{s}$=13 TeV with the ATLAS detector*, *Phys. Lett. B* **761** (Jun, 2016) 136. 19 p.

[28] **CMS** Collaboration, *Measurement of the ttbar production cross section in the emu channel in pp collisions at 7 and 8 TeV*, *CMS-PAS-TOP-13-004* (2015), no. CMS-PAS-TOP-13-004.

[29] **CMS** Collaboration, *A measurement of the inclusive tbart production cross section in proton-proton collisions at sqrts=13 TeV using events with one isolated charged lepton and at least one jet*, *CMS-PAS-TOP-16-006* (2016), no. CMS-PAS-TOP-16-006.

[30] **ATLAS** Collaboration, *Comprehensive measurements of t-channel single top-quark production cross sections at $\sqrt{s} = 7$ TeV with the atlas detector*, *Phys. Rev. D* **90** (Dec, 2014) 112006.

[31] **ATLAS** Collaboration, *Fiducial, total and differential cross-section measurements of t-channel single top-quark production in pp collisions*

at 8 TeV using data collected by the ATLAS detector, arXiv:1702.0285.

[32] **ATLAS** Collaboration, *Measurement of the inclusive cross-section of single top-quark t-channel production in pp collisions at $\sqrt{s}$ = 13 TeV*, Tech. Rep. ATLAS-CONF-2015-079, 2015.

[33] **CMS Collaboration** Collaboration, *Measurement of the single-top-quark t-channel cross section in pp collisions at $\sqrt{s}$ = 7 TeV*, *J. High Energy Phys.* **12** (Sep, 2012) 035. 41 p.

[34] **CMS** Collaboration, *Measurement of the t-channel single-top-quark production cross section and of the vt b ckm matrix element in pp collisions at $\sqrt{s}$= 8 tev*, *Journal of High Energy Physics* **2014** (2014), no. 6 90.

[35] **CMS** Collaboration, *Cross section measurement of t-channel single top quark production in pp collisions at $\sqrt{s}$ = 13 TeV*, *Submitted to: Phys. Lett. B* (2016) [arXiv:1610.0067].

[36] **ATLAS** Collaboration, *Evidence for single top-quark production in the s-channel in proton-proton collisions at $\sqrt{s} = 8$ TeV with the ATLAS detector using the Matrix Element Method*, *ATLAS-CONF-2015-047* (2015).

[37] **ATLAS** Collaboration, *Evidence for the associated production of a W boson and a top quark in ATLAS at $\sqrt{s}$ = 7 TeV*, *Phys. Lett. B* **716** (May, 2012) 142–159. 23 p.

[38] **CMS** Collaboration, *Evidence for associated production of a single top quark and W boson in pp collisions at $\sqrt{s}$ = 7 TeV*, *Phys. Rev. Lett.* **110** (2013) 022003, [arXiv:1209.3489].

[39] **ATLAS** Collaboration, M. Aaboud et al., *Measurement of the top quark mass in the $t\bar{t} \to$ dilepton channel from $\sqrt{s} = 8$ TeV ATLAS data*, *Phys. Lett.* **B761** (2016) 350–371, [arXiv:1606.0217].

[40] S. L. Glashow, J. Iliopoulos, and L. Maiani, *Weak interactions with lepton-hadron symmetry*, *Phys. Rev. D* **2** (Oct, 1970) 1285–1292.

[41] J. A. Aguilar-Saavedra, *Top flavor-changing neutral interactions: Theoretical expectations and experimental detection*, *Acta Phys. Polon.* **B35** (2004) 2695–2710, [hep-ph/0409342].

[42] J. M. Yang, B.-L. Young, and X. Zhang, *Flavor changing top quark decays in r parity violating SUSY*, *Phys. Rev.* **D58** (1998) 055001, [hep-ph/9705341].

[43] G. C. Branco and M. N. Rebelo, *New Physics in the Flavour Sector in the presence of Flavour Changing Neutral Currents*, *PoS* **Corfu2012** (2013) 024, [arXiv:1308.4639].

[44] **ATLAS** Collaboration, *Search for single top-quark production via flavour-changing neutral currents at 8 TeV with the ATLAS detector*, *Eur. Phys. J.* **C76** (2016), no. 2 55, [arXiv:1509.0029].

[45] **CMS** Collaboration, *Search for top quark decays via Higgs-boson-mediated flavor-changing neutral currents in pp collisions at sqrt(s) = 8 TeV*, *JHEP* (2016) [arXiv:1610.0485].

[46] **CMS** Collaboration, *Search for anomalous Wtb couplings and flavour-changing neutral currents in t-channel single top quark production in pp collisions at sqrt(s) = 7 and 8 TeV*, *JHEP* (2016) [arXiv:1610.0354].

[47] **ATLAS** Collaboration, *Search for flavour-changing neutral current top quark decays $t \to Hq$ in pp collisions at $\sqrt{s} = 8$ TeV with the ATLAS detector*, *JHEP* **12** (2015) 061, [arXiv:1509.0604].

[48] G. Mahlon and S. J. Parke, *Spin Correlation Effects in Top Quark Pair Production at the LHC*, *Phys. Rev.* **D81** (2010) 074024, [arXiv:1001.3422].

[49] G. Mahlon and S. J. Parke, *Single top quark production at the LHC: Understanding spin*, *Phys. Lett.* **B476** (2000) 323–330, [hep-ph/9912458].

[50] J. A. Aguilar-Saavedra, *A Minimal set of top anomalous couplings*, *Nucl. Phys.* **B812** (2009) 181–204, [arXiv:0811.3842].

[51] J. A. Aguilar-Saavedra and J. Bernabeu, *W polarisation beyond helicity fractions in top quark decays*, *Nucl. Phys.* **B840** (2010) 349–378, [arXiv:1005.5382].

[52] J. A. Aguilar-Saavedra, *Single top quark production at LHC with anomalous Wtb couplings*, *Nucl. Phys.* **B804** (2008) 160–192, [arXiv:0803.3810].

[53] L. R. Evans and P. Bryant, *LHC Machine*, *J. Instrum.* **3** (2008) S08001. 164 p.

[54] *LEP design report*, *The LEP main ring* **2** (1984) 269 p CERN-LEP-84-01.

[55] J. D. Jackson, *Classical electrodynamics*. Wiley, New York, NY, 3rd ed. ed., 1999.

[56] R. Schmidt, *Machine Protection and Interlock Systems for Circular Machines - Example for LHC*, `arXiv:1608.0308`.

[57] M. Pojer, *LHC Machine: Status and Plan*, *EPJ Web Conf.* **60** (2013) 01002.

[58] ECFA-CERN, *Workshop on Large Hadron Collider in the LEP Tunnel*, *CERN Yellow Reports: Conference Proceedings* (1984).

[59] CERN, *Lep shuts down after eleven years of forefront research, http://cds.cern.ch/record/44515*, .

[60] CERN, *Incident in lhc sector 3-4, http://press.cern/press-releases/2008/09/incident-lhc-sector-3-4*, .

[61] **ATLAS** Collaboration, G. Aad et al., *The ATLAS Experiment at the CERN Large Hadron Collider*, *JINST* **3** (2008) S08003.

[62] **CMS** Collaboration, S. Chatrchyan et al., *The CMS experiment at the CERN LHC*, *JINST* **3** (2008) S08004.

[63] **LHCb** Collaboration, J. Alves, A. Augusto et al., *The LHCb Detector at the LHC*, *JINST* **3** (2008) S08005.

[64] **ALICE** Collaboration, K. Aamodt et al., *The ALICE experiment at the CERN LHC*, *JINST* **3** (2008) S08002.

[65] **LHCf** Collaboration, *LHCf experiment: Technical Design Report*. Technical Design Report LHCf. CERN, Geneva, 2006.

[66] **TOTEM** Collaboration, *Total cross-section, elastic scattering and diffraction dissociation at the Large Hadron Collider at CERN*. Technical Design Report TOTEM. CERN, Geneva, 2004.

[67] **MoEDAL** Collaboration, *Technical Design Report of the MoEDAL Experiment*. No. CERN-LHCC-2009-006. MoEDAL-TDR-001. 2009.

[68] **ATLAS** Collaboration, *ATLAS magnet system*. Technical Design Report ATLAS. CERN, Geneva, 1997.

[69] **ATLAS** Collaboration, *ATLAS first level trigger*. Technical Design Report ATLAS. CERN, Geneva, 1998.

[70] **ATLAS** Collaboration, *ATLAS high-level trigger, data-acquisition and controls: Technical Design Report*. Technical Design Report ATLAS. CERN, Geneva, 2003.

[71] I. Foster and C. Kesselman, *The Grid: Blueprint for a New Computing Infrastructure*. Morgan Kaufmann Publishers Inc., San Francisco, CA, USA, 1999.

[72] C. Eck, J. Knobloch, L. Robertson, I. Bird, K. Bos, N. Brook, D. Düllmann, I. Fisk, D. Foster, B. Gibbard, C. Grandi, F. Grey, J. Harvey, A. Heiss, F. Hemmer, S. Jarp, R. Jones, D. Kelsey, M. Lamanna, H. Marten, P. Mato-Vila, F. Ould-Saada, B. Panzer-Steindel, L. Perini, Y. Schutz, U. Schwickerath, J. Shiers, and T. Wenaus, *LHC computing Grid: Technical Design Report. Version 1.06 (20 Jun 2005)*. Technical Design Report LCG. CERN, Geneva, 2005.

[73] WLCG, *http://wlcg.web.cern.ch*, .

[74] **ATLAS** Collaboration, *ATLAS Computing: technical design report*. Technical Design Report ATLAS. CERN, Geneva, 2005.

[75] ATLAS luminosity public results. *https://twiki.cern.ch/twiki/bin/view/AtlasPublic/LuminosityPublicResults*.

[76] **ATLAS** Collaboration, *ATLAS Data Quality Operations in 2012*, *ATL-DAPR-INT-2015-001* (Jan, 2015).

[77] **ATLAS** Collaboration, *ATLAS Detector Calibration and Alignment*, *ATL-COM-GEN-2009-042* (Oct, 2009).

[78] **ATLAS** Collaboration, *Sign-off Procedure for Bulk Data Reconstruction*, *ATL-COM-GEN-2008-002* (May, 2008).

[79] **ATLAS** Collaboration, *ATLAS inner detector*. Technical Design Report ATLAS. 1997.

[80] **ATLAS** Collaboration, *ATLAS Tracking Event Data Model*, *ATL-SOFT-PUB-2006-004* (Jul, 2006).

[81] **ATLAS** Collaboration, *Survey of the ATLAS Pixel Detector Components*, *ATL-INDET-PUB-2008-012* (Mar, 2008).

[82] **ATLAS** Collaboration, *Track Based Alignment of the ATLAS Silicon Detectors with the Robust Alignment Algorithm*, *ATL-INDET-PUB-2007-011* (Aug, 2007).

[83] T. Göttfert, *Iterative local Chi2 alignment algorithm for the ATLAS Pixel detector*. PhD thesis, Wurzburg U., 2006-05-26.

[84] **ATLAS** Collaboration, *Global chi2 approach to the Alignment of the ATLAS Silicon Tracking Detectors*, *ATL-INDET-PUB-2005-002* (2005).

[85] **ATLAS** Collaboration, *Alignment of the ATLAS Inner Detector and its Performance in 2012*, *ATLAS-CONF-2014-047* (Jul, 2014).

[86] CherryPy, *CherryPy, http://docs.cherrypy.org/en/latest/*, .

[87] ATLAS Services, *ATLAS Web Redirector Service, https://twiki.cern.ch/twiki/bin/viewauth/AtlasComputing/ATLASWebRedirectorService, https://twiki.cern.ch/twiki/bin/view/AtlasComputing/DistributedComputingMachines*, .

[88] **ATLAS** Collaboration, *Study of alignment-related systematic effects on the ATLAS Inner Detector tracking*, *ATLAS-CONF-2012-141* (Oct, 2012).

[89] **ATLAS** Collaboration, *Luminosity determination in pp collisions at $\sqrt{s}$ = 8 TeV using the ATLAS detector at the LHC*, *Eur. Phys. J.* **C76** (2016), no. 12 653, [arXiv:1608.0395].

[90] **ATLAS** Collaboration, G. Aad et al., *Performance of the ATLAS Trigger System in 2010*, *Eur. Phys. J.* **C72** (2012) 1849, [arXiv:1110.1530].

[91] **ATLAS** Collaboration, G. Aad et al., *Performance of the ATLAS muon trigger in pp collisions at $\sqrt{s} = 8$ TeV*, *Eur. Phys. J.* **C75** (2015) 120, [arXiv:1408.3179].

[92] **ATLAS** Collaboration, *The ATLAS Simulation Infrastructure*, *Eur. Phys. J.* **C70** (2010) 823–874, [arXiv:1005.4568].

[93] **GEANT4** Collaboration, S. Agostinelli et al., *GEANT4: A Simulation toolkit*, *Nucl. Instrum. Meth.* **A506** (2003) 250–303.

[94] S. Frixione, P. Nason, and C. Oleari, *Matching nlo qcd computations with parton shower simulations: the powheg method*, *JHEP* **0711** (2007) 070, [arXiv:0709.2092].

[95] H.-L. Lai, M. Guzzi, J. Huston, Z. Li, P. M. Nadolsky, J. Pumplin, and C. P. Yuan, *New parton distributions for collider physics*, *Phys. Rev.* **D82** (2010) 074024, [arXiv:1007.2241].

[96] B. P. Kersevan and E. Richter-Was, *The Monte Carlo Event Generator AcerMC versions 2.0 to 3.8 with interfaces to PYTHIA 6.4, HERWIG 6.5 and ARIADNE 4.1*, *Comput. Phys. Commun.* **184** (2013), no. 3 919 – 985, [hep-ph/0405247v3].

[97] J. Pumplin, D. R. Stump, J. Huston, H. L. Lai, P. M. Nadolsky, and W. K. Tung, *New generation of parton distributions with uncertainties from global QCD analysis*, *JHEP* **07** (2002) 012, [hep-ph/0201195].

[98] M. Moreno Llácer, *Search for CP violation in single top quark events with the ATLAS detector at LHC*. PhD thesis, Valencia U., 2014.

[99] K. Sapp, *From Bottom to Top: Identification to Precision Measurement of 3rd-Generation Quarks with the ATLAS Detector*. PhD thesis, Pittsburgh U., Jan, 2016.

[100] J. Su, *Search for anomalous coupling in Wtb vertex from the measurement of triple differential angular decay rates of single top quarks produced in the t-channel at sqrt(s) = 8 TeV with ATLAS detector*. PhD thesis, Pittsburgh U., Jan, 2017.

[101] X. Sun, *Top polarization measurement in single top quark production with the ATLAS detector*. PhD thesis, Université Joseph-Fourier - Grenoble I ; CNRS/LPSC, Oct., 2013.

[102] S. Frixione, P. Nason, and G. Ridolfi, *A Positive-weight next-to-leading-order Monte Carlo for heavy flavour hadroproduction*, *JHEP* **09** (2007) 126, [arXiv:0707.3088].

[103] E. Re, *Single-top Wt-channel production matched with parton showers using the POWHEG method*, *Eur. Phys. J.* **C71** (2011) 1547, [arXiv:1009.2450].

[104] T. Sjöstrand, S. Mrenna, and P. Z. Skands, *Pythia 6.4 physics and manual*, *JHEP* **0605** (2006) 026, [hep-ph/0603175].

[105] P. Z. Skands, *Tuning Monte Carlo Generators: The Perugia Tunes*, *Phys. Rev.* **D82** (2010) 074018, [arXiv:1005.3457].

[106] **ATLAS** Collaboration, *Comparison of Monte Carlo generator predictions to ATLAS measurements of top pair production at 7 TeV*, .

[107] **ATLAS** Collaboration, *The simulation principle and performance of the ATLAS fast calorimeter simulation FastCaloSim*, *ATL-PHYS-PUB-2010-013* (Oct, 2010).

[108] T. Gleisberg et al., *Event generation with sherpa 1.1*, *JHEP* **0902** (2009) 007, [arXiv:0811.4622].

[109] **ATLAS** Collaboration, *Measurement of the top quark pair production cross-section with atlas in the single lepton channel*, *Phys. Lett. B* **711** (2012) 244, [arXiv:1201.1889].

[110] **ATLAS** Collaboration, *Estimation of Fake Lepton Background for Top Analyses Using the $\sqrt{s} = 8$ TeV Dataset*, *ATL-COM-PHYS-2013-1100* (2013).

[111] **ATLAS** Collaboration, *Object selection and calibration, background estimations and mc samples for top quark analyses using the full 2012 data set*, *ATL-COM-PHYS-2013-1016*.

[112] **ATLAS** Collaboration, *Electron efficiency measurements with the ATLAS detector using the 2012 LHC proton-proton collision data*, *ATLAS-CONF-2014-032* (Jun, 2014).

[113] **ATLAS** Collaboration, *Measurement of the muon reconstruction performance of the ATLAS detector using 2011 and 2012 LHC proton–proton collision data*, *Eur. Phys. J.* **C74** (2014), no. 11 3130, [arXiv:1407.3935].

[114] M. Cacciari, G. P. Salam, and G. Soyez, *The anti-k_t jet clustering algorithm*, *JHEP* **0804** (2008) 063, [arXiv:0802.1189].

[115] **ATLAS** Collaboration, *Topological cell clustering in the ATLAS calorimeters and its performance in LHC Run 1*, arXiv:1603.0293.

[116] **ATLAS** Collaboration, *Jet energy measurement and its systematic uncertainty in proton-proton collisions at $\sqrt{s} = 7$ TeV with the ATLAS detector*, *Eur. Phys. J.* **C75** (2015) 17, [arXiv:1406.0076].

[117] **ATLAS** Collaboration, *Performance of pile-up mitigation techniques for jets in pp collisions at $\sqrt{s} = 8$ TeV using the ATLAS detector*, *Eur. Phys. J.* **C76** (2016), no. 11 581, [arXiv:1510.0382].

[118] **ATLAS** Collaboration, *Calibration of the performance of b-tagging for c and light-flavour jets in the 2012 ATLAS data*, *ATLAS-CONF-2014-046* (Jul, 2014).

[119] **ATLAS** Collaboration, *Performance of missing transverse momentum reconstruction in atlas studied in proton-proton collisions recorded in 2012*, ATLAS-CONF-2013-082.

[120] **ATLAS** Collaboration, *Search for anomalous couplings in the Wtb vertex from the measurement of triple differential angular decay rates of single top quarks produced in the t-channel at $\sqrt{s} = 8$ TeV with the ATLAS detector*, *ATL-COM-PHYS-2016-1803* (Dec, 2016).

[121] T. Adye, *Unfolding algorithms and tests using roounfold*, arXiv:1105.1160.

[122] G. D'Agostini, *A multidimensional unfolding method based on bayes' theorem*, *Nuclear Instruments and Methods in Physics Research Section A: Accelerators, Spectrometers, Detectors and Associated Equipment* **362** (1995), no. 2 487 – 498.

[123] A. Hocker and V. Kartvelishvili, *SVD approach to data unfolding*, *Nucl. Instrum. Meth.* **A372** (1996) 469–481, [hep-ph/9509307].

[124] **ATLAS** Collaboration, *Probing the Wtb vertex structure in t-channel single-top-quark production and decay in pp collisions at $\sqrt{s} = 8$ TeV with the ATLAS detector*, *JHEP* **04** (2017) 124, [1702.08309].

[125] **ATLAS** Collaboration, *Measurement of the Inclusive and Fiducial Cross-Section in Single Top-Quark t-Channel Events in pp Collisions at $\sqrt{s} = 8TeV, ATL - COM - PHYS - 2015 - 177(2015)$.*

[126] **ATLAS** *Collaboration, Electron and photon energy calibration with the ATLAS detector using LHC Run 1 data,* Eur. Phys. J. **C74** *(2014), no. 10 3071, [*arXiv:1407.5063*].*

[127] **ATLAS** *Collaboration, Jet energy measurement and its systematic uncertainty in proton-proton collisions at $\sqrt{s} = 7$ TeV with the ATLAS detector,* Eur. Phys. J. **C75** *(2015) 17, [*arXiv:1406.0076*].*

[128] **ATLAS** *Collaboration, Jet energy resolution in proton-proton collisions at $\sqrt{s} = 7$ TeV recorded in 2010 with the ATLAS detector,* Eur. Phys. J. **C73** *(2013), no. 3 2306, [*arXiv:1210.6210*].*

[129] **ATLAS** *Collaboration, Calibration of the performance of b-tagging for c and light-flavour jets in the 2012 ATLAS data,* ATLAS-CONF-2014-046 *(Jul, 2014).*

[130] **ATLAS** *Collaboration, Calibration of b-tagging using dileptonic top pair events in a combinatorial likelihood approach with the ATLAS experiment,* ATLAS-CONF-2014-004 *(Feb, 2014).*

[131] **ATLAS** *Collaboration, Performance of Missing Transverse Momentum Reconstruction in Proton-Proton Collisions at 7 TeV with ATLAS,* Eur. Phys. J. **C72** *(2012) 1844, [*arXiv:1108.5602*].*

[132] P. Z. Skands, Tuning monte carlo generators: The perugia tunes, Phys. Rev. **D82** *(2010).*

[133] M. Botje et al., The pdf4lhc working group interim recommendations, arXiv:1101.0538.

[134] H.-L. Lai et al., New parton distributions for collider physics, Phys. Rev. D **82** *(2010) 074024, [*arXiv:1007.2241*].*

[135] A. D. Martin, W. J. Stirling, R. S. Thorne, and G. Watt, Parton distributions for the lhc, Eur. Phys. J. C **63** *(2009) 189, [*arXiv:0901.0002*].*

[136] R. Ball et al., Parton distributions with the lhc data, Nucl. Phys. B **867** *(2013) 244, [*arXiv:1207.1303*].*

[137] W. Wagner et al., Bill tool, internal softawre tool provided by the wupertal atlas group, https://twiki.cern.ch/twiki/bin/viewauth/AtlasProtected/BillTool.

[138] **ATLAS** *Collaboration, Observation of a new particle in the search for the Standard Model Higgs boson with the ATLAS detector at the LHC,* Phys. Lett. **B716** *(2012) 1–29, [*arXiv:1207.7214*].*

[139] **ATLAS** *Collaboration, Higgs mass measurements and uncertainties in 2011 and 2012 data,* ATL-COM-PHYS-2012-1774 *(Dec, 2012).*

[140] **ATLAS** *Collaboration, Measurement of the w boson polarisation in $t\bar{t}$ events from pp collisions at $\sqrt{s}$ = 8 tev in the lepton + jets channel with atlas,* The European Physical Journal C **77** *(2017), no. 4.*

[141] **CMS** *Collaboration, Measurement of the W boson helicity fractions in the decays of top quark pairs to lepton+jets final states produced in pp collisions at $\sqrt{s}$ = 8 TeV,* Phys. Lett. B **762** *(2016), no. arXiv:1605.09047.*

[142] J. A. Aguilar-Saavedra and J. Bernabeu, Breaking down the entire W boson spin observables from its decay, Phys. Rev. **D93** *(2016), no. 1 011301, [*arXiv:1508.0459*].*

List of Figures

List of Tables